A New Moment Model For Radiative-Transport Prediction

A Thesis Submitted to
the Faculty of Graduate and Postdoctoral Studies

By

William Morin

In Partial Fulfillment of the Requirements for the Degree of
MASTERS OF APPLIED SCIENCE
in Mechanical Engineering

Department of Mechanical Engineering
University of Ottawa
Ottawa, Canada

© William Morin, Ottawa, Canada, 2020

Abstract

Accurate modelling of radiative transfer is important in many engineering applications, such as, medical imaging, cancer treatment, nuclear-power generation, and heat transfer. Unfortunately, most existing models suffer from modelling artifacts that limits their applications. Methods based on the direct tracking of particles are accurate, however, they can be prohibitively expensive for many practical engineering applications. Spherical-harmonics and discrete-ordinates models are more affordable to compute, however they often produce results that contain severe mathematical artifacts. The maximum-entropy closures feature many desirable mathematical properties. However, for all but the lowest-order members of the hierarchy, these models cannot be written in closed form. Thus, making their practical application exceedingly expensive.

In order to address these issues, the goal of this project is to develop and conduct an investigation into a new hierarchy of models for radiative transport. This model produces field equations for the prediction of general radiative transport. It is therefore expected that solutions will be far easier to compute, as compared to particle-based methods. The idea is based on a new special averaging procedure that is applied to a low order Discrete-Ordinance method. The resulting model is designed to preserve positivity of solutions, like the discrete ordinance model, while approaching rotational symmetry, like spherical-harmonics based models. In this thesis, the first-order closure of the spherical-harmonics, the discrete-ordinates and the maximum-entropy hierarchy are compared with the first member of the new hierarchy. The eigenstructure of the different first-order closures is studied and their general behaviours are compared using three standard radiation-transfer problems. Finally, the second order moment version of the closure is presented along with a discussion of the limitations of the proposed model.

Acknowledgments

First I want to thank Professor James M^{c}Donald for all the time he spent teaching me all the fundamental theories used in this thesis. I feel lucky to have been able to undertake this research project under his supervision. His great ideas and intuitions guided me during my research and when writing this thesis. His patience, motivation, and immense knowledge was crucial for the success of this project.

Along with my advisor, I would like to thank the rest of my thesis committee: Professor Matei Radulescu from University of Ottawa and Professor Jason Etele from Carleton University for their insightful comments.

I would also like to thank my fellow graduate colleagues and friends for the stimulating discussions and all the hours spent together in the computer lab. Finally, I must express my gratitude to my family for providing me with endless support and encouragements throughout my years of study.

Funding for the work presented in this thesis has been provided by the Natural Sciences and Engineering Research Council of Canada (NSERC) and from the Ontario Ministry of Training, Colleges and Universities via an Ontario Graduate Scholarship.

Contents

List of Figures

Chapter 1

Introduction

1.1 Background

Radiation plays an important role in many engineering systems. It is an especially important mode of heat transfer in situations involving high temperatures. For example, combustion chambers (internal combustion engine), furnaces, glass manufacturing and building insulation are applications where radiation is an important type of energy transport [20]. Radiative heat transfer also plays an important role in welding physics, particle physics, and astrophysics [6], as well as many other applications. In the fields of combustion in general, radiative transfer is essential in the determination of flame structure, formation of exhaust particles like soot and temperature distribution inside the combustion chamber [28]. Radiative energy transport is also used in nuclear power plants, medical imaging and radiotherapy dose simulations [24]. Accurate modelling of radiative transport is thus an important tool for radiative phenomena prediction in all the above-mentioned fields.

Many modelling methods already exist for radiative transfer simulation. However they all present serious modelling artifacts or computation difficulties. First, the models based on the direct tracking of particles are obviously the most accurate

methods. However, they can be far too expensive for many practical engineering situations, as an enormous number of particles is needed for accurate results. Only small and relatively simple problems can be solved affordably using these models. Even these calculation are often very expensive to compute. The alternative to particle-based methods are field-based models. Rather than directly tracking particles, theses models define continuous fields describing the radiation. Partial differential equations (PDEs) govern the evolution of these fields.

One family of models, the discrete-ordinates models, also termed S_N, are commonly used in radiative transfer [10, 11, 21]. They have proven to be relatively successful in predicting the behavior of radiation. These models are mathematically elegant and easy to implement because all the particles are forced to move only in a set of predefined directions. The major downside of these models is, in order to be accurate, a large number of predefined directions must be considered. This greatly increases the computational expense. Furthermore, as the predefined directions are chosen in a specific coordinate system, the resulting models are not rotationally invariant. That is, the solution depends on the original choice of coordinates directions. Despite these downsides, this family of model is an important building block for the new hierarchy of models presented in this work. A detailed analysis of this closure is presented in the following chapter.

The spherical-harmonics method, denoted as P_N, is another important approach that is discussed in this thesis [10, 26]. This alternative method uses smooth and continuous functions to approximate the radiation intensity at every point in space time [23]. This method can be derived using the moment-closure approach, which allows for a relatively simple computational implementation. The spherical-harmonics method is generally not excessively expensive to compute but suffers from important modelling artifacts. Even though those models are rotationally invariant, they do not preserve positivity of the solution. They often predict

a negative number of photons in some regions. This major downside greatly limits the physical applications of these models to practical engineering problems. A more in depth analysis of the moment closure form of these methods is presented in this work.

The positive P_N closures (PP_N), developed by Garrett and Hauck [10], are another possible approach. As mentioned before, since P_N closures use smooth functions, mainly polynomials, to approximate the kinetic system, they often produce non-realizable predictions. The PP_N closure, on the other hand, was specifically derived in order to maintain the positivity of the solution. One can think of this closure as a general spherical harmonic closure with the addition of a point-wise positivity constraint. The solutions obtained using this closure maintain a positive photons density but they often feature large oscillations and a lack of rotational symmetry [10].

Another field-based method is the maximum-entropy hierarchy of models [13, 5, 4]. These models are built by assuming that the distribution of radiative-particle velocities at any point in space is such that it maximizes the entropy, while remaining consistent with all known information regarding the state of the radiation. These models have many desirable properties. They are rotationally invariant and guarantee positivity of solutions. Unfortunately, for all but the lowest-order members of this hierarchy, the models cannot be written in closed form. This means that, whenever a flux is needed, an expensive and ill-conditioned entropy-maximization problem must be solved numerically. These ill-conditioned problem are especially difficult to compute, since any small disturbance or numerical error can change the solution drastically. This seriously limits the usefulness of these methods for practical situations.

1.2 Motivation

As mentioned, accurate radiative-transfer simulations are important in many engineering and scientific fields. The ability to make affordable and accurate predictions is crucial for medical imaging and cancer treatment but also in many energy related applications. However, more importantly, understanding these phenomena can lead to new important scientific discoveries. The goal of the present work is to develop a new class of radiation models that combines aspects of the discrete-ordinates method and the spherical-harmonic method. The hope is to produce a hierarchy of models that are rotationally invariant while guaranteeing positivity of solutions and limiting the computational cost. The development of such a hierarchy would lead to improvements in the ability to efficiently and accurately model mechanical systems that involve radiation.

1.3 Research Outline

The content of this thesis is structured as follows, Chapter 2 first introduces the kinetic-theory, moment-closure, and radiative-transport theory used in the scope of this research project. The moment-based approaches of both the spherical-harmonics and the discrete-ordinates methods are carefully derived. Finally, the first-order closure of the maximum-entropy hierarchy is also presented. In Chapter 3, the first-order closure of the new family of models is derived. The behaviour of the closing fluxes and the eigenstructure of the flux Jacobian for the different first-order closures are also studied. In Chapter 4, the numerical methods used in the scope of this project is presented along with numerical results for three characteristic benchmark problems. Solutions of the line-source benchmark, the hohlraum and the lattice problems are shown in order to investigate the capabilities of the new scheme [3]. The second-order closure of the new hierarchy of models is presented in Chapter 5 along with a discussion about the limitations encountered during the use of this new proposed model.

Chapter 2

Literature Review

In this chapter kinetic theory and the method of moments, which are used heavily in this work, are reviewed. Moment-closure techniques for the spherical-harmonics, P_N, the discrete-ordinates, S_N, and the maximum-entropy, M_N, closures are also discussed. Finally, a complete derivation of the lowest-order member of the spherical-harmonics and the discrete ordinates families are presented as examples.

2.1 Kinetic Theory

Kinetic theory is a continuum description of a system containing a large number of discrete particles (atoms, molecules, or photons) that have a constant rapid motion and can possibly be subjected to a large number of collisions with each other or other various types of matter. This theory is usually applied to gases and can explain macroscopic properties, such as temperature, pressure, viscosity, thermal conductivity and density as being related to statistics of particle velocities [18, 22, 15]. For any practical problem, tracking each single particle is very computationally expensive, the kinetic theory approach is to model the system behaviour using a statistical representation of the particle velocities.

2.1.1 Kinetic Theory of Gases

Although the goal of this work is the modelling of radiation transport, the kinetic theory of gases is an important field and allows for a better understanding of the general theory used in this work. In order to illustrate adequately this method the example of a monatomic gas system is presented. This example is first shown since it is more physically intuitive than the radiative situation.

At atmospheric conditions gases are composed of a very large number of particles that are in constant motion. Tracking every single particles contained, even in a relatively small system, is beyond the computational power of even the largest modern computers. Therefore, the kinetic theory approach is to model the system behaviour using a statistical representation of the particles velocities. This is done using a velocity distribution function denoted $\mathcal{F}(x_i, v_i, t)$, representing the number of particles at a location x_i moving at a specific velocity v_i at time t. For example, a monatomic gas in local thermodynamic equilibrium is expected to have a velocity distribution function of the following form,

$$\mathcal{F}(x_i, v_i, t) = \frac{\rho}{m}\left(\frac{\rho}{2\pi p}\right)^{\frac{3}{2}} \exp\left(\frac{-\rho}{2p}(c_i c_i)\right) , \qquad (2.1)$$
$$\text{with} \qquad c_i = v_i - u_i \, ,$$

where, v_i and u_i are particle velocity and bulk velocity respectively. Here the bulk velocity can be referred to as the average of particle velocities at a point in space and time. This distribution is famously known as the Maxwell-Boltzmann distribution. In order to evaluate the macroscopic properties of a system composed of a huge number of gas particles, velocity moments of its specific distribution function, $\mathcal{F}(x_i, v_i, t)$, must be taken. This is done by multiplying the distribution function by a velocity-dependent weight, denoted $W(v_i)$, and integrating over all

velocity space,

$$\iiint_{\infty} W(v_i)\mathcal{F}\ \mathrm{d}^3 v_i = \langle W(v_i)\mathcal{F}\rangle\ . \tag{2.2}$$

Since $\mathcal{F}(x_i, v_i, t)$ describes the number of particles at a specific position and velocity in time, the mass density, ρ, can be determined by taking the molecular mass, m, as the velocity-dependent weight, $W(v_i)$,

$$\rho = \iiint_{\infty} m\,\mathcal{F}\,\mathrm{d}^3 v_i = \langle m\mathcal{F}\rangle\ . \tag{2.3}$$

Where the notation, $\langle W(v_i)\mathcal{F}\rangle$, is used throughout this work to indicate integration over all velocity space. Essentially, this integral adds up the particles at a point regardless of their velocity and multiplies by their mass. By following the same procedure, the momentum of a given system can be found by replacing the velocity-dependent weight by, mv_i,

$$\rho u_i = \iiint_{\infty} mv_i\,\mathcal{F}\,\mathrm{d}^3 v_i = \langle mv_i\mathcal{F}\rangle\ , \tag{2.4}$$

where, again, u_i is the average velocity of all particles at a point in time. Similarly, the generalized pressure tensor, P_{ij} of the system can be described by replacing the velocity-dependent weight by mc_ic_j,

$$P_{ij} = \iiint_{\infty} mc_ic_j\,\mathcal{F}\,\mathrm{d}^3 v_i = \langle mc_ic_j\mathcal{F}\rangle\ , \tag{2.5}$$

where, the generalized pressure tensor, P_{ij} is related to the deviatoric stress tensor τ_{ij} as,

$$\tau_{ij} = \delta_{ij}p - P_{ij}\,. \tag{2.6}$$

Here, $p = P_{ii}/3$ is the equilibrium isotropic pressure [18]. Higher-order moments of the distribution function can be taken by choosing a velocity-dependent weight raised to higher powers, but their physical interpretations are harder to describe.

2.1.2 Kinetic Theory Applied to Radiation

Since radiation is also composed of a large number of "particle" (photons), accurately modelling the behaviour of each individual particles is, as for gases, highly computationally expensive and very impractical. Again, the kinetic-theory approach is to model the behaviour using a statistical representation of particles velocities. As before, this is done using a probability density functions, $\mathcal{F}(x_i, \Omega_i, t)$ [18]. This velocity distribution is a function of the position in space, x_i, the direction of the particle motion, Ω_i, and the time, t. Here, the difference between gaskinetic theory is that all photons are travel at the same speed. Therefore the velocity space is closed and can be described by a spherical surface of radius c, the speed of light. It is important to note that through this thesis all parameters are non-dimensionalized by the speed of light and by a characteristic length of 1 m. A characteristic length of 1 m was chosen for simplicity. Since the kinetic equation becomes self-similar after non-dimensionalizing by the speed of light, the choice of the characteristic length is not important. Throughout this thesis the speed of light, $c = 1.0$ for simplicity. The angular direction, Ω_i, is represented on a sphere and is usually defined using the two standard spherical angles, θ and ϕ. Figure 2.1 shows the velocity space representing all possible photons velocities.

In order to find the macroscopic properties of a radiative system, the exact same method can be applied. Moments can also be taken by integrating the product of $\mathcal{F}(x_i, \Omega_i, t)$ and a velocity-dependent weight $W(v_i)$ over all velocity space. The general moment equation is thus given by,

$$\iint_{\Omega_i} W(v_i)\, \mathcal{F}\, \mathrm{d}\Omega_i = \langle W(v_i)\mathcal{F} \rangle \ . \tag{2.7}$$

In this case, $v_i = c\Omega_i$. Again, monomials of the particle velocity are chosen as weights. A short-hand notation for moments of arbitrarily high order can be

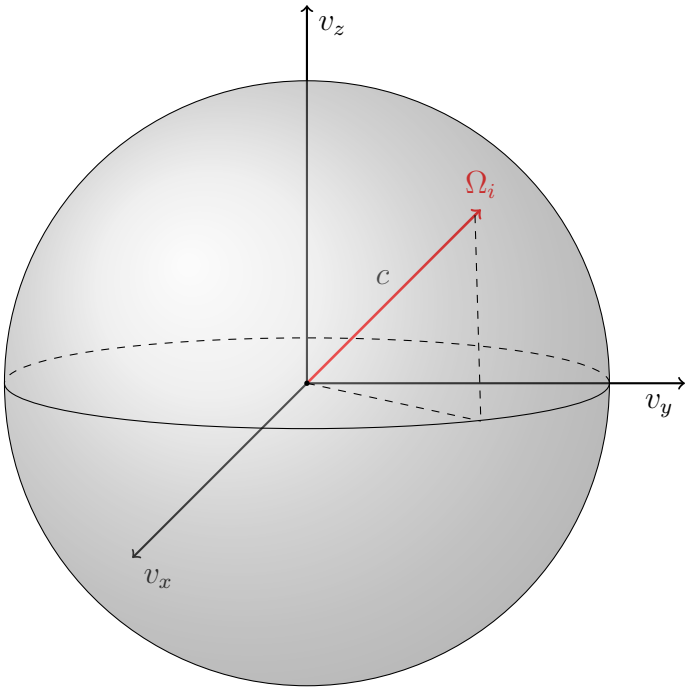

Figure 2.1: Velocity space of the radiation propagation, Ω_i

defined as

$$\rho = U_0 = \langle \mathcal{F} \rangle \ , \qquad \rho u_i = U_i = \langle v_i \mathcal{F} \rangle \ ,$$
$$U_{ij} = \langle v_i v_j \mathcal{F} \rangle \ , \qquad U_{ijk} = \langle v_i v_j v_k \mathcal{F} \rangle \ ,$$
$$U_{ijkl} = \langle v_i v_j v_k v_l \mathcal{F} \rangle \ , U_{ijk\ldots\alpha} = \langle v_i v_j v_k \ldots v_\alpha \mathcal{F} \rangle \ , \tag{2.8}$$

where, for radiation, ρ is the particle number density and u_i is the average velocity of the particles at a point in space. In this thesis the term ρu_i will be referred as the momentum density. It is important to note that this term does not represent the real photon momentum. Rather, the term "momentum" is borrowed from this moments connotation in the kinetic theory of gases. Past the first order all moments are denoted by U and the order is known from the number of indices.

2.2 The Method of Moments

In the previous section, the process to obtain macroscopic properties of a system containing a very large number of moving particles using velocity moments of

its specific distribution function is shown. However, for any practical system that is not in thermodynamic equilibrium, it is also necessary to understand how these macroscopic properties evolve in time. In that regard, the time evolution of the velocity distribution function of any general kinetic system is given by the kinetic equation,

$$\frac{\partial \mathcal{F}}{\partial t} + v_i \frac{\partial \mathcal{F}}{\partial x_i} + \frac{\partial a_i \mathcal{F}}{\partial v_i} = \frac{\delta \mathcal{F}}{\delta t}\,, \tag{2.9}$$

where, a_i is the particle acceleration due to external forces and the term on the right hand side, $\frac{\delta \mathcal{F}}{\delta t}$ is the kinetic collision term. This term accounts for the effect of the intermolecular collisions [18, 19, 27].

For almost any practical applications, directly solving the kinetic equation is impractical. In order to accurately solve this high-order partial differential equation, a numerical scheme that discretizes the spacial domain as well as the velocity domain would be needed, which is obviously prohibitively expensive. The method of moments is an efficient tool to overcome this problem. The goal of this technique is to achieve a closed-form set of first-order partial differential equations (PDEs) governing the evolution of the statistics of the particle motion [14]. This is achieved by taking moments of the kinetic equation equation.

Going back to the monatomic gas example shown in the previous section, the time evolution of the velocity distribution function, $\mathcal{F}(x_i, v_i, t)$, of a gaseous system given by Eq. (2.9). For simplicity, if one assumes that intermolecular collisions are negligible and that the external acceleration field is zero, it is possible to write the collision-less, acceleration-free kinetic equation,

$$\frac{\partial \mathcal{F}}{\partial t} + v_i \frac{\partial \mathcal{F}}{\partial x_i} = 0\,. \tag{2.10}$$

By taking moments of this simplified kinetic equation equation, one can predict the time evolution of the velocity distribution function of this monatomic gas system.

For example, if moments of the kinetic equation, Eq. (2.10), are taken with m as the weight $W(v_i)$ we find:

$$\left\langle W\left[\frac{\partial \mathcal{F}}{\partial t}+v_i\frac{\partial \mathcal{F}}{\partial x_i}=0\right]\right\rangle , \tag{2.11}$$

$$\left\langle m\left[\frac{\partial \mathcal{F}}{\partial t}+v_i\frac{\partial \mathcal{F}}{\partial x_i}=0\right]\right\rangle , \tag{2.12}$$

$$\left\langle m\frac{\partial \mathcal{F}}{\partial t}\right\rangle+\left\langle m\,v_i\frac{\partial \mathcal{F}}{\partial x_i}\right\rangle=0\,, \tag{2.13}$$

$$\frac{\partial}{\partial t}\left\langle m\mathcal{F}\right\rangle+\frac{\partial}{\partial x_i}\left\langle mv_i\mathcal{F}\right\rangle=0\,, \tag{2.14}$$

$$\frac{\partial}{\partial t}\rho+\frac{\partial}{\partial x_i}\rho u_i=0\,. \tag{2.15}$$

Equation (2.15) is called the 0^{th} moment equation. It can simply be seen as the classic continuity equation. Furthermore, if we take moments of Eq. (2.10) with mv_j as the velocity-related weight we find,

$$\left\langle mv_j\left[\frac{\partial \mathcal{F}}{\partial t}+v_i\frac{\partial \mathcal{F}}{\partial x_i}=\sigma\right]\right\rangle=0\,, \tag{2.16}$$

$$\left\langle mv_j\frac{\partial \mathcal{F}}{\partial t}\right\rangle+\left\langle mv_j\,v_i\frac{\partial \mathcal{F}}{\partial x_i}\right\rangle=0\,, \tag{2.17}$$

$$\frac{\partial}{\partial t}\rho u_i+\frac{\partial}{\partial x_i}(\rho u_i u_j+\langle m\,c_i\,c_j\,\mathcal{F}\rangle)=0\,, \tag{2.18}$$

where $c_i = v_i - u_i$ is the difference between a particle's velocity and the bulk velocity of the system. This equation is known as the conservation of momentum. Following the same procedure, the higher-order moment of this hierarchy would give the conservation of energy.

Similarly, for radiation, the evolution in time of the velocity distribution function, $\mathcal{F}$, of a collection of photons is also described by the kinetic equation [18],

$$\frac{\partial \mathcal{F}}{\partial t}+v_i\frac{\partial \mathcal{F}}{\partial x_i}+\frac{\partial a_i\mathcal{F}}{\partial v_i}=S\,. \tag{2.19}$$

In radiation transport, photons travels at constant speed, c, and have negligible inter-particle interactions, the kinetic equation for radiative transfer can thus be

simplified to,

$$\frac{\partial \mathcal{F}}{\partial t} + v_i \frac{\partial \mathcal{F}}{\partial x_i} + a_i \cancel{\frac{\partial \mathcal{F}}{\partial v_i}} = S\,, \tag{2.20}$$

$$\frac{\partial \mathcal{F}}{\partial t} + v_i \frac{\partial \mathcal{F}}{\partial x_i} = S\,, \tag{2.21}$$

where S, is a local source term. Given the previous definitions, it is now possible to write the radiative-transfer equation in the following form,

$$\frac{\partial \mathcal{F}}{\partial t} + c\,\Omega_i \frac{\partial \mathcal{F}}{\partial x_i} = S\,, \tag{2.22}$$

where the term, $c\,\Omega_i$ represents the particle velocity. The source term, S, can include emission, absorption and scattering depending on the application. For this work, simplified models are adopted for particle interactions with the background media, which leads to the source term,

$$S = \sigma_s(E - \mathcal{F}) + \sigma_e E - \sigma_a \mathcal{F}\,, \tag{2.23}$$

$$\text{with} \qquad E = \frac{\rho}{4\pi}\,, \tag{2.24}$$

where, σ_s, σ_e and σ_a represent the emission, absorption and scattering coefficients respectively. The term E represents the equilibrium distribution. In other words, the distribution with the same number density, but with all the photons evenly distributed on the sphere representing velocity space. Again, Eq. (2.22) is mathematically simple. However, it is very hight-dimensional (three space dimensions, two velocity dimensions and time). As explained above, the velocity space describing radiation transport is a spherical surface. This space can thus be described using only the two coordinates. Following the previous example, the partial differential equations (PDEs) governing the evolution of these moment can be obtained

by taking moment of the radiative-transport equation, Eq. (2.22),

$$\left\langle W \left[\frac{\partial \mathcal{F}}{\partial t} + \Omega_i \frac{\partial \mathcal{F}}{\partial x_i} = S \right] \right\rangle , \tag{2.25}$$

$$\left\langle W \frac{\partial \mathcal{F}}{\partial t} \right\rangle + \left\langle W \, \Omega_i \frac{\partial \mathcal{F}}{\partial x_i} \right\rangle = \langle W \, S \rangle , \tag{2.26}$$

$$\frac{\partial}{\partial t} \langle W \mathcal{F} \rangle + \frac{\partial}{\partial x_i} \langle W \, \Omega_i \, \mathcal{F} \rangle = \langle W \, S \rangle . \tag{2.27}$$

2.2.1 Moment Closure

As one can observe, this technique will never yield a closed set of equations. Every equation that describes the evolution of a moment, $\langle W \, \mathcal{F} \rangle$, will require information regarding the divergence of a higher-order moment, $\langle W \, v_i \, \mathcal{F} \rangle$. Any technique used to close Eq. (2.27) is known as a moment closure. This is done most often by choosing a prescribed form for $\mathcal{F}$ in terms of a number of unknown parameters, or closure coefficients. The number of coefficients should match the number of known moments in a model. These coefficients are then chosen such that the moment relations shown in Eq. (2.8) are satisfied. Once these coefficients are known, the distribution function, $\mathcal{F}$, is completely specified. Higher-order moments can simply be integrated and become functions of known moments through the prescribed form—the system is thus closed.

2.3 The Line Source Benchmark

The line source problem is a benchmark problem that was first introduced by Ganapol [9]. This is an extremely difficult problem for PDE-based models. However, since an exact solution exists, the problem is an excellent way to test different radiative transport models, thus evaluating their corresponding strength and weaknesses. This problem has become a standard by which the accuracy of different models are judged [10, 8].

The line source problem is described as an initial pulse of particles that are

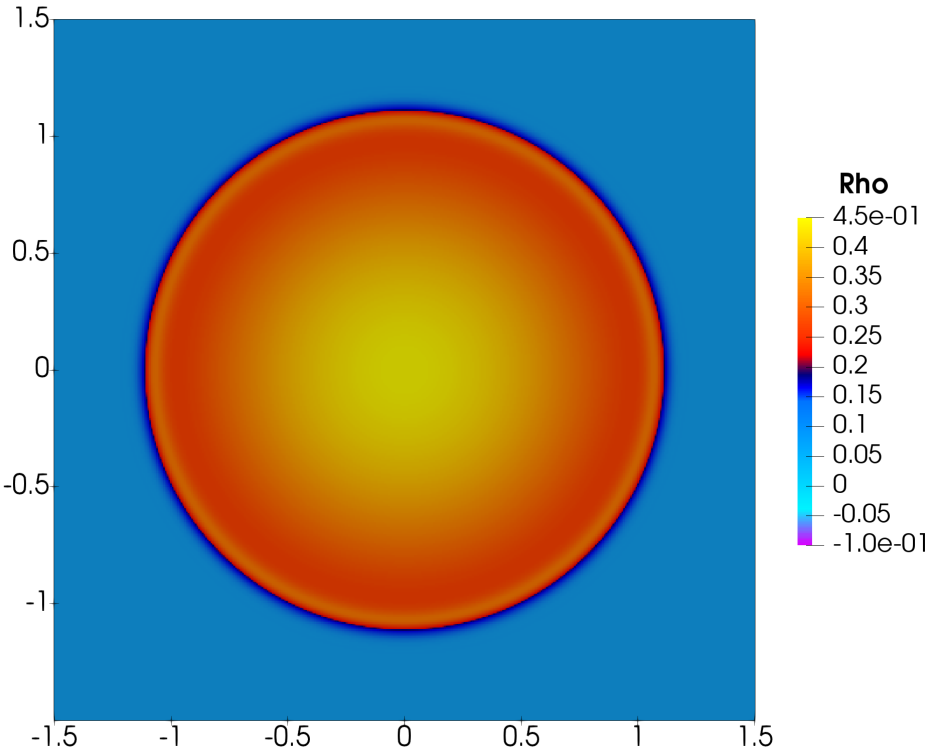

Figure 2.2: The exact solution of radiation density, ρ, for the line source benchmark using $\sigma_s = 1$ at time $t = 1.0$

distributed isotropically along an infinite line in space and move through a material medium with constant scattering. The exact solution of the line source problem is derived by Ganapol [9]. By approximating the initial pulse of radiation by a steep Gaussian, the initial condition used in this work is,

$$\mathcal{F} = \max\left(\frac{1}{2\pi\omega^2}e^{-(x^2+y^2)/(\omega^2)}, 10^{-3}\right) , \tag{2.28}$$

with $\omega = 0.03$. The constant ω is a smoothing parameter controlling the steepness of the Gaussian initial condition. This smoothed initial condition is used to remove numerical artifacts due to spacial discretization errors on the cartesian grid. Figure 2.2, shows the exact solution to the line source problem at a final time, $t_{\text{final}} = 1.0$ using a scattering intensity of $\sigma_s = 1.0$. This solution will be used as a reference throughout this thesis. All the solutions of the line-source benchmark presented in this work are computed using the initial conditions presented above with $\omega = 0.03$ and using a grid of 400 by 400 cells unless specified otherwise. The numerical

method is described in detail in Section 4.0.1.

2.4 The Spherical-Harmonics Closures, P_N

One family of moment methods for radiation modelling is known as the spherical harmonics method [10, 26, 3, 2]. The method of spherical harmonics is based on an assumed form of the distribution function that is an expansion in terms of the spherical harmonics. This is a spectral method in velocity space that can be interpreted as a polynomial approximation to the distribution function on the unit sphere defining directions of particle travel. The resulting PDEs that govern the evolution of moments are linear and rotationally invariant. Unfortunately, they do not preserve positivity of solutions. This is because the assumed form (a polynomial) can easily be negative. It has also been found that, even for systems with a very large number of unknowns, spherical-harmonic-based methods can produce relatively poor results for many problems [10]. This family of moment methods is important since the new model presented in the present thesis recovers similar behavior under certain conditions.

2.4.1 Spherical Harmonics General Definition

Spherical harmonics are a special set of functions defined on the surface of a sphere. They are often used to solve partial differential equations in many scientific fields, namely in quantum physics, computer graphics, chemistry and many other application. Similar to how circular functions (sines and cosines) are used to describe functions on a circle through a Fourier series, spherical harmonics are a complete set of orthogonal functions on the sphere. Since they are a set of orthogonal functions, they are often used as a basis to represent functions defined on a curved surface [7]. In general, a harmonic is a function that satisfies Laplace's

equation in spherical coordinates,

$$\nabla^2 f = \frac{1}{r^2}\frac{\partial}{\partial r}\left(r^2\frac{\partial f}{\partial r}\right) + \frac{1}{r^2\sin\theta}\frac{\partial}{\partial\theta}\left(\sin\theta\frac{\partial f}{\partial\theta}\right) + \frac{1}{r^2\sin^2\theta}\frac{\partial^2 f}{\partial\phi^2} = 0\,. \tag{2.29}$$

The solution to Laplace's equation, Eq. (2.29), is traditionally defined as $Y_l^m(\theta,\phi)$, and give by

$$Y_l^m(\theta,\phi) = (-1)^m\sqrt{\frac{(2l+1)}{4\pi}\frac{(l-m)!}{(l+m)!}}P_l^m(\cos\theta)e^{-im\phi}\,, \tag{2.30}$$

$$\text{for} \quad \begin{cases} l = 0, 1, 2, 3, \cdots \\ m = -l, -l+1, \cdots l-1, l \end{cases}, \tag{2.31}$$

where, $P_l^m(\cos\theta)$ is the associated Legendre polynomial in $\cos\theta$. The spherical harmonics functions are linearly independent. Furthermore, there does not exist any function of θ and ϕ that is orthogonal to all the harmonics for the range of l and m shown above. Thus, any well-behaved function existing on the surface of a sphere can be written as,

$$f(\theta,\phi) = \sum_{l=0}^{N}\sum_{l}^{m=-l} a_{lm}Y_l^m(\theta,\phi)\,, \tag{2.32}$$

where, a_{lm} is a constant. The spherical harmonics for $l = 1, 2, 3$ are listed bellow,

$$
\begin{aligned}
l = 0 : \quad & \begin{cases} Y_0^0(\theta,\phi) = \frac{1}{\sqrt{4\pi}}\,, \end{cases} \\
l = 1 : \quad & \begin{cases} Y_1^{-1}(\theta,\phi) = \frac{1}{2}\sqrt{\frac{3}{2\pi}}\sin\theta e^{-i\phi}\,, \\ Y_1^{0}(\theta,\phi) = \sqrt{\frac{3}{4\pi}}\cos\theta\,, \\ Y_1^{1}(\theta,\phi) = -\sqrt{\frac{3}{8\pi}}\sin\theta e^{i\phi}\,, \end{cases} \\
l = 2 : \quad & \begin{cases} Y_2^{-2}(\theta,\phi) = \frac{1}{4}\sqrt{\frac{15}{2\pi}}\sin^2\theta e^{-2i\phi}\,, \\ Y_2^{-1}(\theta,\phi) = \frac{1}{2}\sqrt{\frac{15}{2\pi}}\sin\theta\cos\theta e^{-i\phi}\,, \\ Y_2^{0}(\theta,\phi) = \frac{1}{2}\sqrt{\frac{5}{4\pi}}(3\cos^2\theta - 1)\,, \\ Y_2^{1}(\theta,\phi) = -\sqrt{\frac{15}{8\pi}}\sin\theta\cos\theta e^{i\phi}\,, \\ Y_2^{2}(\theta,\phi) = \frac{1}{4}\sqrt{\frac{15}{2\pi}}\sin^2\theta e^{2i\phi}\,. \end{cases}
\end{aligned}
$$

For radiative transport, the velocity distribution function, $\mathcal{F}(x_i, \Omega_i, t)$, can be approximated as a series of spherical harmonics,

$$\mathcal{F}(x_i, \Omega_i, t) = \sum_{l=0}^{N} \sum_{l}^{m=-l} a_{lm}(x_i, t) Y_l^m(\Omega_i)\,. \tag{2.33}$$

Since the velocity space is defined as a sphere, the use of spherical harmonics to approximate the distribution function is convenient and mathematically elegant. The moments can then be obtained by integrating the distribution function over all angles. Although, there is no physical limit to the number of harmonics that can be added to the distribution function, for practical calculations a finite N value is assigned. It is hoped that higher accuracy is obtained for higher values of N. Although this is generally observed, it cannot be proven or guaranteed for all cases.

2.4.2 The P_1 Closure

In order to illustrate the method of moment as applied to the spherical-harmonics closure, the first member of the hierarchy is derived. For the P_1 closure, the distribution function $\mathcal{F}(x_i, \Omega_i, t)$ is constructed using 0^{th}-order and 1^{st}-order spherical-harmonics. As mentioned earlier, the speed of light is non-dimensionalized such that $c = 1$, meaning that the velocity space is restricted to a unit sphere. As shown above, the 0^{th}-order harmonic is simply a constant and the three first-order harmonics are linear function of v_i. The assumed form of the distribution function $\mathcal{F}(x_i, \Omega_i, t)$ is therefore,

$$\mathcal{F}_{P_1}(x_i, \Omega_i, t) = \beta + \alpha_x v_x + \alpha_y v_y + \alpha_z v_z \,. \tag{2.34}$$

Since the studied density distribution function only has four unknowns, $(\alpha_x \,, \alpha_y \,, \alpha_z \,, \beta)$, the first two moments will provide enough information to completely define the system. As shown before, the first two moments are defined as,

$$U_0 = \langle \mathcal{F} \rangle = \rho \,, \qquad\qquad U_i = \langle v_i \mathcal{F} \rangle = \rho u_i \,. \tag{2.35}$$

They represent the particle density, ρ, and the momentum density, ρu_i, respectively. Again, u_i is the bulk velocity of the system. The distribution function can be rewritten using the standard spherical notation as follows,

$$\mathcal{F}_{P_1}(x_i, \Omega_i, t) = \alpha_x \sin\phi \cos\theta + \alpha_y \sin\phi \sin\theta + \alpha_z \cos\phi + \beta \,. \tag{2.36}$$

In order to find the four unknowns, moments of the distribution function are needed. The moments will have the form presented in Eq. (2.7). The first integral is associated with the 0^{th}-order moment, thus the velocity-related weight, $W(v_i)$, is taken to be 1. The other integrals are the three different components of the 1st-order moment. Their velocity-related weight, $W(v_i)$, are taken as $\sin\phi\cos\theta$,

$\sin\phi\sin\theta$ and $\cos\phi$ respectively. This yields

$$\begin{aligned}
\iint_{\Omega_i} (\alpha_x \sin\phi\cos\theta + \alpha_y \sin\phi\sin\theta + \alpha_z \cos\phi + \beta)\sin\phi \; \mathrm{d}\Omega_i &= \rho\,, \\
\iint_{\Omega_i} \sin\phi\cos\theta(\alpha_x \sin\phi\cos\theta + \alpha_y \sin\phi\sin\theta + \alpha_z \cos\phi + \beta)\sin\phi \; \mathrm{d}\Omega_i &= \rho u_x\,, \\
\iint_{\Omega_i} \cos\phi\cos\theta(\alpha_x \sin\phi\cos\theta + \alpha_y \sin\phi\sin\theta + \alpha_z \cos\phi + \beta)\sin\phi \; \mathrm{d}\Omega_i &= \rho u_y\,, \\
\iint_{\Omega_i} \cos\phi(\alpha_x \sin\phi\cos\theta + \alpha_y \sin\phi\sin\theta + \alpha_z \cos\phi + \beta)\sin\phi \; \mathrm{d}\Omega_i &= \rho u_z\,.
\end{aligned}$$

After evaluating these integrals, the distribution function coefficients needed to ensure consistency with the known moments are found to be,

$$\begin{aligned}
4\pi\beta = \rho \qquad &\text{or} \qquad \beta = \frac{\rho}{4\pi}\,, \\
\frac{4\pi\alpha_x}{3} = \rho u_x \qquad &\text{or} \qquad \alpha_x = \frac{3\rho u_x}{4\pi}\,, \\
\frac{4\pi\alpha_y}{3} = \rho u_y \qquad &\text{or} \qquad \alpha_y = \frac{3\rho u_y}{4\pi}\,, \\
\frac{4\pi\alpha_z}{3} = \rho u_z \qquad &\text{or} \qquad \alpha_z = \frac{3\rho u_z}{4\pi}\,.
\end{aligned}$$

The solutions found are obviously simple. In fact the first coefficient β is shown to be the density of particles divided by the surface area of the unit sphere. The last three coefficients $(\alpha_x\,, \alpha_y\,, \alpha_z)$ are perfectly symmetric and are related to the momentum density in each of the three spatial directions. Finally, using this new information, the assumed form of the distribution function can be written in its complete form as,

$$\mathcal{F}_{P_1}(x_i, \Omega_i, t) = \frac{\rho}{4\pi} + \frac{3\rho u_x}{4\pi}\,\sin\phi\cos\theta + \frac{3\rho u_y}{4\pi}\,\sin\phi\sin\theta + \frac{3\rho u_z}{4\pi}\,\cos\phi\,. \quad (2.37)$$

It is important to note that both ρ and u_i remain functions of x_i and t. In order to predict the time evolution of the distribution function, moments of the radiative-transport equation are needed. As shown previously, the moments of the

radiative-transport equation have the following form,

$$\frac{\partial}{\partial t}\langle W\mathcal{F}\rangle + \frac{\partial}{\partial x_i}\langle W\, v_i\,\mathcal{F}\rangle = \langle W\, S\rangle \ .$$

The second term of the left hand side of the equation, $\langle W\, v_i\,\mathcal{F}\rangle$, represent the divergence of the flux of the first left-hand-side term, $\langle W\mathcal{F}\rangle$. This differential equation can expanded as,

$$\frac{\partial}{\partial t}\langle W\mathcal{F}\rangle + \frac{\partial}{\partial x}\langle W\, v_x\,\mathcal{F}\rangle + \frac{\partial}{\partial y}\langle W\, v_z\,\mathcal{F}\rangle + \frac{\partial}{\partial z}\langle W\, v_z\,\mathcal{F}\rangle = \langle W\, S\rangle \ . \qquad (2.38)$$

where the terms $\langle W\, v_x\,\mathcal{F}\rangle$, $\langle W\, v_z\,\mathcal{F}\rangle$, and $\langle W\, v_z\,\mathcal{F}\rangle$ represent the fluxes in the x, y, and z directions respectively. In order to obtain a complete description of the system behavior, the two first moments of the radiative-transport equation need to be evaluated. The 0^{th}-order moment is represented by the following partial differential equation (PDE), again where the weight W is equal to 1 and the function $\mathcal{F}$ is defined by Eq. (2.37),

$$\frac{\partial}{\partial t}\langle\mathcal{F}\rangle + \frac{\partial}{\partial x}\langle\, v_x\,\mathcal{F}\rangle + \frac{\partial}{\partial y}\langle\, v_y\,\mathcal{F}\rangle + \frac{\partial}{\partial z}\langle\, v_z\,\mathcal{F}\rangle = \langle\sigma_s(E-\mathcal{F}) + \sigma_e E - \sigma_a\mathcal{F}\rangle \ .$$

The 1^{st}-order moment of the radiative-transport equation gives the following PDEs,

$$\begin{aligned}
&\frac{\partial}{\partial t}\langle v_x\mathcal{F}\rangle + \frac{\partial}{\partial x}\langle\, v_x v_x\,\mathcal{F}\rangle + \frac{\partial}{\partial y}\langle\, v_x v_y\,\mathcal{F}\rangle + \frac{\partial}{\partial z}\langle\, v_x v_z\,\mathcal{F}\rangle = \langle v_x(\sigma_s(E-\mathcal{F}) + \sigma_e E - \sigma_a\mathcal{F})\rangle \ ,\\
&\frac{\partial}{\partial t}\langle v_y\mathcal{F}\rangle + \frac{\partial}{\partial x}\langle\, v_y v_x\,\mathcal{F}\rangle + \frac{\partial}{\partial y}\langle\, v_y v_y\,\mathcal{F}\rangle + \frac{\partial}{\partial z}\langle\, v_y v_z\,\mathcal{F}\rangle = \langle v_y(\sigma_s(E-\mathcal{F}) + \sigma_e E - \sigma_a\mathcal{F})\rangle \ ,\\
&\frac{\partial}{\partial t}\langle v_z\mathcal{F}\rangle + \frac{\partial}{\partial x}\langle\, v_z v_x\,\mathcal{F}\rangle + \frac{\partial}{\partial y}\langle\, v_z v_y\,\mathcal{F}\rangle + \frac{\partial}{\partial z}\langle\, v_z v_z\,\mathcal{F}\rangle = \langle v_z(\sigma_s(E-\mathcal{F}) + \sigma_e E - \sigma_a\mathcal{F})\rangle \ .
\end{aligned}$$

After integrating over all velocity space, as demonstrated earlier, the resulting PDEs governing the time evolution of the system can be written as

$$\frac{\partial}{\partial t}\rho + \frac{\partial}{\partial x}\rho u_x + \frac{\partial}{\partial y}\rho u_y + \frac{\partial}{\partial z}\rho u_z = \rho(\sigma_e - \sigma_a)\,, \tag{2.39}$$

$$\frac{\partial}{\partial t}\rho u_x + \frac{\partial}{\partial x}\frac{\rho}{3} = -(\sigma_s + \sigma_a)\rho u_x\,, \tag{2.40}$$

$$\frac{\partial}{\partial t}\rho u_y + \frac{\partial}{\partial y}\frac{\rho}{3} = -(\sigma_s + \sigma_a)\rho u_y\,, \tag{2.41}$$

$$\frac{\partial}{\partial t}\rho u_z + \frac{\partial}{\partial z}\frac{\rho}{3} = -(\sigma_s + \sigma_a)\rho u_z\,. \tag{2.42}$$

The first equation can be referred to as the continuity equation, while the last equations describe the average of the particle velocities in all three physical dimensions.

2.4.3 Solution of the Line Source Problem Using the P_1 Closure

Figure 2.3 shows the solution to the line-source problem using this first-order spherical-harmonics closure. Note that for this simulation the scattering intensity was set to $\sigma_s = 1.0$. The P_1 closure would not be used for any serious calculations but the major downside of this method is obvious to see. As one can see, the solution shown in Figure 2.3 present a huge region of negative particle density (shown in pink), also the P_1 closure does not recover the right radiation speed. Since the speed of light is taken to be $c = 1.0$, after a non-dimensional time of $t = 1.0$ the radiation front should have traveled a non-dimensional distance of 1. This is not observed in the result.

2.5 The Discrete Ordinates Closures, S_N

The discrete-ordinates models are used in many scientific fields. Their simplicity make them very easy to implement and relatively inexpensive to compute [10, 3, 11, 16, 25]. Though not usually written as a moment method, expressing

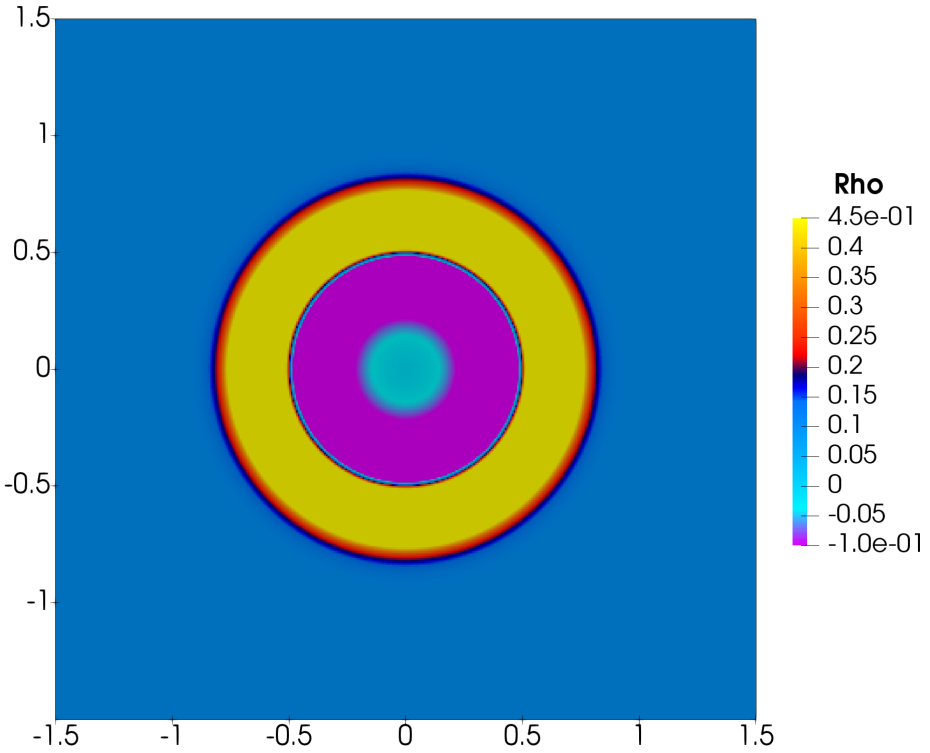

Figure 2.3: Radiation density, ρ, for the line-source benchmark, using the P_1 closure with $\sigma_s = 1$ at $t = 1.0$

them in this form is always possible and is done here for consistency.

The discrete ordinates models represent the distribution function with a collocation method using quadrature sets on the unit sphere [10]. Since the velocity space of all radiative transport methods is represented to be a unit sphere, as mentioned in the previous section, this method is particularly suitable. The results of such a quadrature in velocity space is that photons are only permitted to move in a set of prescribed direction specified by the chosen quadrature.

The assumed form of the distribution function is taken to be,

$$\mathcal{F} = \sum_{l=0}^{\#\text{ direction}} w^{(l)}\, c\, \delta(\Omega_i - \hat{\Omega}_i^{(l)})\,, \tag{2.43}$$

where $\hat{\Omega}_i^{(l)}$ is the l^{th} chosen direction and $w^{(l)}$ is the corresponding weight required for agreement with Eq. (2.8). Moments of such a distribution function are simple

to evaluate as,

$$\langle \mathcal{F} \rangle = \sum_{l=0}^{\#\text{ direction}} w^{(l)} \,, \tag{2.44}$$

$$\langle v_i \mathcal{F} \rangle = \sum_{l=0}^{\#\text{ direction}} w^{(l)}\, c\, \hat{\Omega}_i^{(l)} \,, \tag{2.45}$$

$$\langle v_i v_j \mathcal{F} \rangle = \sum_{l=0}^{\#\text{ direction}} w^{(l)}\, c^2\, \hat{\Omega}_i^{(l)} \hat{\Omega}_j^{(l)} \,, \tag{2.46}$$

$$\langle v_i v_j v_k \mathcal{F} \rangle = \sum_{l=0}^{\#\text{ direction}} w^{(l)}\, c^3\, \hat{\Omega}_i^{(l)} \hat{\Omega}_j^{(l)} \hat{\Omega}_k^{(l)} \,. \tag{2.47}$$

Obviously this method requires a huge number of discrete directions to be accurate and can rapidly become computationally expensive. Furthermore, this method does not guaranty a positive particle density, but it does preserve it. For a given initial condition, if all initial weights, $w^{(l)}$, are found to be positive, the solution is guaranteed to remain positive. However, if one or more weights are initially negative this method can easily predict regions of negative particle density. Finally, due to the assumed form of the distribution function, the solutions are not rotationally invariant. Even when using a quadrature with a huge number of points, the solutions display spurious rays of radiation. This well known artifact is called the ray effect [21].

2.5.1 The S_1 Closure

In order to fully illustrate the method, the first-order member of the S_N hierarchy is derived. Similar to the first-order member of the spherical-harmonics model, the distribution function associated with the S_1 model has only four unknowns, thus it requires a quadrature rule using four chosen directions. The understanding of this example is crucial since the first member of the new model hierarchy, that is the main topic of this thesis, uses a quadrature rule based on this strategy. The four chosen velocities are denoted as $v_i^{(1)}$, $v_i^{(2)}$, $v_i^{(3)}$, and $v_i^{(4)}$. In order to cover as much moment space as possible, the four quadrature points are chosen to be evenly spaced on the unit sphere representing velocity space. One can visualize

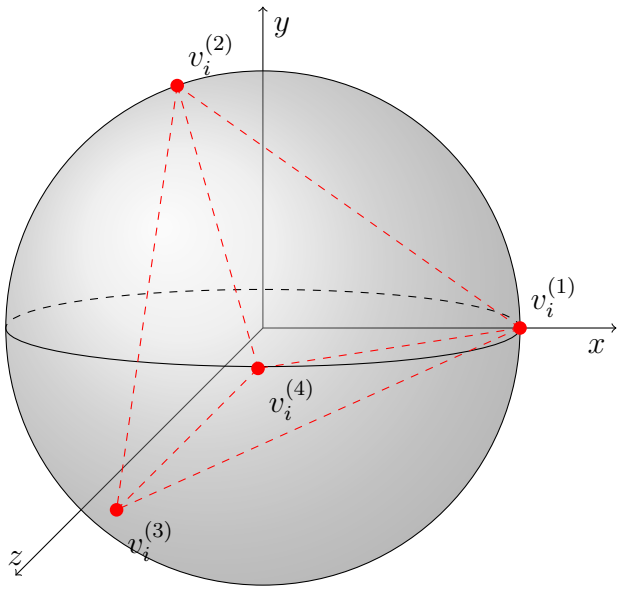

Figure 2.4: S_1 quadrature points on the velocity space

this arrangment by imagining a methane molecule or the apex of a tetrahedron as shown in Figure 2.4. Where the exact coordinates ($v_i^{(1)}$, $v_i^{(2)}$, $v_i^{(3)}$, $v_i^{(4)}$) used are

$$v_i^{(1)} = \begin{pmatrix} 1 \\ 0 \\ 0 \end{pmatrix}, \quad v_i^{(2)} = \begin{pmatrix} \cos(2\theta) \\ \sin(2\theta) \\ 0 \end{pmatrix}, \quad v_i^{(3)} = \begin{pmatrix} \cos(\pi-\theta) \\ -\sin(\pi-\theta) \\ \sin(\theta) \end{pmatrix}, \quad v_i^{(4)} = \begin{pmatrix} \cos(\pi-\theta) \\ -\sin(\pi-\theta) \\ -\sin(\theta) \end{pmatrix},$$

with $\theta = \arccos(1/\sqrt{3})$. One can see that the 0^{th} and 1^{st} moments, as shown in Eqs. (2.44) and (2.45), can be expressed in vector form as,

$$\boldsymbol{Q}\,\boldsymbol{W} = \boldsymbol{U}\,, \tag{2.48}$$

with the definitions

$$\boldsymbol{Q} = \begin{bmatrix} 1 & 1 & 1 & 1 \\ v_x^{(1)} & v_x^{(2)} & v_x^{(3)} & v_x^{(4)} \\ v_y^{(1)} & v_y^{(2)} & v_y^{(3)} & v_y^{(4)} \\ v_z^{(1)} & v_z^{(2)} & v_z^{(3)} & v_z^{(4)} \end{bmatrix}, \quad \boldsymbol{W} = \begin{bmatrix} w^{(1)} \\ w^{(2)} \\ w^{(3)} \\ w^{(4)} \end{bmatrix} \quad \text{and} \quad \boldsymbol{U} = \begin{bmatrix} U_0 \\ U_x \\ U_y \\ U_z \end{bmatrix}. \tag{2.49}$$

If one knows the values of the moments in $\boldsymbol{U}$, the distribution function weights, $w^{(l)}$, are found using the following relation,

$$\begin{bmatrix} w^{(1)} \\ w^{(2)} \\ w^{(3)} \\ w^{(4)} \end{bmatrix} = \begin{bmatrix} 1 & 1 & 1 & 1 \\ v_x^{(1)} & v_x^{(2)} & v_x^{(3)} & v_x^{(4)} \\ v_y^{(1)} & v_y^{(2)} & v_y^{(3)} & v_y^{(4)} \\ v_z^{(1)} & v_z^{(2)} & v_z^{(3)} & v_z^{(4)} \end{bmatrix}^{-1} \begin{bmatrix} U_0 \\ U_x \\ U_y \\ U_z \end{bmatrix} . \tag{2.50}$$

The flux dyad for this system, F_i can be expressed in vector form as,

$$\boldsymbol{F}_i = \boldsymbol{Z}_i \boldsymbol{W} , \tag{2.51}$$

with,

$$\boldsymbol{F}_i = \begin{bmatrix} U_i \\ U_{xi} \\ U_{yi} \\ U_{zi} \end{bmatrix} \quad \text{and} \quad \boldsymbol{Z} = \begin{bmatrix} v_i^{(1)} & v_i^{(2)} & v_i^{(3)} & v_i^{(4)} \\ v_i^{(1)} v_x^{(1)} & v_i^{(2)} v_x^{(2)} & v_i^{(3)} v_x^{(3)} & v_i^{(4)} v_x^{(4)} \\ v_i^{(1)} v_y^{(1)} & v_i^{(2)} v_y^{(2)} & v_i^{(3)} v_y^{(3)} & v_i^{(4)} v_y^{(4)} \\ v_i^{(1)} v_z^{(1)} & v_i^{(2)} v_z^{(2)} & v_i^{(3)} v_z^{(3)} & v_i^{(4)} v_z^{(4)} \end{bmatrix} . \tag{2.52}$$

Ultimately, it is possible to write the fluxes as linear functions of the moments, U,

$$\boldsymbol{F}_i = \boldsymbol{Z}_i \boldsymbol{Q}^{-1} \boldsymbol{U} . \tag{2.53}$$

The matrices, $\boldsymbol{Z}_i$ and $\boldsymbol{Q}^{-1}$, depend only on the chosen quadrature rule. Therefore, they can be precomputed and remain constant throughout the calculation.

2.5.2 Solution of the Line Source Problem Using the S_1 Closure

Figure 2.5, shows the solution to the line-source problem using a scattering intensity, $\sigma_s = 1.0$ at time $t = 1.0$. Only four directions are obviously far less that would be used in any serious calculation, however the main characteristics of the

discrete-ordinates closures can be observed.

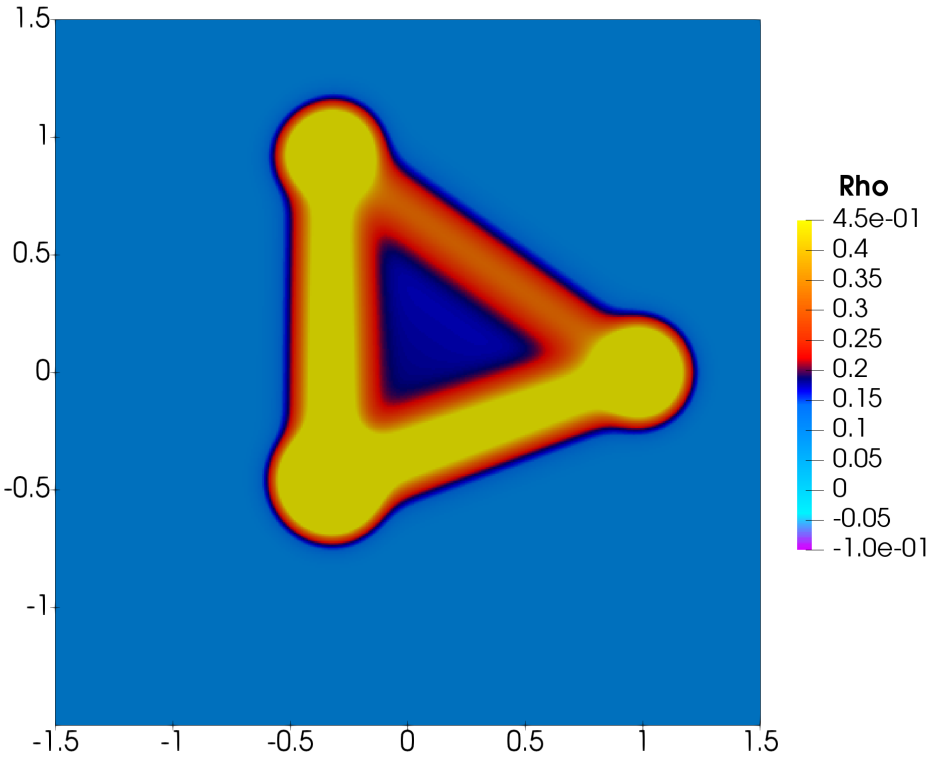

Figure 2.5: Radiation density, ρ, for the line source benchmark using the S_1 closure with $\sigma_s = 1$ at time $t = 1.0$

As one can see, the S_1 closure maintain positivity of the solution. As expected, it is far form being rotationally invariant but the radiation speed is correctly captured. This simple four-direction model serves as the base of the new family of models for radiation transport presented in the next chapter.

2.6 The Maximum-Entropy Closures, M_N

Instead of using polynomials or a sum of delta functions to approximate the form of the distribution function, $\mathcal{F}(x_i, \Omega_i, t)$, the maximum-entropy closures choose the function which maximizes the entropy while agreeing with a finite set of velocity moments [18]. Maximum-entropy moment closure has been successful in the field of gaskinetic theory due to their ability to predict with relatively good accuracy the behavior of gaseous flow using a limited number of moments [18, 3, 4, 5]. The M_N hierarchy is attractive since it ensure non-negativity of the radiation den-

sity and produces a system of hyperbolic PDEs which guaranties that the moments are physically realizable. Unfortunately, for all but the lowest-order members of this hierarchy, the M_1 closure, these models cannot be written in closed form. This means that, whenever a flux is needed, an expensive and ill-conditioned entropy-maximization problem must be solved numerically. This entropy-maximization requires many integrals that must be accurately evaluated using quadratures, leading to huge expense [18].

2.6.1 The Maximum-Entropy Distribution Function

In order to construct the maximum-entropy moment method for radiative transfer, it is first necessary to determine the distribution function which maximizes the entropy while remaining in agreement with the specific moments, $\boldsymbol{U}$. The radiative entropy density, given by the Bose-Einstein statistics, is known to be [8],

$$h(\mathcal{F}) = \frac{2\kappa\nu^2}{c^3}\left[(n+1)\ln(n+1) - n\ln(n)\right] , \tag{2.54}$$
$$\text{with} \qquad n = \left(\frac{c^2}{2h\nu^3}\right)\mathcal{F} .$$

Here, n is the occupation number, h and κ are the Plank and the Boltzmann constants, respectively. The optimization problem can be formulated as,

$$\mathcal{F} = \max_{\mathcal{F}} \langle h(\mathcal{F}) \rangle , \tag{2.55}$$
$$\text{subject to} \qquad \langle W(v_i)\mathcal{F} \rangle = \boldsymbol{U} . \tag{2.56}$$

This constrained maximization problem can be solved using the technique of Lagrange multipliers. Using a vector of Lagrange multipliers, denoted $\boldsymbol{\alpha}$, one can write the optimization problem as,

$$\frac{dJ}{d\mathcal{F}} = 0 , \tag{2.57}$$

where, J is a new functional defined as,

$$J = \left\langle \frac{2\kappa\nu^2}{c^3} \left[(n+1)\ln(n+1) - n\ln(n) \right] \right\rangle - \boldsymbol{\alpha}^T (\boldsymbol{U} - \langle W(v_i)\mathcal{F} \rangle) \,. \tag{2.58}$$

The solution to this optimization problem is presented here for completeness although it is not important for the understanding of this research project.

One can first define $n = a\mathcal{F}$, where a is a constant defined as, $\frac{c^2}{2h\nu^3}$, for simplicity. This leads to,

$$\frac{dJ}{d\mathcal{F}} = \frac{d}{d\mathcal{F}} \left[\left\langle \frac{2\kappa\nu^2}{c^3} \left[(n+1)\ln(n+1) - n\ln(n) \right] \right\rangle - \boldsymbol{\alpha}^T (\boldsymbol{U} - \langle \boldsymbol{W}(v_i)\mathcal{F} \rangle) \right] = 0 \,,$$

$$\frac{d}{d\mathcal{F}} \left\langle \frac{2\kappa\nu^2}{c^3} \left[(n+1)\ln(n+1) - n\ln(n) \right] \right\rangle - \frac{d}{d\mathcal{F}} \left[\boldsymbol{\alpha}^T (\boldsymbol{U} - \langle \boldsymbol{W}(v_i)\mathcal{F} \rangle) \right] = 0 \,.$$

The vector of target moments, $\boldsymbol{U}$, is not a function of, $\mathcal{F}$,

$$\frac{d}{d\mathcal{F}} \left\langle \frac{2\kappa\nu^2}{c^3} \left[(n+1)\ln(n+1) - n\ln(n) \right] \right\rangle + \frac{d}{d\mathcal{F}} \left[\boldsymbol{\alpha}^T \langle \boldsymbol{W}(v_i)\mathcal{F} \rangle \right] = 0 \,.$$

This leads to,

$$\frac{d}{d\mathcal{F}} \left[\frac{2\kappa\nu^2}{c^3} \left[(a\mathcal{F}+1)\ln(a\mathcal{F}+1) - a\mathcal{F}\ln a\mathcal{F} \right] + \boldsymbol{\alpha}^T \boldsymbol{W}(v_i)\mathcal{F} \right] = 0 \,,$$

$$\frac{2\kappa\nu^2}{c^3} \left[a\ln(a\mathcal{F}+1) - a\ln(a\mathcal{F}) \right] + \boldsymbol{\alpha}^T \boldsymbol{W}(v_i) = 0 \,.$$

From there, it is possible to solve for $\mathcal{F}$ as follows,

$$\frac{2\kappa\nu^2}{c^3} \left[a\ln(a\mathcal{F}+1) - a\ln(a\mathcal{F}) \right] = -\boldsymbol{\alpha}^T \boldsymbol{W}(v_i) \,,$$

$$\ln(a\mathcal{F}+1) - \ln(a\mathcal{F}) = -\boldsymbol{\alpha}^T \boldsymbol{W}(v_i) \left(\frac{ch\nu}{\kappa} \right) \,,$$

$$\mathcal{F} = \frac{1}{a} \left(\exp\left(-\boldsymbol{\alpha}^T \boldsymbol{W}(v_i) \left(\frac{ch\nu}{\kappa} \right) \right) - 1 \right)^{-1} \,.$$

The final form of the distribution function is found to be,

$$\mathcal{F} = \frac{2h\nu^3}{c^2}\left(\exp\left(-\boldsymbol{\alpha}^T\boldsymbol{W}(v_i)\left(\frac{ch\nu}{\kappa}\right)\right)-1\right)^{-1}. \tag{2.59}$$

Unfortunately, as mentioned before, Eq. 2.59 cannot be integrated in closed form on the sphere if the velocity weights, $W(v_i)$, contain terms that are higher than first order. This is the greatest limitation of this method.

2.6.2 The M_1 Closure

Following the same method shown for the two previous closures, it is required to take moments of the M_1 distribution function, Eq. (2.59), according to the following relations,

$$\rho = U_0 = \langle\mathcal{F}\rangle\ , \qquad \rho u_i = U_i = \langle v_i\mathcal{F}\rangle\ , \tag{2.60}$$

one can write the two-dimensional form of the conservation equations as,

$$\frac{\partial \boldsymbol{U}}{\partial t} + \frac{\partial \boldsymbol{F_x}}{\partial x} + \frac{\partial \boldsymbol{F_y}}{\partial y} = \boldsymbol{S}\,, \tag{2.61}$$

where

$$\boldsymbol{U} = \begin{bmatrix} \rho \\ \rho u_x \\ \rho u_y \end{bmatrix},\ \boldsymbol{F_x} = \begin{bmatrix} \rho u_x \\ U_{xx} \\ U_{xy} \end{bmatrix},\ \boldsymbol{F_y} = \begin{bmatrix} \rho u_y \\ U_{yx} \\ U_{yy} \end{bmatrix}, \tag{2.62}$$

and the source term, $\boldsymbol{S}$, as shown before, is defined as,

$$\boldsymbol{S} = \begin{bmatrix} \rho(\sigma_e - \sigma_a) \\ -(\sigma_s + \sigma_a)\rho u_x \\ -(\sigma_s + \sigma_a)\rho u_y \end{bmatrix}, \tag{2.63}$$

The full derivation of the M_1 closure is not presented in this work since it is not necessary for the understanding of the new model. However, by integrating the distribution function over velocity space with the corresponding velocity related weights, one finds the fluxes, $\boldsymbol{F_x}$ and $\boldsymbol{F_y}$ as,

$$\boldsymbol{F_x} = \begin{bmatrix} \rho u_x \\ \left(\frac{1-\chi}{2} + \frac{3\chi-1}{2}\frac{u_x^2}{u_x^2+u_y^2}\right)\rho \\ \left(\frac{3\chi-1}{2}\frac{u_x u_y}{u_x^2+u_y^2}\right)\rho \end{bmatrix}, \quad \boldsymbol{F_y} = \begin{bmatrix} \rho u_y \\ \left(\frac{3\chi-1}{2}\frac{u_x u_y}{u_x^2+u_y^2}\right)\rho \\ \left(\frac{1-\chi}{2} + \frac{3\chi-1}{2}\frac{u_y^2}{u_x^2+u_y^2}\right)\rho \end{bmatrix}, \tag{2.64}$$

where, χ is the Eddington factor [7]. This factor can be expressed in different forms, however for the M_1 closure, it is generally written as,

$$\chi = \frac{3 + 4(u_x^2 + u_y^2)}{5 + 2\xi}, \quad \xi = \sqrt{4 - 3(u_x^2 + u_y^2)}\,. \tag{2.65}$$

2.6.3 Solution to the line source problem using the M_1 closure

Figure 2.6 shows the solution to the line-source benchmark using a scattering intensity, $\sigma_s = 1$, obtained using the M_1 model. As expected, the solution is rotationally invariant and preserves positivity. However it is still a relatively bad approximation to the exact solution presented in Figure 2.2.

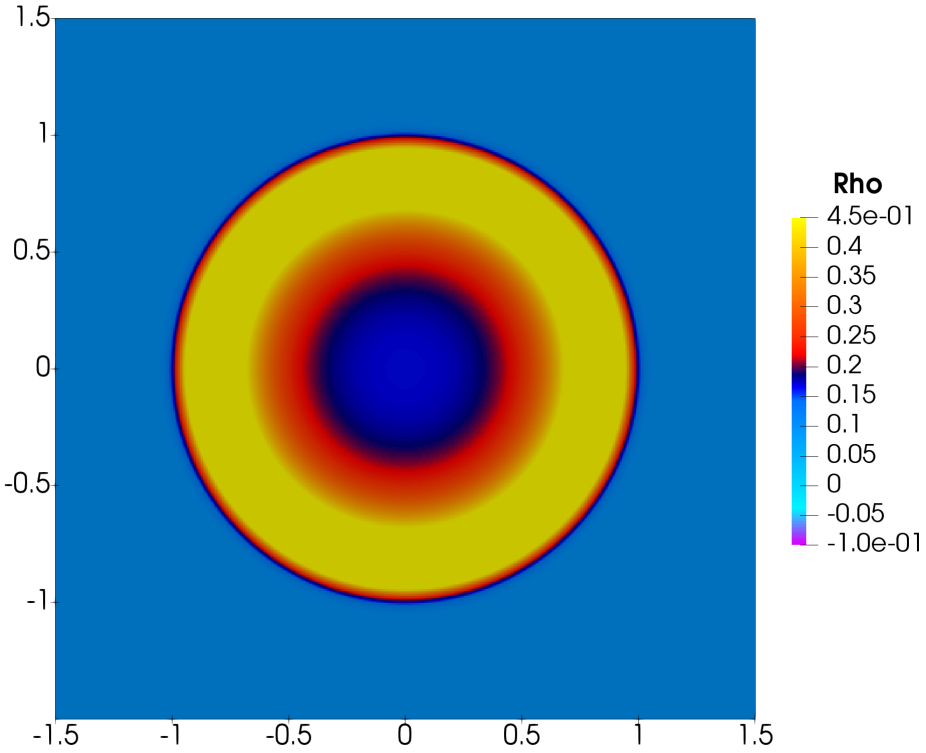

Figure 2.6: Radiation density, ρ, for the line source benchmark using the M_1 closure with $\sigma_s = 1$ at $t = 1.0$

Chapter 3

A New Model

The main goal of this thesis is to develop a new hierarchy of radiative transport models. As seen in the previous chapter, the spherical-harmonics, discrete-ordinates and maximum-entropy based models present some important limitations that greatly restrict their applicability. The spherical-harmonics closures, due to the assumed form of its distribution function, do not preserve positivity of the solution. The discrete-ordinates model preserves positivity but does not produce rotationally invariant solutions and can be prohibitively expensive. Even when using nearly a thousand quadrature points, the solutions display ray effects [10]. Finally, the maximum-entropy closure features many desirable mathematical properties, however for all but the lowest-order members of the hierarchy, the M_1 model, these models cannot be written in closed form. In other words, the analytical solution of the distribution function, $\mathcal{F}$, cannot be found.

In this chapter, the lowest-order member of a new Positive-Averaged-Quadratures hierarchy, PAQ_N, is derived and analyzed. This new model is designed to guarantee a positive particle density and is also believed to leave open the possibility of rotational invariance while limiting the computational cost.

3.1 The PAQ_1 closure

The construction of the first member of this hierarchy is based on a very low-order discrete-ordinates method (the S_1 closure shown in the previous chapter). The general idea is that, since each individual discrete-ordinates solution maintains positivity, a model that is the average of a large collection of discrete-ordinates models can also be made to maintain positivity. As for the S_1 closure above, the four directions are chosen such that the angles between each direction is equal. However, rather than using a single set of directions (quadrature points) for each flux calculation, this new model computes the fluxes by taking the average of a large number of sets of four such ordinates. For each of these sets, a methane-style quadrature is used. In other words, each time an inter-cell flux is needed, it is taken to be the average of the fluxes predicted by a large collection of discrete-ordinates representation. If enough orientations of the quadrature are taken the model will approach rotational invariance and hopefully maintain solution positivity.

The collection of quadrature representations are found by rotating the "initial" quadrature around the z-axis as pictured in Figure 3.1. During the initial investigation of this new closure technique, other more complicated 3D-rotations were tested. It was found that it is extremely difficult to evenly cover the velocity space using 3D-rotations of the "initial" quadrature. Some regions of the sphere would inevitably display a higher density of quadrature points thus leading to rotational asymmetry.

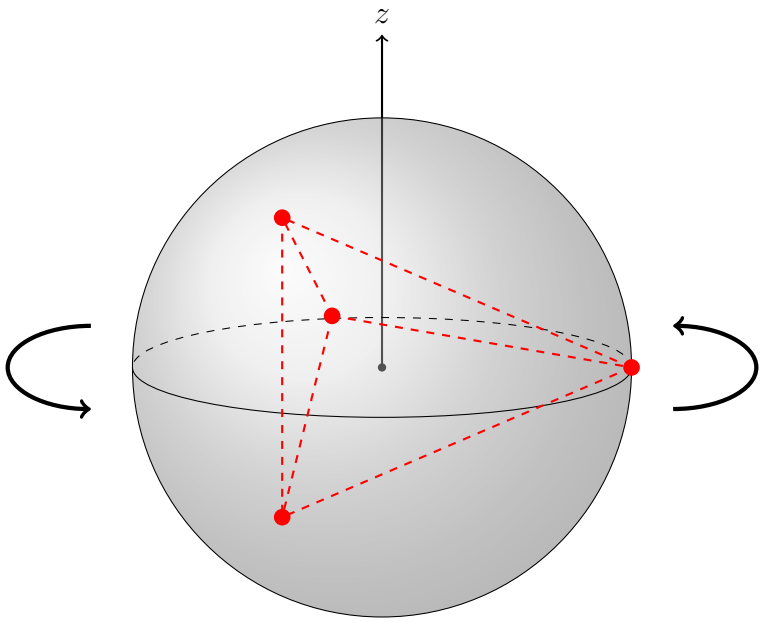

Figure 3.1: PAQ_1, Collection of quadrature points on the velocity space

As seen for the S_1 closure, the flux dyad predicted by one quadrature representation can be calculated as,

$$\boldsymbol{F}_i = \boldsymbol{Z}_i \boldsymbol{W}\,, \tag{3.1}$$

where, the weight vector, $\boldsymbol{W}$, and the matrix, $\boldsymbol{Z}_i$, are defined as,

$$\boldsymbol{W} = \begin{bmatrix} w^{(1)} \\ w^{(2)} \\ w^{(3)} \\ w^{(4)} \end{bmatrix} \quad \text{and} \quad \boldsymbol{Z} = \begin{bmatrix} v_i^{(1)} & v_i^{(2)} & v_i^{(3)} & v_i^{(4)} \\ v_i^{(1)}v_x^{(1)} & v_i^{(2)}v_x^{(2)} & v_i^{(3)}v_x^{(3)} & v_i^{(4)}v_x^{(4)} \\ v_i^{(1)}v_y^{(1)} & v_i^{(2)}v_y^{(2)} & v_i^{(3)}v_y^{(3)} & v_i^{(4)}v_y^{(4)} \\ v_i^{(1)}v_z^{(1)} & v_i^{(2)}v_z^{(2)} & v_i^{(3)}v_z^{(3)} & v_i^{(4)}v_z^{(4)} \end{bmatrix}. \tag{3.2}$$

It is important to note that the weight vector, $\boldsymbol{W}$, represent the number of photons moving in each specific direction. If the values of the moments contained in $\boldsymbol{U}$ are known, $\boldsymbol{W}$, can easily be found as

$$\boldsymbol{W} = \boldsymbol{Q}^{-1}\boldsymbol{U}\,, \tag{3.3}$$

where,

$$\boldsymbol{Q} = \begin{bmatrix} 1 & 1 & 1 & 1 \\ v_x^{(1)} & v_x^{(2)} & v_x^{(3)} & v_x^{(4)} \\ v_y^{(1)} & v_y^{(2)} & v_y^{(3)} & v_y^{(4)} \\ v_z^{(1)} & v_z^{(2)} & v_z^{(3)} & v_z^{(4)} \end{bmatrix}, \qquad \text{and} \qquad \boldsymbol{U} = \begin{bmatrix} U_0 \\ U_x \\ U_y \\ U_z \end{bmatrix}. \tag{3.4}$$

The flux dyad can finally be written in compact form as,

$$\boldsymbol{F}_i = \boldsymbol{Z}_i \boldsymbol{Q}^{-1} \boldsymbol{U} \tag{3.5}$$

This relation was already derived in the previous chapter. The new model calculates the inter-cell fluxes as the average of the fluxes predicted by a large collection of this simple four-points quadrature rule. The PAQ_1 closure flux dyad can thus be expressed as

$$\boldsymbol{F_i} = \frac{1}{N} \sum_{\xi=0}^{N} \left(Z_i Q^{-1} \right)^{(\xi)} \boldsymbol{U}\,, \tag{3.6}$$

where, N, is the total number of distinct quadrature sets (rotations around the z-axis) used in the flux calculation. Since the matrices Z_i and Q are only function of the quadrature locations in velocity space, the term $\left(\frac{1}{N} \sum_{\xi=0}^{N} \left(\boldsymbol{Z}_i \boldsymbol{Q}^{-1} \right)^{(\xi)} \right)$, can be precomputed and simply replaced by an equivalent 4x4 matrix denoted $\mathcal{A}_i$,

$$\boldsymbol{F_i} = \mathcal{A}_i \boldsymbol{U}\,,$$
$$\text{with} \qquad \mathcal{A}_1 = \frac{1}{N} \sum_{\xi=0}^{N} \left(\boldsymbol{Z}_i \boldsymbol{Q}^{-1} \right)^{(\xi)}\,.$$

In other words, each inter-cell flux can be calculated by a simple 4×4 matrix multiplication. Figure 3.2 shows the solution to the line source problem using this technique. The solution shown in Figure 3.2 is rotationally invariant, but, unfortunately, displays a large zone of negative particle density. In fact, this solution is very similar to the solution predicted by the first-order spherical-harmonics closure. Since both the P_1 and the PAQ_1 closure are linear with respect to $\boldsymbol{U}$, they

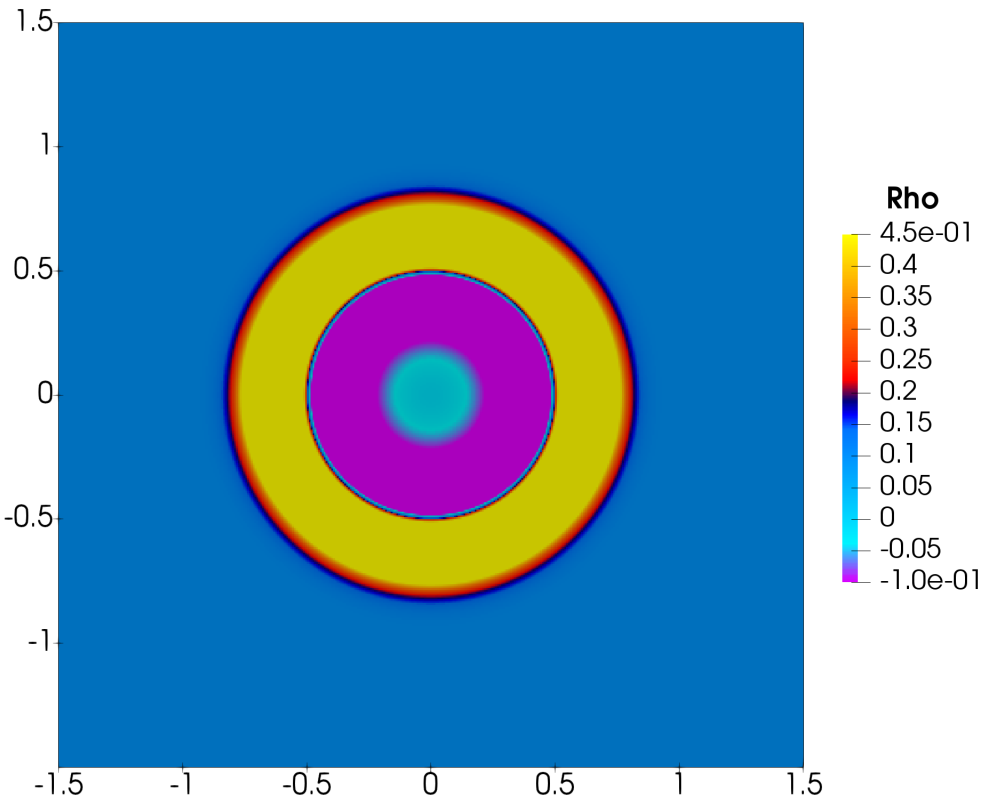

Figure 3.2: Radiation density, ρ, for the line source benchmark using the average of all quadratures of the PAQ_1 closure with $\sigma_s = 1.0$.

can be expressed as function of their respective flux Jacobian,

$$\boldsymbol{F_i} = \frac{\partial \boldsymbol{F_i}}{\partial \boldsymbol{U}} \boldsymbol{U} \, . \tag{3.7}$$

When a large number discrete quadratures are used the matrix $\mathcal{A}_i$ recovers perfectly the flux Jacobian of the P_1 closure. A more detailed explanation of the eigenstructure of each model is presented in Section 3.1.3. As explained before, the negative particle density is due to the fact that the discrete-ordinates methods do not guarantee positivity of the solution but only preserve it. For a given state $\boldsymbol{U}$, if all the initial weights, $w^{(l)}$, are found to be positive, the solution is guaranteed to remain positive. However, if one or more weights are negative this method can easily predict regions of negative particle density. One can imagine that a new "initial condition" is applied to each discrete-ordinates representation, if the current state cannot be represented by a discrete-ordinates representation,

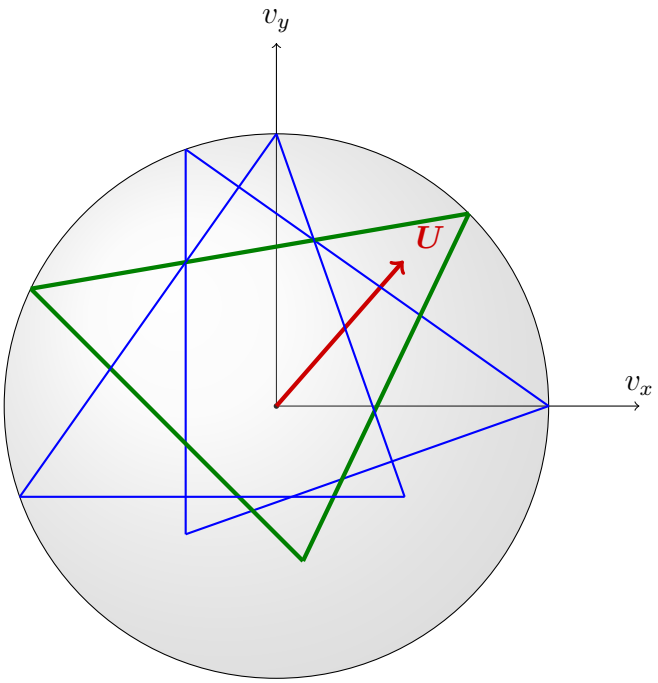

Figure 3.3: Projection of discrete-ordinates representations on a 2D velocity space

negative solutions can result.

Figure 3.3 shows a graphical representation of this phenomena. In this figure the tree-dimensional quadratures are projected onto the two-dimensional velocity space. The state $\boldsymbol{U}$, represented as a red arrow is also projected onto the velocity space and U_0 is assumed to be $U_0 = 1$ for the purpose of this example. If the state $\boldsymbol{U}$, is contained inside the quadrature, solutions are guaranteed to maintain positivity. In the example shown in Figure 3.3, only the green discrete-ordinate representation produces positive weights. Both other quadrature representations would require at least one weight to be negative, in order to remain consistent with the known moments, $\boldsymbol{U}$.

In order to overcome this problem, when computing a flux, only the discrete-ordinates representations that would correspond to positive weights should be used. This means that the weights of each individual quadrature are first tested for positivity. If all the weights are found to be positive, for a given discrete-ordinates representation, its contribution is added to the total flux. The procedure

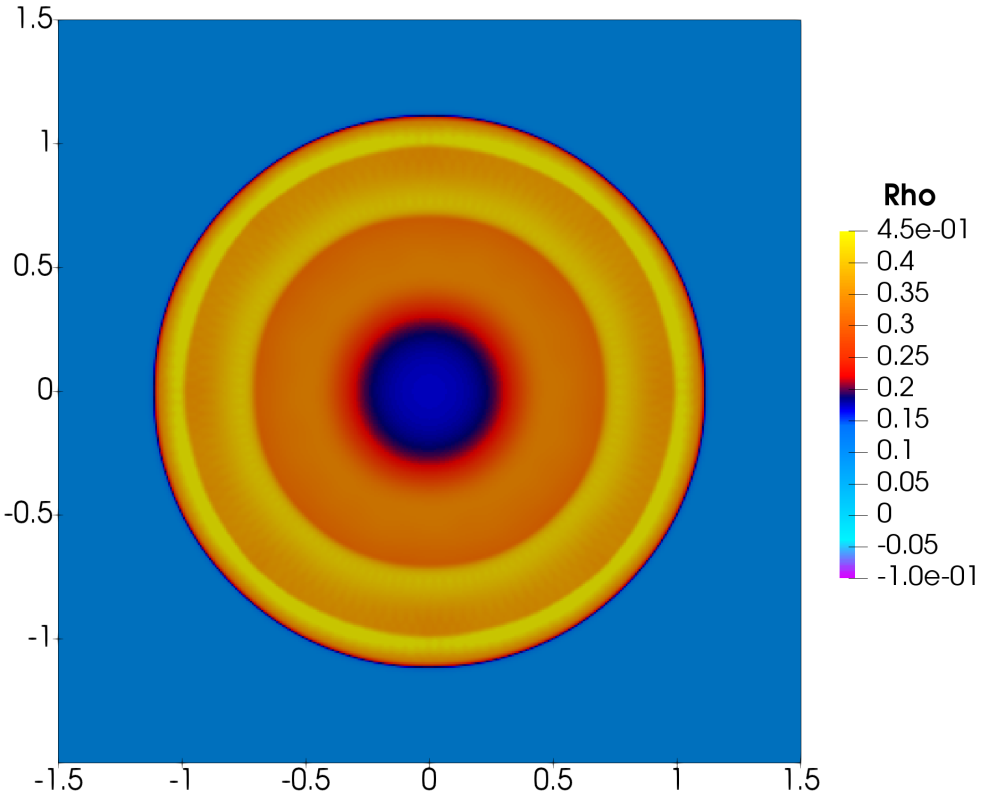

Figure 3.4: Radiation density, ρ, for the line source benchmark using the PAQ_1 closure with $\sigma_s = 1.0$

is described in more detail in the following Algorithm 1.

Algorithm 1 Flux Averaging Procedure

$\mathcal{Z} = 0$ ▷ Initializing counter
for $\xi \leftarrow 0$ to N **do** ▷ Loop over each quadrature

$\boldsymbol{W} = (\boldsymbol{Q}^{-1})^{(\xi)} \boldsymbol{U}$
if $\boldsymbol{W} >= 0$ **then**
$\boldsymbol{F}_i += \boldsymbol{Z}_i \, \boldsymbol{Q}^{-1}\boldsymbol{U}$
$\mathcal{Z}++$
end if
end for

$\boldsymbol{F}_i = \boldsymbol{F}_i / \mathcal{Z}$

The solution of the line source problem, using this method, is shown in Figure 3.4. Finally, the solution is rotationally invariant, preserve positivity and is far closer to the exact solution than all the other methods presented previously. However, due to the required positivity check, the solution is now a lot more ex-

pensive to compute since every time an inter-cell flux is needed, all the members of the quadrature collection are first checked for positivity before their specific contribution can be added to the total flux.

3.1.1 Binary Tree Structure

Now that a new model that produces positive and rotationally invariant solutions has been proposed, can the computational cost be reduced? In order to reduce the computational expense related to the positivity check of each discrete-ordinates representation, a binary-tree data structure is used. The goal of this data structure is to minimize the number of positivity checks and matrix multiplications required, without changing the overall calculation. The technique presented in this section is based on a special averaging procedure. In order to illustrate the method, the x-direction flux is considered. It has been found that it is always possible to average the fluxes of two neighboring quadrature representations and use this "equivalent flux" without changing the numerical solution. The procedure is mathematically described below. The X-directions fluxes of two neighbouring discrete-ordinates representations can be calculated according to Eq. (3.5) as,

$$\boldsymbol{F}_x^{(1)} = (\boldsymbol{Z}_x \boldsymbol{Q}^{-1})^{(1)} \boldsymbol{U} \,, \tag{3.8}$$

$$\boldsymbol{F}_x^{(2)} = (\boldsymbol{Z}_x \boldsymbol{Q}^{-1})^{(2)} \boldsymbol{U} \,. \tag{3.9}$$

It is now possible to calculate the equivalent average flux as,

$$\boldsymbol{F}_x^{(\text{equivalent})} = \frac{\left[\boldsymbol{F}_x^{(1)} + \boldsymbol{F}_x^{(2)}\right]}{2} \,, \tag{3.10}$$

$$\boldsymbol{F}_x^{(\text{equivalent})} = \frac{\left[(\boldsymbol{Z}_x \boldsymbol{Q}^{-1})^{(1)} \boldsymbol{U} + (\boldsymbol{Z}_x \boldsymbol{Q}^{-1})^{(2)} \boldsymbol{U}\right]}{2} \,, \tag{3.11}$$

$$\boldsymbol{F}_x^{(\text{equivalent})} = \frac{\left[(\boldsymbol{Z}_x \boldsymbol{Q}^{-1})^{(1)} + (\boldsymbol{Z}_x \boldsymbol{Q}^{-1})^{(2)}\right]}{2} \boldsymbol{U} \,. \tag{3.12}$$

One can rewrite this equation using an equivalent flux Jacobian,

$$\boldsymbol{F}_x^{(\text{equivalent})} = \left(\frac{\partial \boldsymbol{F_i}}{\partial \boldsymbol{U}}\right)^{(\text{equivalent})} \boldsymbol{U}\,, \tag{3.13}$$

$$\text{with} \qquad \left(\frac{\partial \boldsymbol{F_i}}{\partial \boldsymbol{U}}\right)^{(\text{equivalent})} = \frac{\left[(\boldsymbol{Z}_x\boldsymbol{Q}^{-1})^{(1)} + (\boldsymbol{Z}_x\boldsymbol{Q}^{-1})^{(2)}\right]}{2}\,.$$

For this particular case, the flux Jacobian is found to be diagonalizable. Thus it is possible to decompose it using a similarity transformation as,

$$\frac{\partial \boldsymbol{F_x}}{\partial \boldsymbol{U}}^{(\text{equivalent})} = \boldsymbol{R}\ \Omega_x\ \boldsymbol{R}^{-1}\,, \tag{3.14}$$

where $\boldsymbol{R}$ is the matrix of eigenvectors and Ω_x is the matrix with the corresponding eigenvalues. As shown in Eq. (3.15), one can see that the matrix $\boldsymbol{R}$ is in fact of the structure as the matrix $\boldsymbol{Q}$ and that the term $\boldsymbol{R}\ \Omega_x$ is equal to the matrix $\boldsymbol{Z_x}$,

$$\boldsymbol{R}\ \Omega_x\ \boldsymbol{R}^{-1} = \boldsymbol{Z}_x\boldsymbol{Q}^{-1} \tag{3.15}$$

$$\text{where,} \qquad \boldsymbol{R}\,\Omega_x = \boldsymbol{Z}_i \quad \text{and} \quad \boldsymbol{R}^{-1} = \boldsymbol{Q}^{-1}\,.$$

It is therefore possible to interpret, $\boldsymbol{R}$, as representing an "equivalent" quadrature rule. Using this transformation, every time an equivalent flux is calculated, it is possible to find the matrix $\boldsymbol{Q}$, representing the equivalent quadrature representation for a specific direction. This matrix is needed for the positivity check shown in Algorithm 1. This averaging procedure is represented graphically in Figure 3.5, where the two initial quadrature representation are shown in blue and the equivalent quadrature representation is shown in orange.

One can see that this averaged quadrature will not always produce the same flux as if the two initial quadratures were used for a specific state $\boldsymbol{U}$. As an example, let us consider the case presented in Figure 3.6, where the state $\boldsymbol{U}$ is represented by the red arrow. Again the state, $\boldsymbol{U}$ is projected on the 2D velocity space and the 0^{th}-order moment is taken to be $U_0 = 1$. In that situation, neither

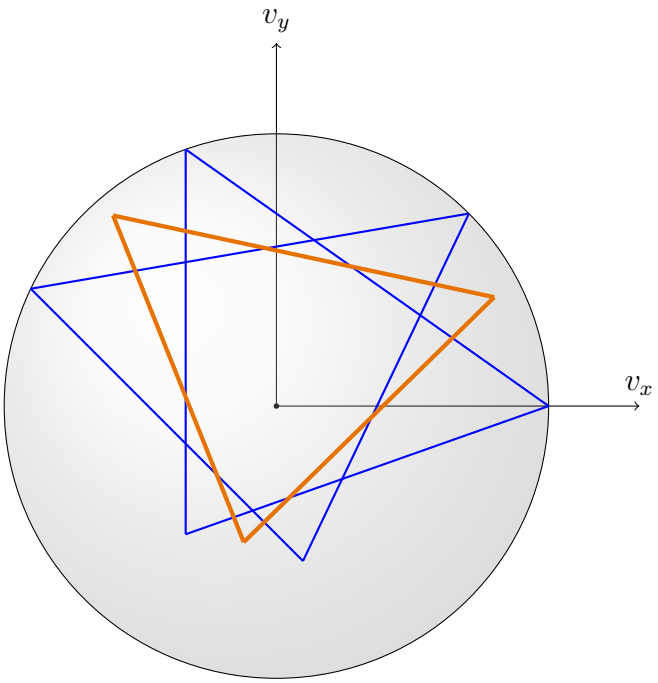

Figure 3.5: Graphical representation of the X-direction equivalent $\boldsymbol{Q}$ matrix calculation

of the two initial quadratures contribution would be added to the total x-direction flux calculation. However, in this case the averaged quadrature would give positive weights thus its contribution would be added to the flux calculation. Even if the solution is still guaranteed to maintain positivity, this artifact will produce solutions that are not rotationally invariant and will depend on which quadratures are averaged.

Using this averaging procedure, one can now build the binary tree data structure. In order to illustrate the method, a small collection composed of eight discrete-ordinates representations is considered, as shown in Figure 3.7. The collection of discrete-ordinates representations, shown in Figure 3.7a, are first ordered based on their rotation angle. Then, the collection of discrete-ordinates representations are grouped into groups of two and the equivalent fluxes are calculated, as represented in Figure 3.7b. It is important to note that, for obvious reason, in order for this technique to work, one must choose, N, the number quadrature representation, to be a power of two. As shown in Figures 3.7c and 3.7d, the procedure is repeated until a single equivalent quadrature is found at the top of

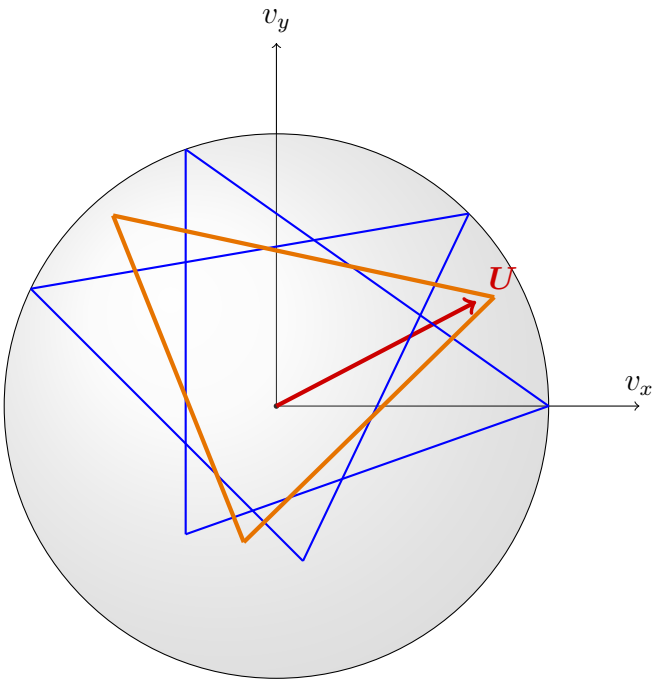

Figure 3.6: Graphical representation of the averaging procedure for a state $\boldsymbol{U}$

the tree.

Once the binary tree is built, let us consider a simple case to illustrate how it would be used in a real flux calculation. For example, the following case will be considered where, for a given state $\boldsymbol{U}$, the positivity of the bottom-row quadratures is distributed as shown in Figure 3.8. In this oversimplified example, three of the eight bottom-row quadratures are found to be negative, thus their contribution should not be added to the total flux calculation. The algorithm used in this work first checks the top equivalent quadrature for positivity using Eq. (3.3). If one of the weights is found to be negative, the algorithm jumps to the second level of the tree. This procedure is repeated until all positive equivalent quadratures are identified. As shown in Figure 3.9, the flux is calculated using only three matrix multiplications. One can see that flux contribution of the right part of the tree is obtained using only one matrix even though a negative quadrature representation is present. This behaviours was explained above using Figure 3.6. The hope is that throughout a real calculation, the fluxes will mostly be calculated using the higher levels of the tree and only in extreme cases the bottom-row will be needed thus greatly limiting the computational expenses.

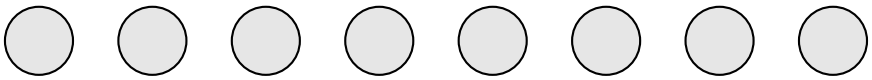

(a) Initial discrete-ordinates collection

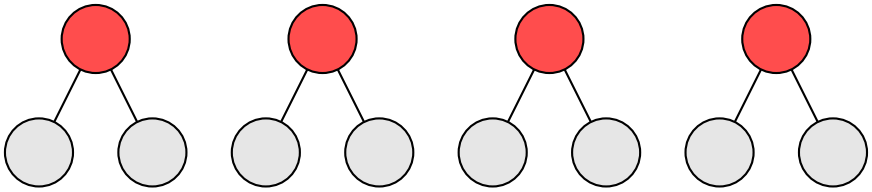

(b) First row of the binary tree

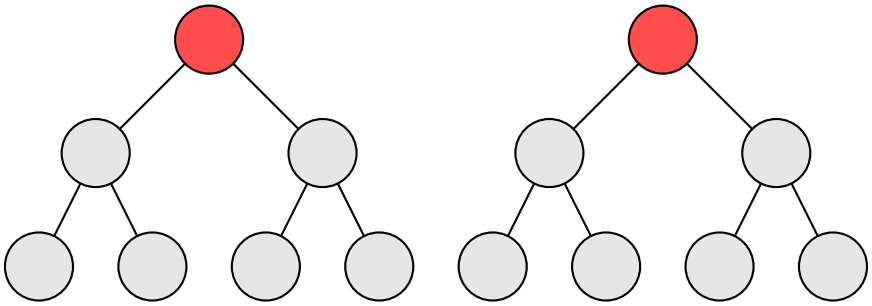

(c) Second row of the binary tree

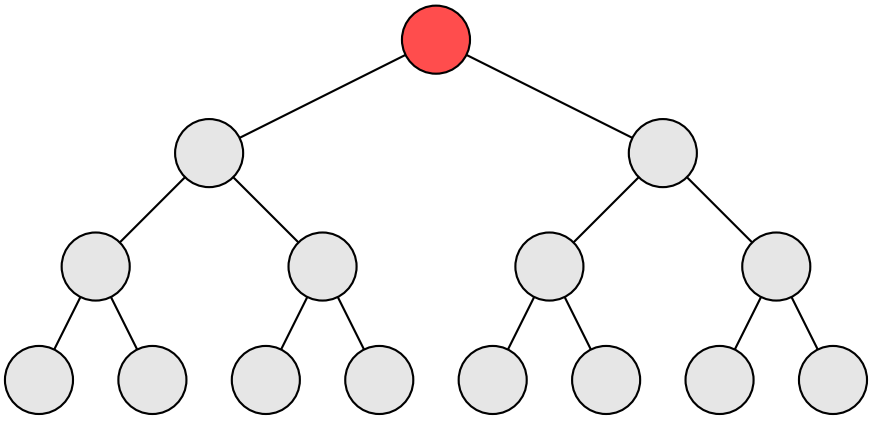

(d) Top row of the binary tree

Figure 3.7: Graphical representation of the binary tree-data structure

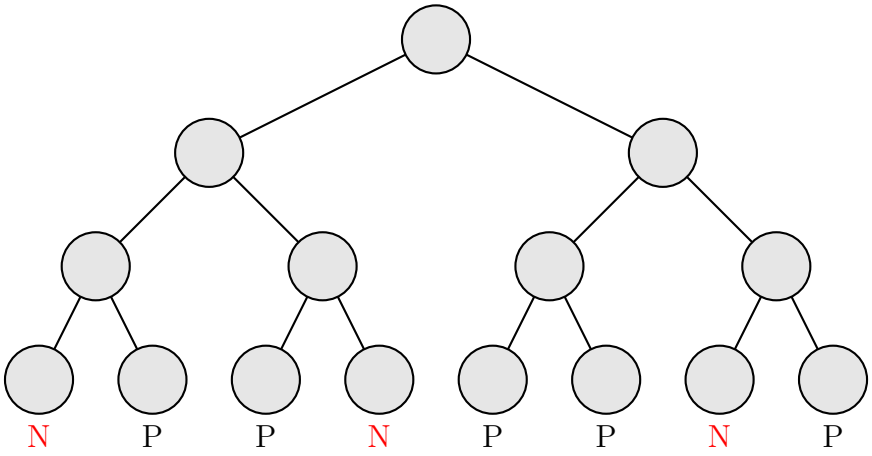

Figure 3.8: Graphical representation of a flux calculation uisng the binary-tree data structure

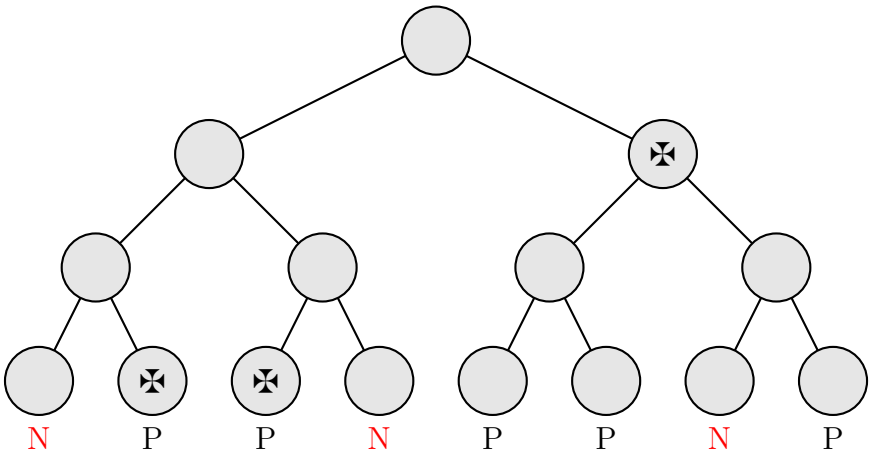

Figure 3.9: Graphical representation of a flux calculation uisng the binary-tree data structure

3.1.2 The Closing Fluxes

In the end, the behaviour of the models depends entirely on the PDEs that they produce. Specifically, it is the relationship between the closing fluxes and the known moments of the solution vector that is important. In this section the relationship between the closing entries of the x-direction flux and the solution vector is examined for the four first-order models presented so far. In a two-dimensional Cartesian coordinate system, the moment equations take the form,

$$\frac{\partial \boldsymbol{U}}{\partial t} + \frac{\partial \boldsymbol{F_x}}{\partial x} + \frac{\partial \boldsymbol{F_y}}{\partial y} = \boldsymbol{S}\,. \tag{3.16}$$

This equation can be rewritten in matrix-vector form as,

$$\frac{\partial}{\partial t}\begin{bmatrix} \rho \\ \rho u_x \\ \rho u_y \end{bmatrix} + \frac{\partial}{\partial x}\begin{bmatrix} \rho u_x \\ U_{xx} \\ U_{xy} \end{bmatrix} + \frac{\partial}{\partial y}\begin{bmatrix} \rho u_y \\ U_{yx} \\ U_{yy} \end{bmatrix} = \boldsymbol{S}\,, \tag{3.17}$$

where

$$\boldsymbol{S} = \begin{bmatrix} \rho(\sigma_e - \sigma_a) \\ -(\sigma_s + \sigma_a)\rho u_x \\ -(\sigma_s + \sigma_a)\rho u_y \end{bmatrix} \tag{3.18}$$

is the source term representing scattering, emission and absorption. It is important to note that the closing fluxes, present in the flux vector, $\boldsymbol{F_x}$, but not the solution vector, $\boldsymbol{U}$, are U_{xx} and U_{xy}.

Figures 3.10 shows how the unknown entry, U_{xx}, in the x-direction flux vector, of the four studied models, vary as a function of the x-component of the velocity, u_x, for a particle density $\rho = 1.0$ and a Y-component velocity, $u_y = 0.0$. In physical reality, if $u_x = 1.0$, the flux U_{xx} has to be 1.0. Since particles cannot travel faster then the speed of light, the x-direction bulk velocity u_x reaches 1.0

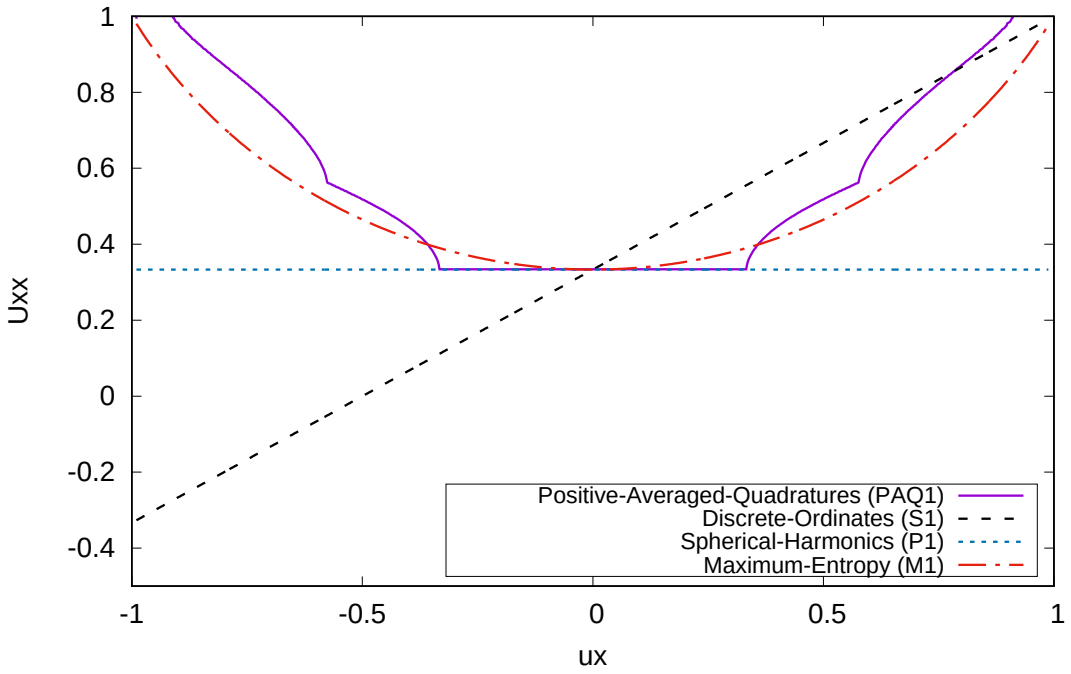

Figure 3.10: U_{xx} as a function of the velocity u_x with $u_y = 0$

only if all particles are moving straight in the X-direction, thus the variance of the particle velocities is zero. Figure 3.10 shows that the M_1 model recovers perfectly that behavior, while the PAQ_1 model approach the right limits. The spherical-harmonic model predicts a constant value while the discrete-ordinates show a negative value of the flux for u_x below -0.5. Again, this is physically impossible. It is also interesting to note that for small values of u_x the PAQ_1 model recovers the exact same solution as the P_1 closure. The kinks observed in the PAQ_1 solution are caused by an abrupt change in the number of discrete-ordinates used in the flux calculation. For a value of $|u|$ smaller than $1/3$ all quadrature representations are used, therefore leading to the spherical harmonic solution. The second kink happens for values of $|u|$ larger than $1/\sqrt{3}$ where again the number of quadratures used drops drastically. This behavior can is explained in more detail using a graphical representation of the 2D velocity space. Figure 3.11 shows the two critical bulk velocities, $u_1 = 1/3$ and $u_2 = 1\sqrt{3}$. One can see that for a given state, $\boldsymbol{U}$, if the bulk velocity is smaller than u_1, shown in

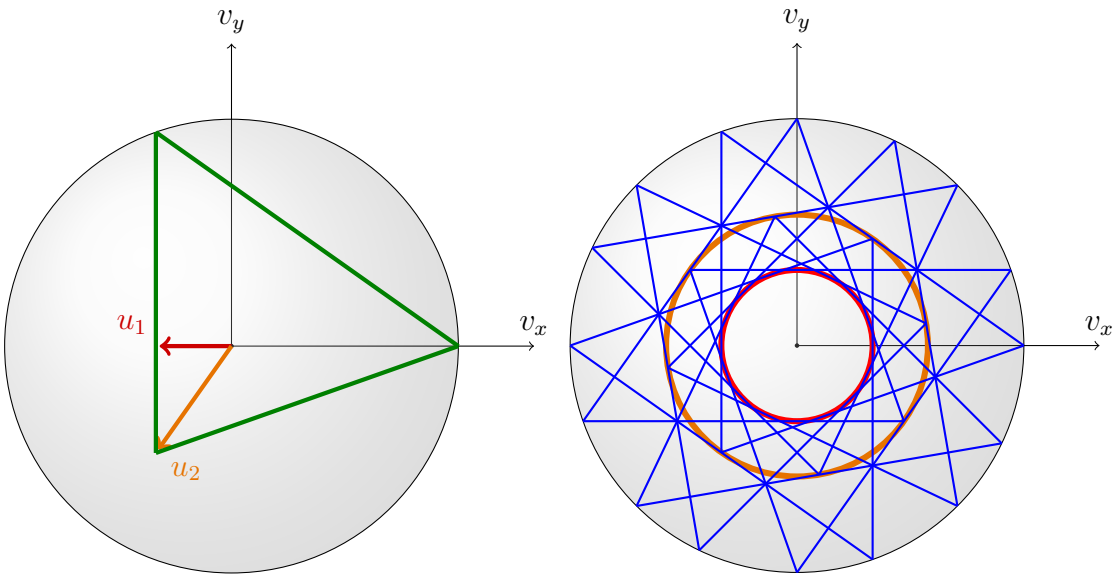

(a) One discrete-ordinate representation (b) Eight discrete-ordinate representations

Figure 3.11: Graphical representation of the bulk velocity, u, for discrete-ordinates representations on a 2D velocity space

red, all quadrature representations are used for the flux calculation. However if the bulk velocity is larger than u_2, shown in orange, only a few discrete-ordinates representations correspond to positive weights. The unknown entry, U_{xy} is not shown here since it remains at a constant value of $U_{xy} = 0$ for $u_y = 0$.

In Figure 3.12 and 3.13, the y-direction velocity u_y is set to 0.5. One can observe similar behaviours for U_{xx}. The PAQ_1 model approach the right limits, but does not quite reach the same extrema as the M_1 closure. The M_1 and PAQ_1 closures are the only ones to correctly predict a variation in U_{xy}. Again, such variation is expected in the real physics of radiative transfer.

3.1.3 Eigenstructure of the PAQ_1 closure

In this section the eigenstructures of the four studied first-order closures are presented. The moment equation (3.16) can be simplified in order to approximate local properties. Let's consider the following one-dimensional, source-free moment equation,

$$\frac{\partial \boldsymbol{U}}{\partial t} + \frac{\partial \boldsymbol{F_x}}{\partial x} = 0\,. \tag{3.19}$$

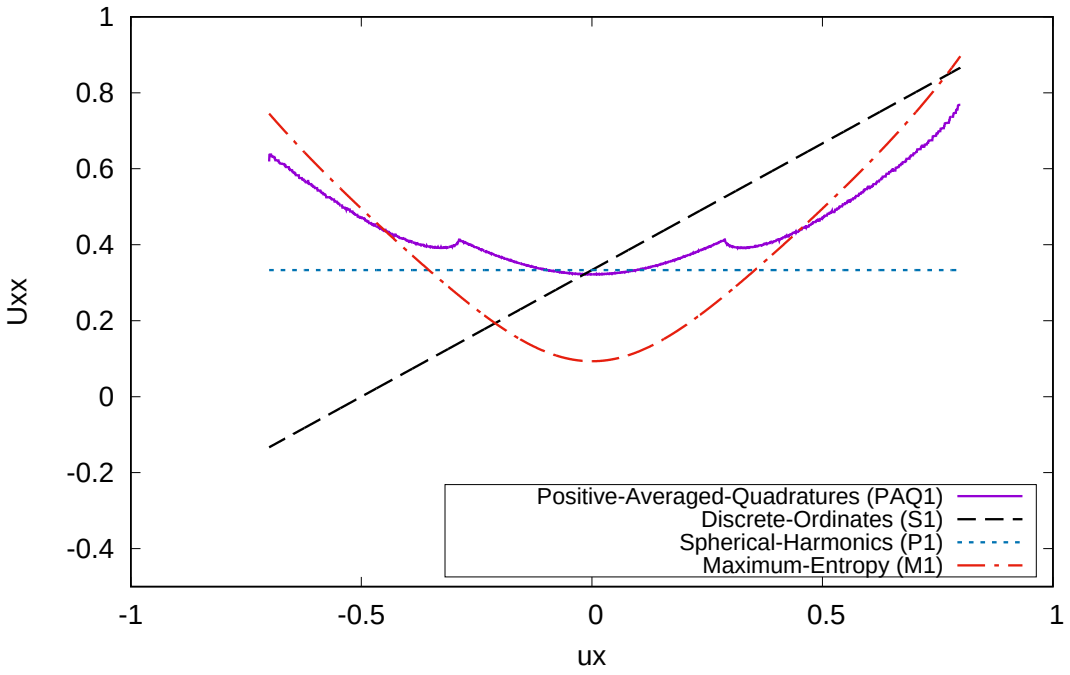

Figure 3.12: U_{xx} as a function of the velocity u_x with $u_y = 0.5$

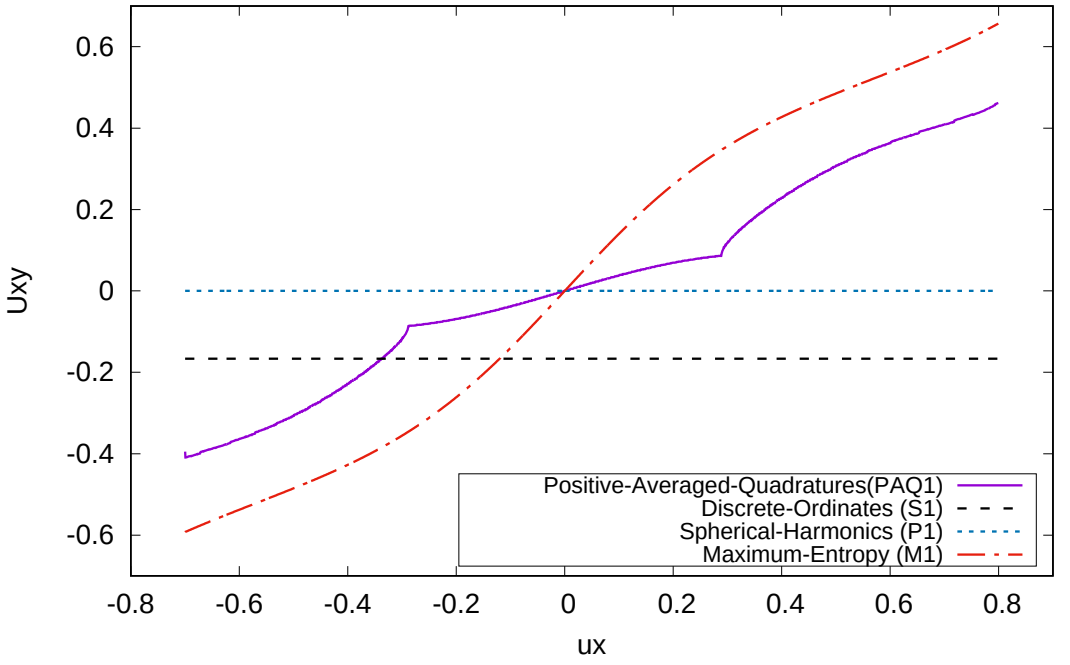

Figure 3.13: U_{xy} as a function of the velocity u_x with $u_y = 0.5$

This equation can be rewritten in the following form,

$$\frac{\partial \boldsymbol{U}}{\partial t} + \left(\frac{\partial \boldsymbol{F_x}}{\partial \boldsymbol{U}}\right)\frac{\partial \boldsymbol{U}}{\partial x} = 0\,, \tag{3.20}$$

where the matrix $\left(\frac{\partial \boldsymbol{F_x}}{\partial \boldsymbol{U}}\right)$ is the flux Jacobian. The Eigenvalues of that matrix represent the propagating wave speeds for a given state $\boldsymbol{U}$. For the P_1 closure, the flux Jacobian matrix is in fact very simple. As seen from Eq. (2.42), the flux Jacobain is not even a function of the known moments, thus it remains constant,

$$\frac{\partial \boldsymbol{F_x}}{\partial \boldsymbol{U}} = \begin{bmatrix} 1 & 0 & 0 \\ 0 & \frac{1}{3} & 0 \\ 0 & 0 & 0 \end{bmatrix}. \tag{3.21}$$

The S_1 closure flux Jacobian is also very straightforward. For a given set of quadrature points, the matrix is simply defined as,

$$\frac{\partial \boldsymbol{F_x}}{\partial \boldsymbol{U}} = Z_x Q^{-1} \tag{3.22}$$

where the matrices $\boldsymbol{Z}_x$ and $\boldsymbol{Q}$ are defined in Eqns. (2.52) and (2.49) respectively. On the other hand, the eigenstructure of the M_1 closure is much more elaborate. As derived by Berthon *et al.* [1], the X-direction flux Jacobian is known to be,

$$\frac{\partial \boldsymbol{F_x}}{\partial \boldsymbol{U}} = \begin{bmatrix} 0 & 1 & 0 \\ c^2\frac{(2u^2-3u_y^2)(\chi-u\chi')+u_y^2}{2u^2} & c\left(\frac{u_x\chi'}{u} - \frac{u_x u_y^2}{2u^4}\Theta\right) & c\left(-\frac{u_y\chi'}{2u} + \frac{u_x^2 u_y}{2u^4}\Theta\right) \\ c^2\frac{u_x u_y}{2u^2}(3\chi - 3u\chi - 1) & c\left(\frac{u_y(3\chi-1)}{2u^2} + \frac{u_x^2 u_y}{2u^4}\Theta\right) & c\left(\frac{u_x(3\chi-1)}{2u^2} + \frac{u_y^2 u_x}{2u^4}\Theta\right) \end{bmatrix},$$

where the variable $\Theta = 2c\rho - 6c\rho\chi + 3u\chi'$ and $\chi' = \frac{2u}{\xi}$. It is also important to note that the scalar, u, is simply defined as,

$$u = \sqrt{u_x^2 + u_y^2}\,.$$

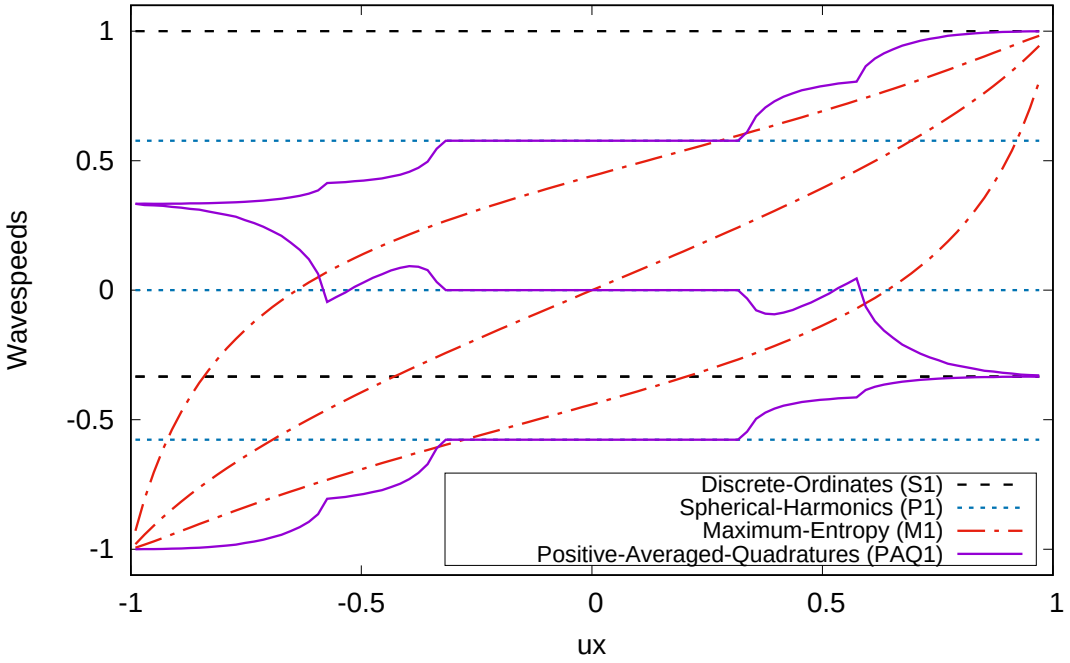

Figure 3.14: Eigenvalues as a function of the velocity u_x with $u_y = 0.0$

The corresponding eigenvalues, again obtained by obtained Berthon *et al.* [1], are,

$$\lambda_{x,1,2} = c\left(\frac{u_x}{\xi} \pm \frac{\sqrt{2(\xi-1)(\xi+2)(2(\xi-1)(\xi+2)+3u_y^2)}}{\sqrt{3}\xi(\xi+2)}\right) \tag{3.23}$$

$$\lambda_{x,3} = c\frac{u_x(2-\xi)}{u^2} \tag{3.24}$$

Finally, the flux Jacobian of the PAQ_1 closure, based on Eq. 3.6, is,

$$\frac{\partial \boldsymbol{F_x}}{\partial \boldsymbol{U}} = \frac{1}{N}\sum_{\xi=0}^{N}\left(Z_i Q^{-1}\right)^{(\xi)}\boldsymbol{U}\,. \tag{3.25}$$

Where the sum on ξ only includes quadrature representations that lead to positive weights. One can see that this matrix is not constant. The Jacobian is constructed by averaging the contribution of each discrete-ordinates representation that correspond to positive quadrature weights, thus is will vary based on the given state $\boldsymbol{U}$. Figure 3.14 shows the wave speeds of the four models for a particle density $\rho = 1$ and constant $u_y = 0.0$. As expected, the wave speeds for both the P_1 and

the S_1 remain constant. The three wave speeds of the P_1 closure are $\pm\sqrt{(1/3)}$ and 0.0 while for the S_1 closure two wave speeds are positioned at $-1/3$ and the third one is at 1.0. These are in fact the x-coordinates of the chosen quadrature points. The M_1 closure displays a more physical behavior, all three wave speeds reach the right limits of $\pm c$, while transitioning smoothly throughout the domain. The wave speeds observed for the PAQ_1 closure are interesting. At least one recovers the right limits and as observed for the closing fluxes, for a value of $|u_x|$ bellow $1/3$ the model recovers exactly the wave speeds of the P_1 closure. One can also see that for $|u_x| = 1.0$, one of the PAQ_1 wave also recovers the S_1 wave speeds. This is due to the fact that, when $|u_x| = 1.0$, the flux is computed using only one discrete-ordinates representation. The kinks observes at $|u_x| = 1/3$ and $|u_x| = 1/\sqrt{3}$ are due to the specific geometry of initial quadrature representation and have been explained in the previous section.

Chapter 4

Numerical Results

In this chapter, numerical simulations are presented in order to investigate the general behavior of the proposed model compared to the other first-order models presented in Chapter 2. The developed code uses a Godunov-type finite-volume method to compute the various solutions. Over the past decades, Godunov-type finite-volume methods have been widely adopted as the dominant computational approach for solving systems of hyperbolic balance laws [17, 18, 19]. In this chapter, solutions of the line-source benchmark for various level of background scattering along with a grid dependence study are shown. Two other standard problems for radiative transport, the hohlraum problem and the lattice problem, are also presented [3].

In order to compute the solution for any given problem, the code used to calculate the fluxes of the different models is coupled to an in-house flow solver. All simulation results are presented on 2D plots. For each case considered, the corresponding plot is formed by a 2D structured Cartesian grid of variable dimension and mesh resolution. It is important to note that none of these first-order closures are expected to produce accurate numerical solutions to any of the three standard problems. The goal of the study presented in this chapter is, rather to asses the different behaviours of each model and identify any important modelling artifacts

such as rotational asymmetry of negativity or the particle density.

4.0.1 Numerical Method

In finite-volume methods, the domain is first discretized into non-overlapping volumes. These volumes are delimited by nodes forming the mesh. The studied partial differential equation (balance law) is then expressed in its so-called integral form. This is done by converting the divergence terms into surface integrals through the divergence theorem. For example, if one considers the following general balance law,

$$\frac{\partial U}{\partial t} + \nabla \cdot F(U) = S\,, \tag{4.1}$$

where U represents a state vector, $F(U)$ represents the corresponding flux tensor and S the local source vector. Since the spacial domain is subdivided into finite volumes, the volume integral needs to be taken over each cell. This yields,

$$\iiint_{V_i} \frac{\partial U}{\partial t} \mathrm{d}V + \iiint_{V_i} \nabla F(U) \mathrm{d}V = \iiint_{V_i} S \,\mathrm{d}V\,. \tag{4.2}$$

where, V_i, is the volume of the i^{th} cell. By applying the divergence theorem, it is possible to rewrite the balance law as,

$$\iiint_{V_i} \frac{\partial U}{\partial t} \mathrm{d}V + \oiint_{s_i} F(U) \cdot \hat{n} \,\mathrm{d}s = \iiint_{V_i} S \,\mathrm{d}V\,, \tag{4.3}$$

where $\hat{n}$ is the outward-facing unit normal to the surface and s_i is the surface of the i^{th} cell. By integrating the first term, the average density, $\bar{U}_i$ can be found as,

$$\bar{U}_i = \frac{1}{V_i} \iiint_{Vi} U_i \mathrm{d}V\,. \tag{4.4}$$

By assuming that each volume V_i is constant in time and is bounded by a finite number of faces, the balance law can then be written as

$$\frac{\partial \bar{U}_i}{\partial t} + \frac{1}{V_i} \sum_{j=0}^{\#faces} F_j \cdot \hat{n_j} \, S_j \, = \frac{1}{V_i} \iiint_{V_i} S \, \mathrm{d}V \, . \tag{4.5}$$

The rate of change of the average density, $\bar{U}_i$, of each cell is evaluated by adding the fluxes at the boundaries and the net effect of any source term. Because the flux entering a given volume is identical to that leaving the adjacent volume, the finite volume method is conservative if no source is present. The solution representation is generally discontinuous on the cell boundaries. Numerical flux functions must be used to estimate the flux at such discontinuities.

The flux function implemented in the current code is a two-state HLL Riemann solver [18]. This function is used to calculate the flux crossing each boundary of the grid at each time step. In the code, the flux function is implemented as,

$$F_{HLL} \, = \, \frac{\lambda^+ F(\bar{U_L}) \, - \lambda^- F(\bar{U_R})}{\lambda^+ - \lambda^-} \, + \, \frac{\lambda^+ \lambda^-}{\lambda^+ - \lambda^-} (\bar{U_R} - \bar{U_L}) \, , \tag{4.6}$$

where λ^+ and λ^- are the fastest positive and negative wave speeds from the states $\bar{U_R}$ and $\bar{U_L}$ respectively. In order to reduce the numerical cost associated with finding the eigenvalues at each flux calculation, the only wave speeds used are bounded by the speed of light. The fastest positive and negative wave speeds are simply taken as c and $-c$. Substituting those values in the two-state HLL flux function yields,

$$F_{HLL} \, = \, \frac{F(\bar{U_L}) \, + F(\bar{U_R})}{2} \, + \, \frac{c}{2} (\bar{u_R} - \bar{u_L}) \, . \tag{4.7}$$

This is also known as the local Lax-Friedrichs flux function, where c is the maximum absolute value of any wave speed of the system. Finally, the time-marching

method implemented in the code is the explicit Euler method,

$$U_i^{n+1} = U_i^n + \Delta t \left(\frac{\mathrm{d}U}{\mathrm{d}t} \right)^n , \tag{4.8}$$

where Δt is calculated to be the minimum cell length over the maximum wave speed value time the CFL number. To ensure stability, a CFL number of 0.5 is used.

4.1 The Line Source Problem

In this section, a grid dependence study is first conducted in order to assess the mesh resolution required to produce accurate solutions. Then, numerical solutions of the line source problem are presented for each model using various levels of scattering. The computation time of each simulation has been recorded in order to compare the efficiency of the different models.

The line source problem has already been previously presented in Chapter 2. As a reminder, the line source problem is described as an initial pulse of particles that are initially distributed isotropically along an infinite line in space and which then move through a medium with a constant scattering. For numerical simulations, the initial pulse of radiation is approximated by a steep Gaussian. The initial condition used for all simulations is as follows,

$$\mathcal{F} = \max \left(\frac{1}{2\pi\omega^2} e^{-(x^2+y^2)/(\omega^2)}, 10^{-3} \right) , \tag{4.9}$$

where the factor $\omega = 0.03$ is constant for all simulations. All cases are run to a final time, $t_{\text{final}} = 1.0$, using a grid of 400 by 400 cells unless specified otherwise. All boundary conditions are set to be a zero-gradient condition. A more complete description of the line source problem is presented in Section 2.3. All simulations using the PAQ_1 closure were run using a family of 1024 distinct discrete-ordinates

representations which correspond to a structure binary tree of 10 levels. This number was chosen in order to best balance the accuracy and computational expense of the model.

4.1.1 Mesh Dependence Study

In order to determine the mesh resolution required for accurate solution, the line source problem with a scattering constant of $\sigma_s = 2.0$ has been run four times on different grids using the first-order of the new model without using the binary-tree structure. For all simulations, the CFL number was set to 0.5. The results are presented at time $t_{\text{final}} = 1.0$.

Figure 4.1 shows that the solution does not change significantly for a mesh resolution higher then 200 by 200 cells. However, for safety, all the cases presented in this section have been simulated on a 400 by 400 Cartesian grid. This mesh resolution is preferred since it produces accurate solutions without being overly computationally expensive.

4.1.2 Line Source Solutions for Various Scattering levels

The line source benchmark is solved using increasing levels of scattering. As seen in Eq. (2.23), scattering basically absorbs incoming radiation and re-emits it according to the statistics given by the equilibrium state. The more the background scattering increases, the easier the problem becomes to solve numerically. In other words, scattering limits the value of the bulk velocity, u_i, by redirecting photons in arbitrary directions. The goal of this study is, first, to gain knowledge on the behavior of each model but also to see which model converges faster to the exact solution.

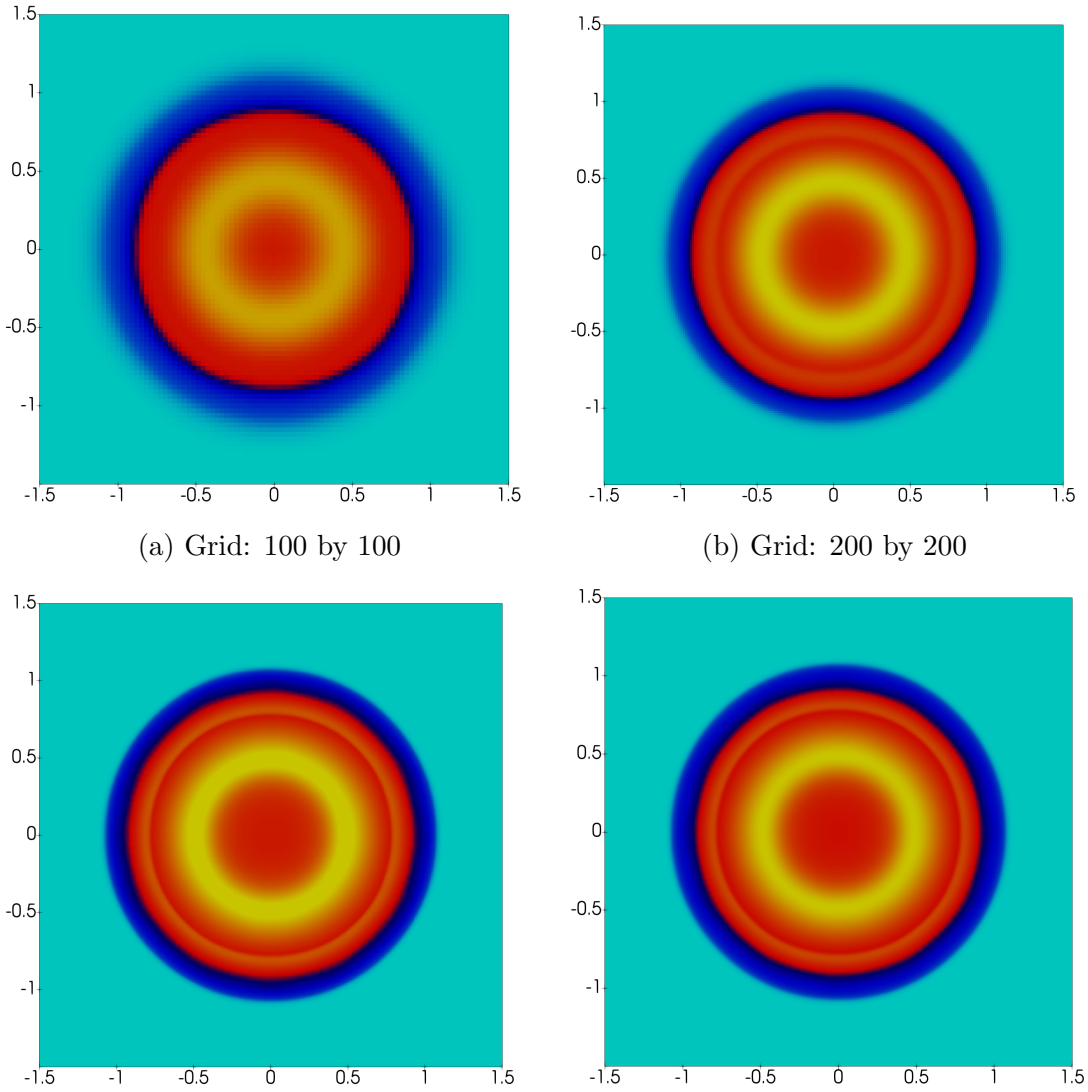

(a) Grid: 100 by 100

(b) Grid: 200 by 200

(c) Grid: 400 by 400

(d) Grid: 800 by 800

Figure 4.1: Radiation density, ρ, for the line source benchmark using the PAQ_1 model for multiple mesh resolutions

Figure 4.2 shows the radiation density, ρ, predicted using a scattering intensity of $\sigma_s = 1.0$. As discussed earlier, both the M_1 and the PAQ_1 solutions are symmetric, maintain positivity and recover the correct radiation speed. However, the M_1 closure predicts a large region of high radiation intensity at the outer edge while under-predicting the radiation density at the center. The P_1 closure is rotationally invariant but does not preserve positivity and underpredicts the radiation speed. The region of negative particle density is shown in pink. The S_1 closure, using only four directions, is simply too crude to produce an accurate prediction. As mentioned before, a large number of discrete directions are needed for the discrete-ordinates models to be accurate. Finally, the solution produced using the PAQ_1 closure with the structured binary tree maintain positivity but is far from being rotationally invariant. This is due to the order in which quadratures are grouped in the binary tree, as explained in Section 3.1.1. By comparing the results with the exact solution, one can see that the PAQ_1 closure without the tree, produces the best approximation.

Figure 4.3, shows the radiation density, ρ, for a scattering intensity of $\sigma_s = 2.0$. All other initial conditions remain unchanged. As expected, increasing the background scattering makes the problem easier to solve numerically. Now both the M_1 and the PAQ_1 solutions are predicting an higher radiation density at the center and agree with the exact solution relatively well. The P_1 closure still predicts a zone of negative radiation density (in pink) which is physically impossible. The solution produced using the PAQ_1 closure with the structured binary tree, although improving, is still far from being rotationally invariant.

Figures 4.4 and 4.5 shows the radiation density, ρ, for a scattering intensity of $\sigma_s = 4.0$ and $\sigma_s = 6.0$ respectively. In Figure 4.4, the solution produced by the M_1 and the PAQ_1 are now very close to the exact solution. The P_1 closure does not produce negative particle density anymore, but still does not accurately predict

Table 4.1: Comparison of the first-order closures computation times when solving the line-source benchmark for various levels of scattering

σ_s	M_1	P_1	S_1	PAQ_1	PAQ_1 (tree)
1.0	94 s	45 s	46 s	247 s	139 s
2.0	90 s	46 s	48 s	243 s	129 s
4.0	93 s	40 s	45 s	226 s	51 s
6.0	96 s	46 s	42 s	223 s	47 s
8	94 s	44 s	49 s	217 s	46 s

the radiation distribution. The solution produced using the PAQ_1 closure with the tree, is almost rotationally invariant at this point and recovers the solution found using the PAQ_1 closure almost perfectly. Finally, in Figure 4.5, all solutions, with the exception of the S_1 solution, are almost identical and accurately predict the behavior of radiation. Solutions using higher level of scattering have been run but do not show any more relevant information. Based on this study, the PAQ_1 closure seams to produce the best approximation to the line source problem, followed closely by the M_1 closure. It produces rotationally invariant, positive solutions that are in closest agreement with the exact solution.

Although the solutions produced using the PAQ_1 closure with the structured binary tree maintain positivity, the asymmetry observed is due to the fact that, each time a flux is calculated, the algorithm used to navigate the tree often includes initial quadrature representations that would lead negative weights if used on their own. This behavior is explained in Section 3.1.1.

Computation Time

The computation time of all simulations shown above has been recorded and are presented here. All simulation were run using one core on the same CPU to ensure accurate and consistent results. The CPU used was an Intel i7-6700HQ. Table 4.1 shows the computation time of all the above cases.

As expected, the computation times of all but the PAQ_1 closure using the tree do not vary as a function of the scattering intensity. The results show that

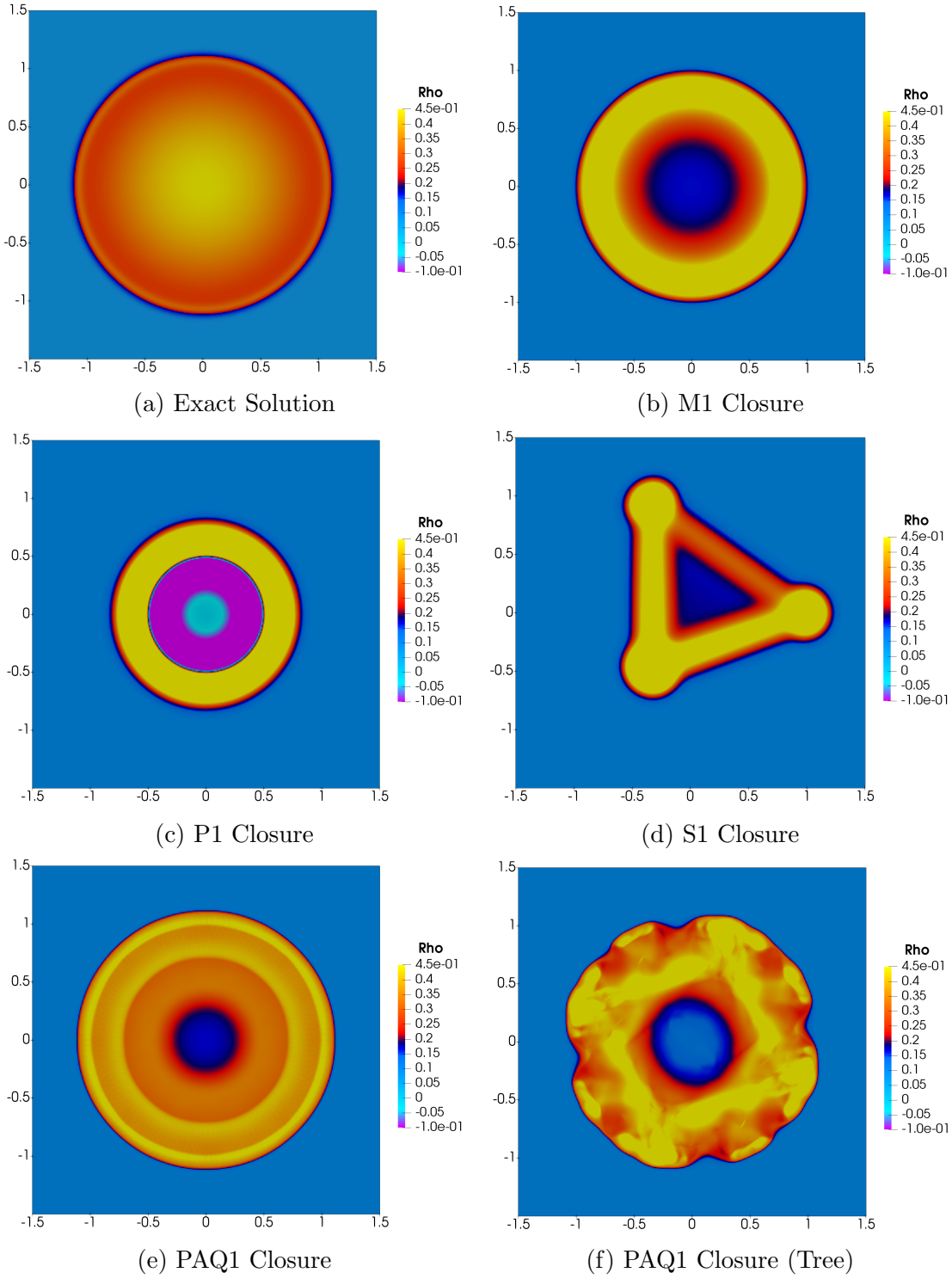

(a) Exact Solution

(b) M1 Closure

(c) P1 Closure

(d) S1 Closure

(e) PAQ1 Closure

(f) PAQ1 Closure (Tree)

Figure 4.2: Radiation density, ρ, for the line source benchmark using a scattering constant $\sigma_s = 1.0$ at $t = 1.0$

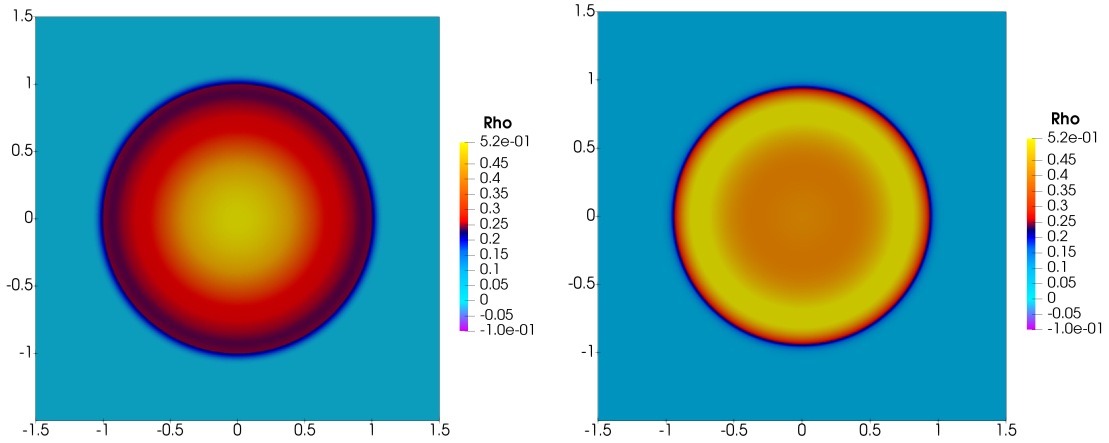

(a) Exact Solution

(b) M1 Closure

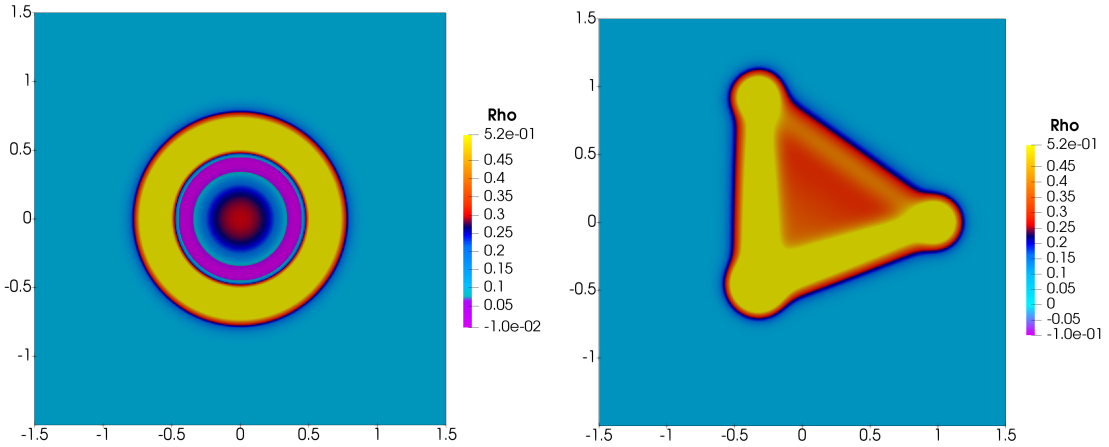

(c) P1 Closure

(d) S1 Closure

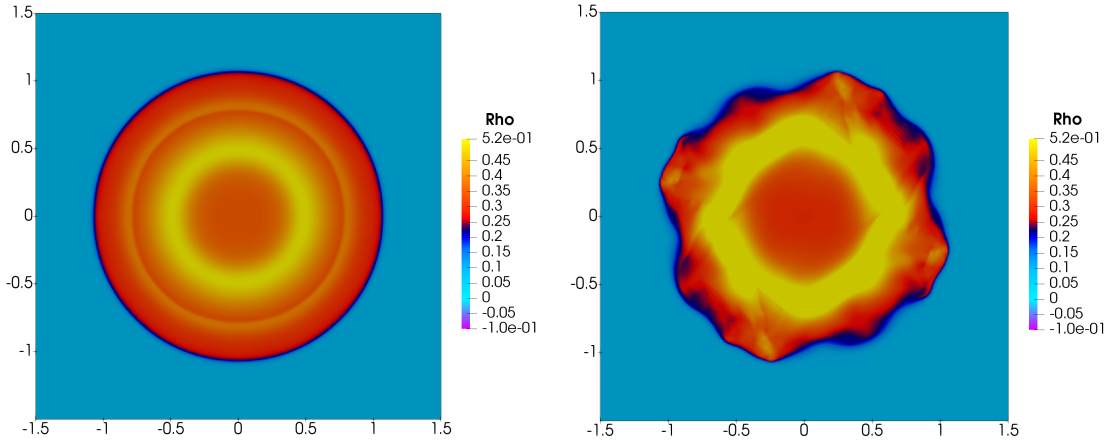

(e) PAQ1 Closure

(f) PAQ1 Closure (Tree)

Figure 4.3: Radiation density, ρ, for the line source benchmark using a scattering constant $\sigma_s = 2.0$ at $t = 1.0$

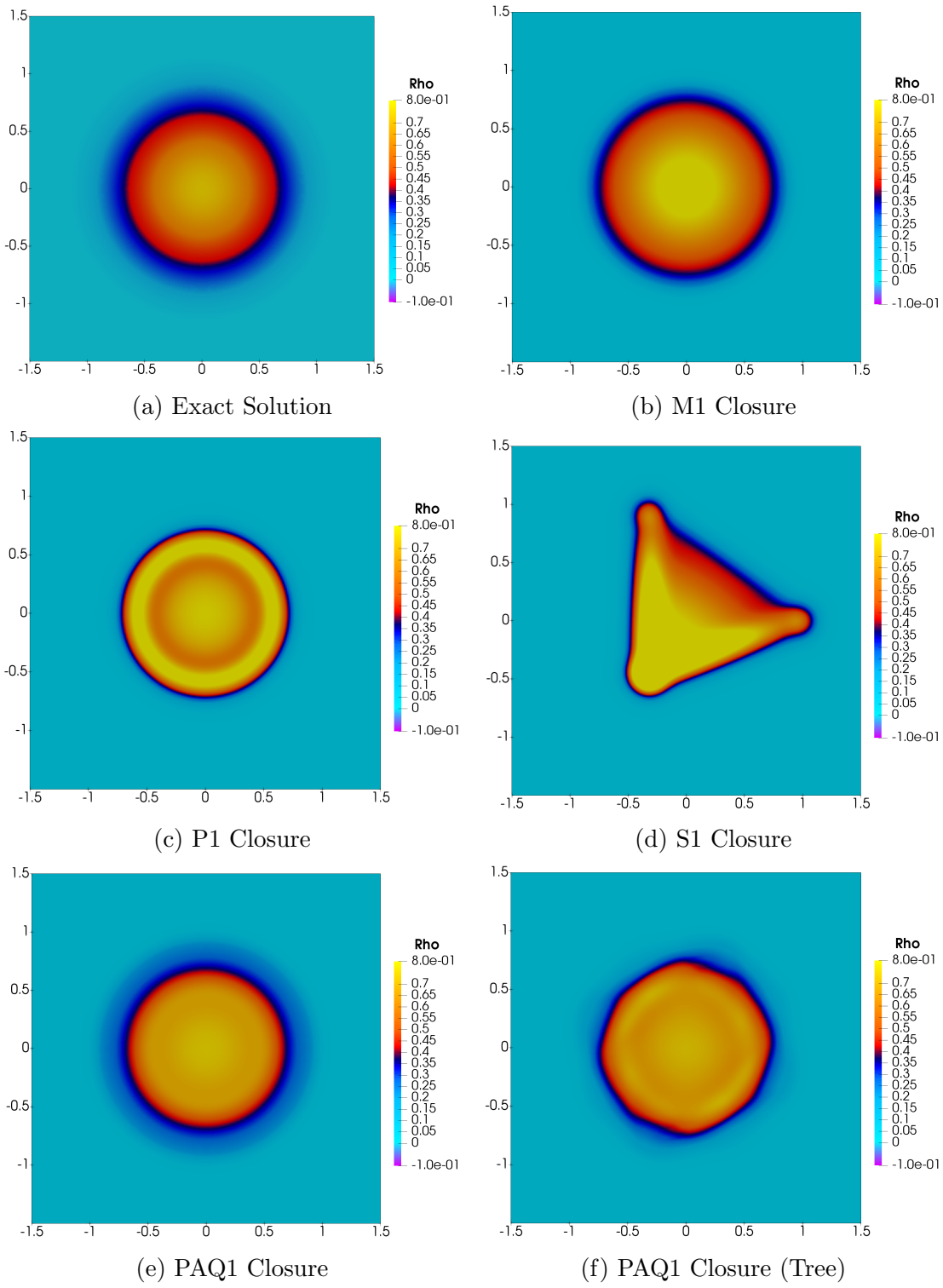

(a) Exact Solution

(b) M1 Closure

(c) P1 Closure

(d) S1 Closure

(e) PAQ1 Closure

(f) PAQ1 Closure (Tree)

Figure 4.4: Radiation density, ρ, for the line source benchmark using a scattering constant $\sigma_s = 4.0$ at $t = 1.0$

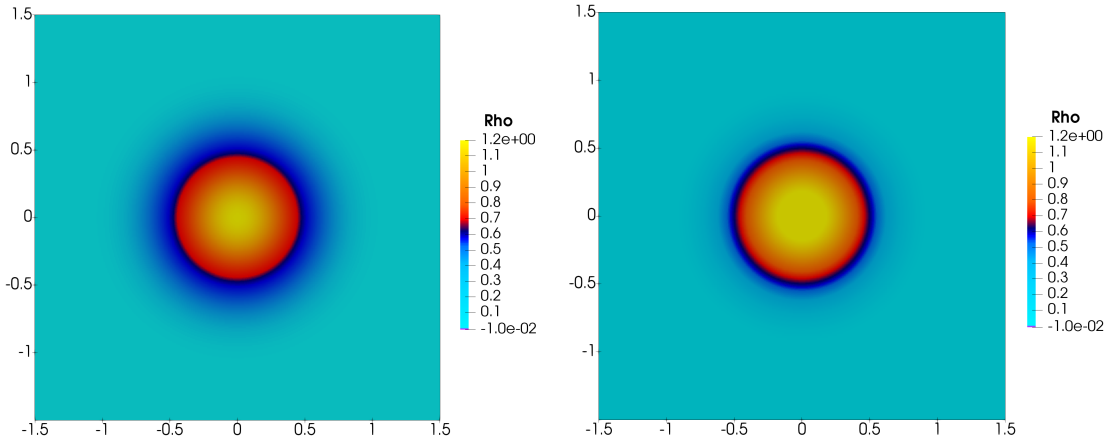

(a) Exact Solution

(b) M1 Closure

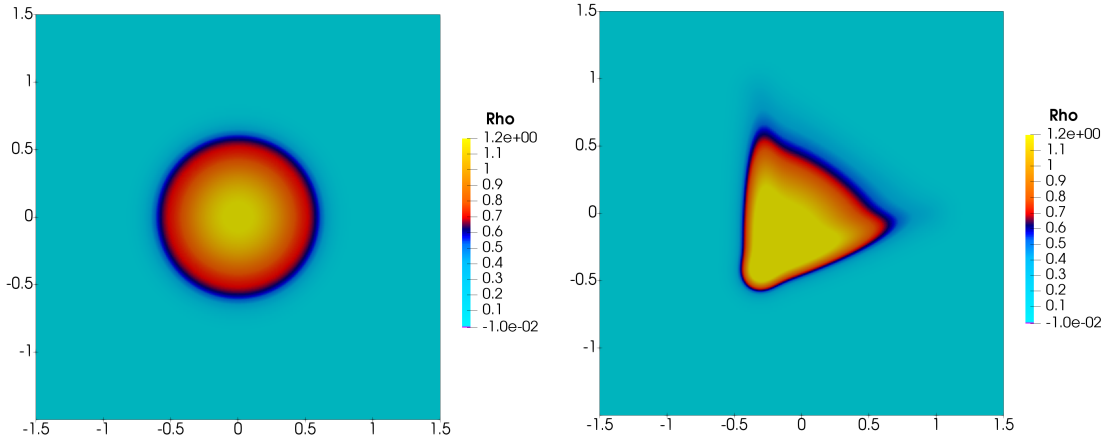

(c) P1 Closure

(d) S1 Closure

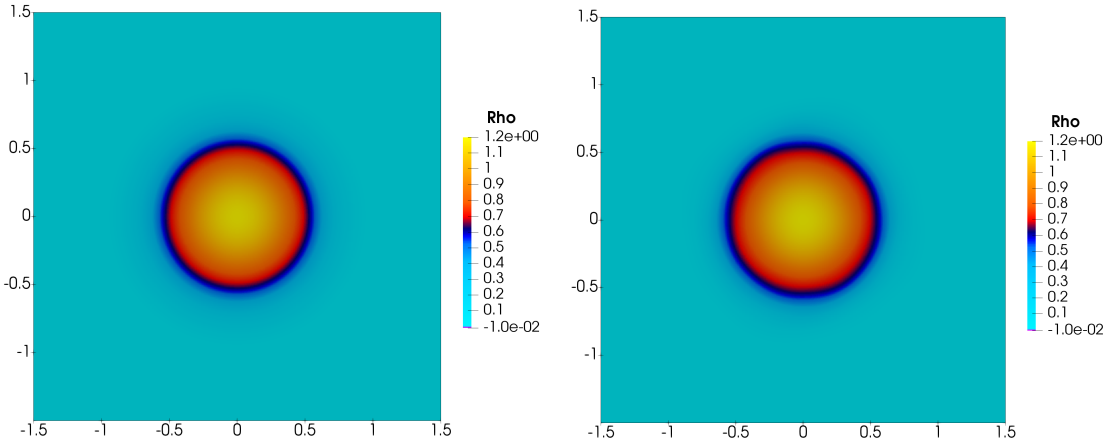

(e) PAQ1 Closure

(f) PAQ1 Closure (Tree)

Figure 4.5: Radiation density, ρ, for the line source benchmark using a scattering constant $\sigma_s = 6.0$ at $t = 1.0$

PAQ_1 model is more expensive to compute then the M_1, P_1 and S_1 closures. As explained in Chapter 3, each time a flux is needed, a positivity check first needs to be done on each of the 1024 quadrature representations before averaging the contribution of all the positive ones. This is obviously computationally expensive. However, the computation time of the PAQ_1 closure using the structured binary tree drastically changes with the background scattering. As the scattering increases, one can observe a reduction in computation time. As explained above, the scattering reduces the maximum value of the bulk velocity by continuously redirecting photons in arbitrary directions. The problem becomes easier to solve numerically, thus the fluxes are calculated higher in the tree data structure using only a few matrix multiplications. However, as discussed above, when the bulk velocity of a given state is too close to the speed of light, the tree data structure produces neither accurate results nor an appreciable gain in efficiency.

4.2 The Hohlraum Problem

The present problem is based on a typical hohlraum found in many nuclear laboratories around the world. In reality, a hohlraum is used to absorb and re-radiate the radiation energy through a process called the indirect drive approach. Typical hohlraum are very small cylindrical objects. Unlike a real hohlraom, the studied problem is described in Cartesian coordinates. This hohlraum problem is a variation of a problem studied previously by Brunner [3].

The problem geometry, shown in Figure 4.6, is 1.3 non-dimensional lengths long by 1.2 wide. There are two openings on either left side of the hohlraum, and a rectangular block of material is placed in the center. The black regions are pure absorbers where $\sigma_a = 100$ and the light blue region is a near perfect vacuum. Since some models can not model a pure void, the initial background radiation density is set to $\rho = 10^{-4}$. All simulations were run using a structured grid of 500

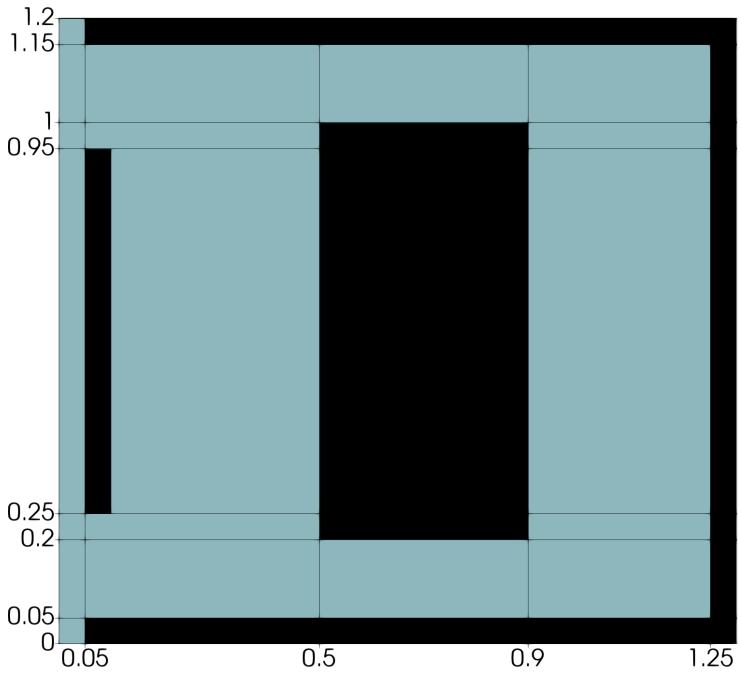

Figure 4.6: Geometry of the hohlraum problem. The black region are pure absorbers regions where $\sigma_a = 100$ and the light blue region is a near perfect vacuum.

by 500 cells. No scattering is used in this problem. In order to model the initial incoming radiation, a fixed boundary condition is applied on the left side of the problem throughout the calculations. The state used for the fixed left boundary condition is,

$$\boldsymbol{U}_{\text{Fixed}} = \begin{bmatrix} \rho \\ \rho u_x \\ \rho u_y \end{bmatrix} = \begin{bmatrix} 1.0 \\ 0.5 \\ 0.0 \end{bmatrix}. \tag{4.10}$$

All other boundary conditions use a zero-gradient condition. This problem was run using the four first-order closures to a final time, $t_{\text{final}} = 2.0$. There is no exact solution for this problem, the goal is simply to study qualitatively the behavior of the different models.

Figure 4.7 shows the solution to the hohlraum problem using all first-order closures. The solutions shown are in steady state. One can see that the P_1 closure, shown in Figure 4.7b, produces a very different solution compared to the other first-

order models and does not agree at all with previous particle calculations [3]. The photon density is much too uniform in front of the block and little or no radiation reaches the right side of the room. It is also important to mentioned that the P_1 closure produces some slightly negative density regions. However, for this case, this behaviour can be attributed to numerical errors. As expected, the S_1 closure, shown in Figure 4.7e, does not produce an accurate solution either. Due to the specific placement of the four quadrature points, the radiation is mostly restricted to move in the x-direction, which is obviously non-physical. As was observed for the line source problem, the M_1 and the PAQ_1 closures produce similar solutions. However, the M_1 closure, Figure 4.7a, is the most accurate model for this problem. The radiation distribution agrees relatively well with previous results obtained using the particle-based model [3]. Due to the difficult initial conditions the bulk velocity of the radiation close to the absorbers is often found to be close to 1.0. In these conditions, the PAQ_1 closure, Figure 4.7c, can only rely on one discrete-ordinates representations to calculate the inter-cell fluxes since the others produces negatives quadrature weights. Under these conditions the radiation distribution is not as uniform and ray effect can be seen. Finally, the PAQ_1 closure using the structures binary tree, Figure 4.7d, produces an asymmetric solution, due to the effect explained in the previous section. However, it still produce better solutions than the S_1 and the P_1 closures using similar computation time. The results obtained can be compared qualitatively by the result computed using an implicit Monte-Carlo method, produced by Brunner [3].

4.3 The Lattice Problem

The lattice problem is based on a rough approximation of a small part of a nuclear reactor core. Radiation is emitted at the center of the geometry and then absorbed by absorbing rods. As seen in Figure 4.8, this problem is a checkerboard of highly scattering and absorbing regions. The blue regions are pure absorbers

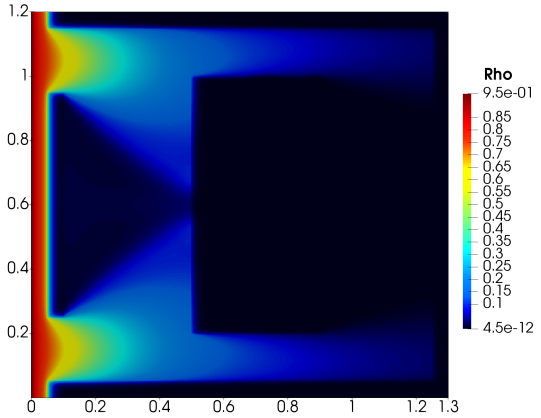

(a) M1 Closure

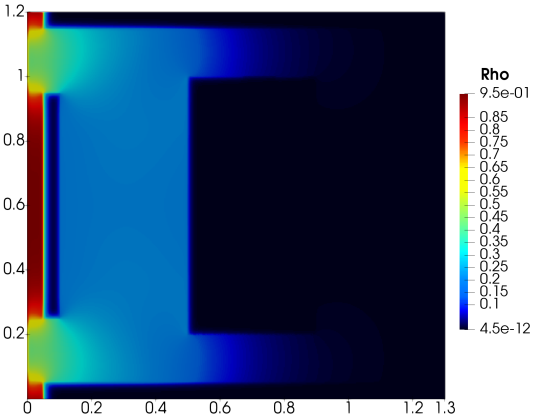

(b) P1 Closure

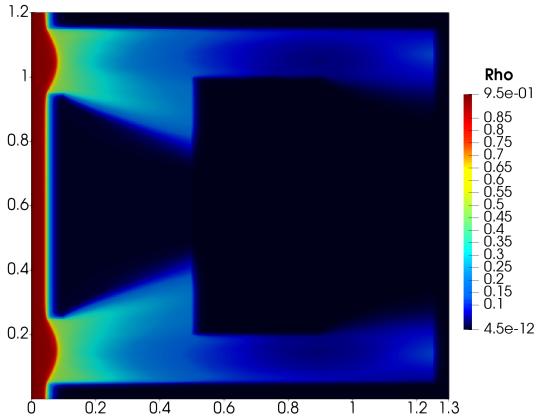

(c) PAQ1 Closure

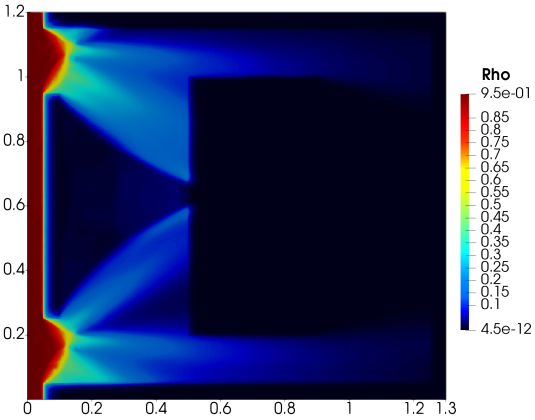

(d) PAQ1 Closure (Tree)

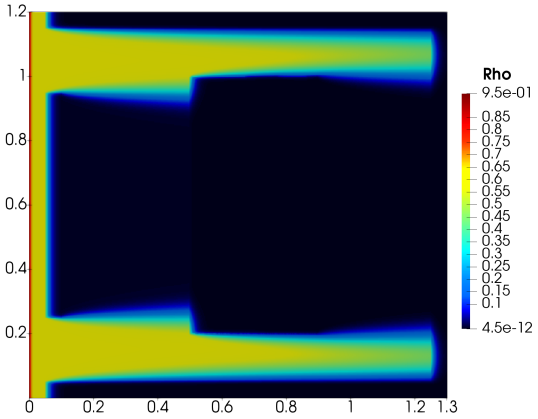

(e) S1 Closure

Figure 4.7: Radiation density, ρ, for the Hohlraum problem

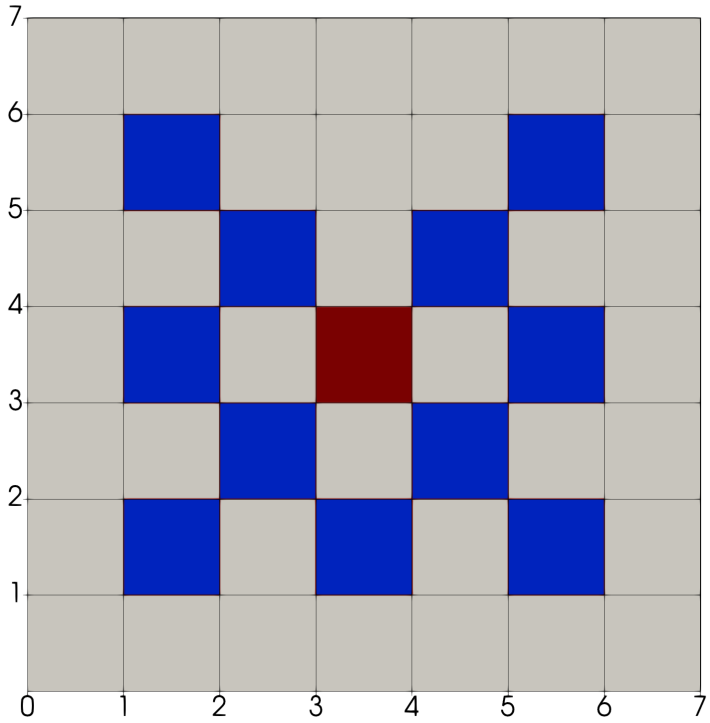

Figure 4.8: Geometry of the Lattice problem. The blue regions are pure absorbers with $\sigma_a = 10$, the red region is a source of radiation where $\sigma_e = 1$ and the white region is a pure scattering region with $\sigma_s = 1$.

with $\sigma_a = 10$, the red region is a source of radiation where the emission is $\sigma_e = 1$ and the white region is a pure scattering region with $\sigma_s = 1$. At time $t = 0.0$ the source is turned on in the center of the system. Again, this problem is studied qualitatively and can be compared on results obtained using an implicit Monte-Carlo method presented in a study conducted by Brunner [3]. As shown in Figure 4.8, the system is 7 units wide in both directions. The absorbers are placed at intervals of 1 non-dimensional length. This problem was run again using the four first-order closures to a final time, $t_{\text{final}} = 1.8$. All simulations were run using a structured grid of 500 by 500 cells.

Figure 4.9 shows the solution using the M_1, P_1, S_1 and PAQ_1 closures. The solution produced using the P_1 model, shown in Figure 4.9b, do not agree with the particle based solution. The radiation does not propagate at the correct speed. One can see an artificial wave front of photons moving at a speed of $v = 1/\sqrt{3}$ which corresponds to the wave speeds calculated in section 3.14. Again both

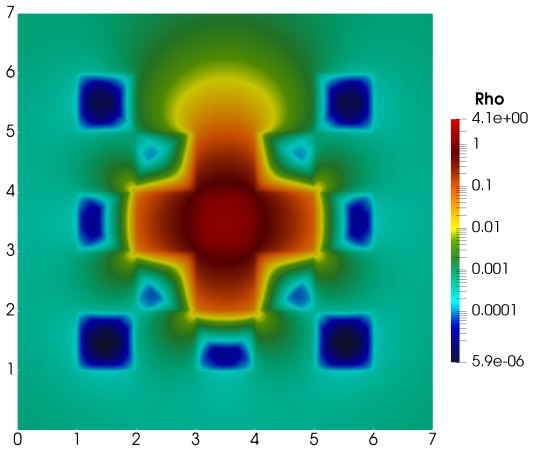

(a) M1 Closure

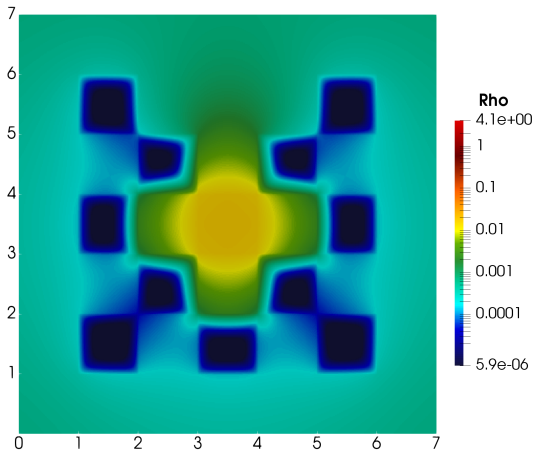

(b) P1 Closure

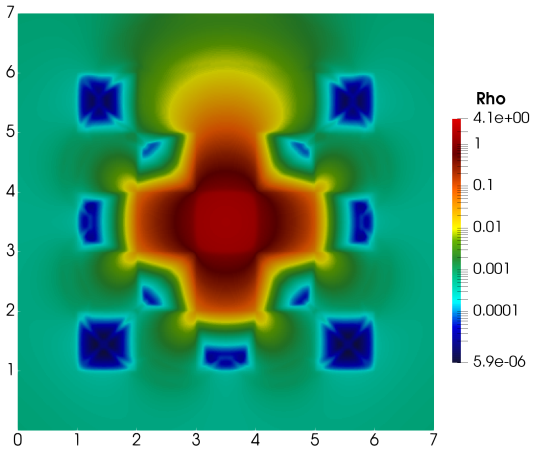

(c) PAQ1 Closure

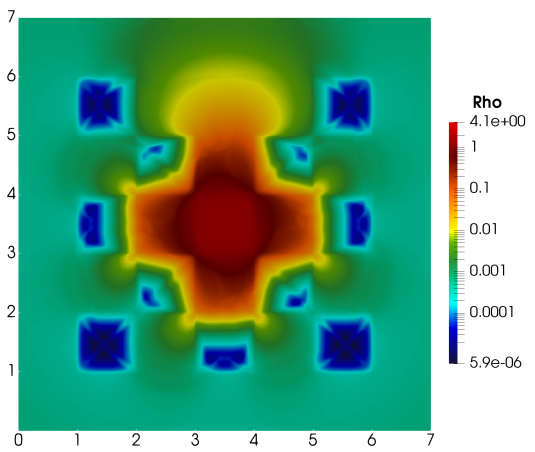

(d) PAQ1 Closure (Tree)

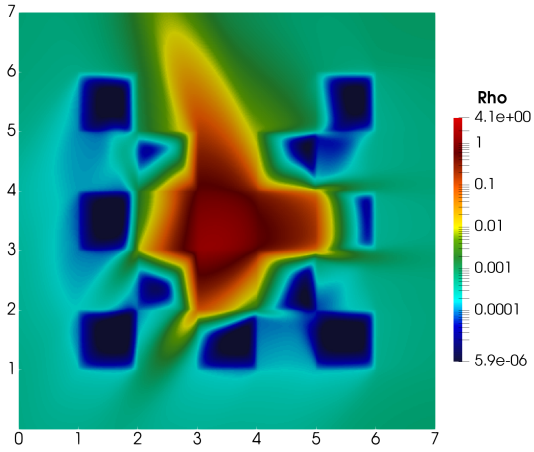

(e) S1 Closure

Figure 4.9: Radiation density, ρ, for the Lattice problem

the M_1 and PAQ_1 closures, shown in Figures 4.9a and 4.9c respectively, produce very similar solutions. These solutions agree relatively well with previous implicit Monte-Carlo solutions [3]. However, one can observe some ray effect on the absorbing rods. The cause of this artifact have been addressed in the hohlraum problem. The solution computed using the PAQ_1 model with the binary tree, Figure 4.9d, shows good agreement with the M_1 and PAQ_1 closures. However the solution is, again, not perfectly symmetric. Finally, as anticipated, the S_1 closure produces an horrible solution. The solution is expected to be perfectly symmetric with respect to the y-axis, which is not recovered by the S_1 closure.

Chapter 5

Second-Order Closure of the Positive-Averaged-Quadratures Hierarchy

The first-order closure of the new Positive-Averaged-Quadratures hierarchy, PAQ_1, is sufficient to conduct a general investigation of the basic behaviours of the proposed modelling hierarchy. However, in order to produce accurate solutions, more information regarding the statistic of the particle velocities will be needed. No model based on only first-order statistics could be expected to yield truly realistic results. Higher-order models are found by going to higher moments. In this chapter, the second-order member of the new Positive-Averaged-Quadratures hierarchy, PAQ_2, is presented. A complete derivation of the moment method is first shown followed by a discussion about the limitations that were discovered when applying this model to the benchmark problems.

5.1 The PAQ_2 closure

As for the first-order closure, this model is based on a low-order discrete-ordinates representation, the S_2 closure. The moments of interest for this second-

order closure are given by,

$$\rho = U_0 = \langle \mathcal{F} \rangle \ , \tag{5.1}$$

$$\rho u_i = U_i = \langle v_i \mathcal{F} \rangle \, , \tag{5.2}$$

$$\rho u_i u_j + P_{ij} = U_{ij} = \langle v_i v_j \mathcal{F} \rangle \ , \tag{5.3}$$

where, P_{ij} is often called the radiative pressure tensor. It basically represents the variance of the particle velocities normalized by the particle density. While the moments U_0 and U_i still represent the particle density and the momentum density respectively. One might expect that the solution vector, $\boldsymbol{U}$, now contains ten entries. The second-order moment is a symmetric second-order tensor producing six distinct moments in addition to the four moments from the first-order system. Closer inspection, however, reveals that the ten moments are not all independent. In fact, the trace of the second-order moment is equal to the zeroth-order moment, as

$$U_{ii} = \langle v_x v_x \mathcal{F} \rangle + \langle v_y v_y \mathcal{F} \rangle + \langle v_z v_z \mathcal{F} \rangle \tag{5.4}$$

$$U_{ii} = \langle v_x v_x \mathcal{F} + v_y v_y \mathcal{F} + v_z v_z \mathcal{F} \rangle \tag{5.5}$$

$$U_{ii} = \left\langle (v_x^2 + v_y^2 + v_z^2) \mathcal{F} \right\rangle \tag{5.6}$$

$$U_{ii} = \left\langle \underbrace{(v_x^2 + v_y^2 + v_z^2)}_{=1} \mathcal{F} \right\rangle \tag{5.7}$$

$$U_{ii} = \langle \mathcal{F} \rangle = \rho \, . \tag{5.8}$$

Therefore, only nine moments are needed to completely defined the system. The solution vector, $\boldsymbol{U}$, and the flux dyad, $\boldsymbol{F}_i$, are as follows,

$$\boldsymbol{U} = \begin{bmatrix} U_x \\ U_y \\ U_z \\ U_{xx} \\ U_{xy} \\ U_{yy} \\ U_{xz} \\ U_{yz} \\ U_{zz} \end{bmatrix}, \qquad \boldsymbol{F}_i = \begin{bmatrix} U_{xi} \\ U_{yi} \\ U_{zi} \\ U_{xxi} \\ U_{xyi} \\ U_{yyi} \\ U_{xzi} \\ U_{yzi} \\ U_{zzi} \end{bmatrix}. \tag{5.9}$$

The discrete-ordinates closure needed to represent this solution now uses nine discrete directions. Since it is not possible to evenly distribute nine points on the surface of a sphere, the discrete directions are configured as three equilateral triangles on parallel planes, as shown in Figure 5.1. This arrangement distributes the points as evenly as possible on the velocity space, thus maximizing the volume covered by the discrete-ordinates representation in moment space.

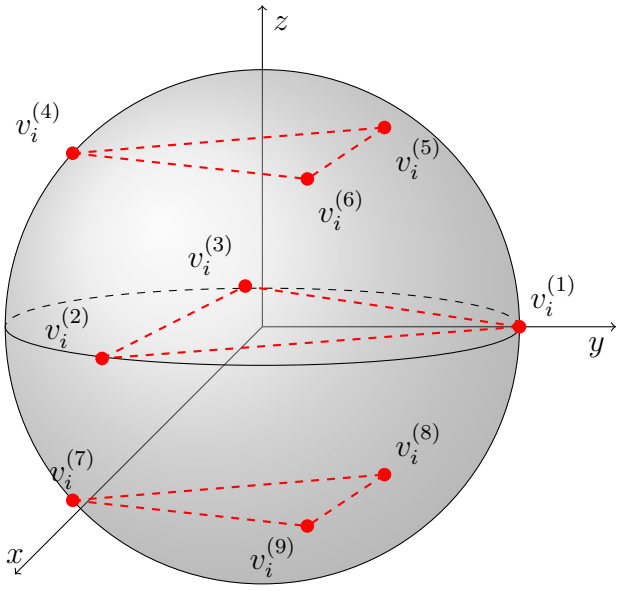

Figure 5.1: S_2 quadrature points in velocity space

The exact coordinates of this arrangement are

$$v_i^{(1)} = \begin{pmatrix} 1 \\ 0 \\ 0 \end{pmatrix}, \quad v_i^{(2)} = \begin{pmatrix} -\frac{1}{2} \\ \frac{\sqrt{3}}{2} \\ 0 \end{pmatrix}, \quad v_i^{(3)} = \begin{pmatrix} -\frac{1}{2} \\ -\frac{\sqrt{3}}{2} \\ 0 \end{pmatrix},$$

$$v_i^{(4)} = \begin{pmatrix} \frac{\cos\pi}{\sqrt{2}} \\ \frac{\sin\pi}{\sqrt{2}} \\ \frac{\sqrt{3}}{2} \end{pmatrix}, \quad v_i^{(5)} = \begin{pmatrix} \frac{\cos 5\pi}{\sqrt{2}} \\ \frac{\sin 5\pi}{\sqrt{2}} \\ \frac{\sqrt{3}}{2} \end{pmatrix}, \quad v_i^{(6)} = \begin{pmatrix} \frac{\cos 7\pi}{\sqrt{2}} \\ \frac{\sin 7\pi}{\sqrt{2}} \\ \frac{\sqrt{3}}{2} \end{pmatrix},$$

$$v_i^{(7)} = \begin{pmatrix} \frac{\cos\pi}{\sqrt{2}} \\ \frac{\sin\pi}{\sqrt{2}} \\ \frac{-\sqrt{3}}{2} \end{pmatrix}, \quad v_i^{(8)} = \begin{pmatrix} \frac{\cos 5\pi}{\sqrt{2}} \\ \frac{\sin 5\pi}{\sqrt{2}} \\ \frac{-\sqrt{3}}{2} \end{pmatrix}, \quad v_i^{(9)} = \begin{pmatrix} \frac{\cos 7\pi}{\sqrt{2}} \\ \frac{\sin 7\pi}{\sqrt{2}} \\ \frac{-\sqrt{3}}{2} \end{pmatrix}.$$

Using a similar method as presented in Chapter 2 for the S_1 closure, the moments of interest are related to the weight of each delta function through the relation

$$\boldsymbol{Q}\,\boldsymbol{W} = \boldsymbol{U}\,, \tag{5.10}$$

where, $\boldsymbol{Q}$ is now defined as,

$$\begin{bmatrix} v_x^{(1)} & v_x^{(2)} & & v_x^{(9)} \\ v_y^{(1)} & v_y^{(2)} & & v_y^{(9)} \\ v_z^{(1)} & v_z^{(2)} & & v_z^{(9)} \\ v_x^{(1)}v_x^{(1)} & v_x^{(2)}v_x^{(2)} & & v_x^{(9)}v_x^{(9)} \\ v_x^{(1)}v_y^{(1)} & v_x^{(2)}v_y^{(2)} & \cdots & v_x^{(9)}v_y^{(9)} \\ v_y^{(1)}v_y^{(1)} & v_y^{(2)}v_y^{(2)} & & v_y^{(9)}v_y^{(9)} \\ v_x^{(1)}v_z^{(1)} & v_x^{(2)}v_z^{(2)} & & v_x^{(9)}v_z^{(9)} \\ v_y^{(1)}v_z^{(1)} & v_y^{(2)}v_z^{(2)} & & v_y^{(9)}v_z^{(9)} \\ v_z^{(1)}v_z^{(1)} & v_z^{(2)}v_z^{(2)} & & v_z^{(9)}v_z^{(9)} \end{bmatrix},$$

and $\boldsymbol{W}$, is the vector of quadrature weights, $w^{(l)}$. If one knows the values of the moments in $\boldsymbol{U}$, the distribution function weights, $w^{(l)}$, are found as,

$$\boldsymbol{W} = \boldsymbol{Q}^{-1}\boldsymbol{U}\,. \tag{5.11}$$

The flux dyad for this system, $\boldsymbol{F}_i$ can be expressed in vector form as,

$$\boldsymbol{F}_i = \boldsymbol{Z}_i\,\boldsymbol{W}\,, \tag{5.12}$$

with $\boldsymbol{Z}$ given by,

$$\begin{bmatrix}
v_x^{(1)}v_i^{(1)} & v_x^{(2)}v_i^{(2)} & & v_x^{(9)}v_i^{(9)} \\
v_y^{(1)}v_i^{(1)} & v_y^{(2)}v_i^{(2)} & & v_y^{(9)}v_i^{(9)} \\
v_z^{(1)}v_i^{(1)} & v_z^{(2)}v_i^{(2)} & & v_z^{(9)}v_i^{(9)} \\
v_x^{(1)}v_x^{(1)}v_i^{(1)} & v_x^{(2)}v_x^{(2)}v_i^{(2)} & & v_x^{(9)}v_x^{(9)}v_i^{(9)} \\
v_x^{(1)}v_y^{(1)}v_i^{(1)} & v_x^{(2)}v_y^{(2)}v_i^{(2)} & \cdots & v_x^{(9)}v_y^{(9)}v_i^{(9)} \\
v_y^{(1)}v_y^{(1)}v_i^{(1)} & v_y^{(2)}v_y^{(2)}v_i^{(2)} & & v_y^{(9)}v_y^{(9)}v_i^{(9)} \\
v_x^{(1)}v_z^{(1)}v_i^{(1)} & v_x^{(2)}v_z^{(2)}v_i^{(2)} & & v_x^{(9)}v_z^{(9)}v_i^{(9)} \\
v_y^{(1)}v_z^{(1)}v_i^{(1)} & v_y^{(2)}v_z^{(2)}v_i^{(2)} & & v_y^{(9)}v_z^{(9)}v_i^{(9)} \\
v_z^{(1)}v_z^{(1)}v_i^{(1)} & v_z^{(2)}v_z^{(2)}v_i^{(2)} & & v_z^{(9)}v_z^{(9)}v_i^{(9)}
\end{bmatrix}\,.$$

Finally, as shown for the first-order closure, it is possible to write the fluxes produced by one second-order discrete-ordinates representation as linear functions of the known moments, $\boldsymbol{U}$,

$$\boldsymbol{F}_i = \boldsymbol{Z}_i\,\boldsymbol{Q}^{-1}\boldsymbol{U}\,. \tag{5.13}$$

The family of discrete-ordinates representations used for a flux calculation is, as for the PAQ_1 closure, constructed by rotating this "initial quadrature" representation around the z-axis. This process is depicted in Figure 5.2. Once the family of discrete-ordinates is built, the PAQ_2 closure uses Algorithm 1, presented in chapter 3, to calculate the flux. All the quadratures are first tested for positivity

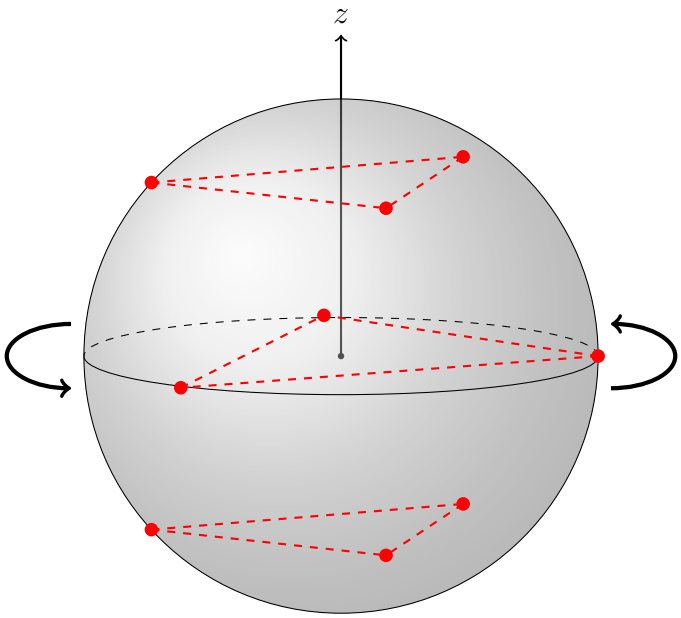

Figure 5.2: PAQ_2, Collection of quadrature points on the velocity space

of the weights before their specific contributions are added to the net flux. One can see that the general method is identical to the one used for the PAQ_1 closure. Unfortunately, when implemented and tested on every problems studied in Chapter 4, this method failed to produce a solution in every case. Every time, the calculation was terminated because this method predicts a state, $\boldsymbol{U}$, that cannot be represented by any of the discrete-ordinates representations with positive weights. After extensive investigation, it was found that this problem is caused by the non-convexity of the moment space covered by this model.

5.2 The Realizability Domain of the Second-Order Moments

The realizability domain of moments is defined as the collection of states, $\boldsymbol{U}$, that can be represented by at least one non-negative distribution function. In other words, it is the collection of all the moment states, $\boldsymbol{U}$, that are physically realizable. For a fixes density, U_0, the realizability domain of the first-order moments is simply described as a sphere, where any state with an average velocity below the speed

of light is possible. However, the realizable domain of the second-order moments is much more complex. This domain exists in nine dimensions, which is difficult to imagine or even understand. The realizability limits of second-order closure are known and can be written using the known moments, U_0, U_i and U_{ij} as,

$$\begin{aligned} \mathrm{tr}(U_{ij}) = U_0 > 0\,, \\ \text{and} \qquad U_0 U_{ij} - U_i U_j \quad \text{is simmetric positive definite} \end{aligned} \tag{5.14}$$

The complete proof of this result is demonstrated by Kershaw [12]. One can see that the first condition has already been applied in the previous section in order to reduce the the state vector, $\boldsymbol{U}$, to nine entries. The second condition can be expressed in vector form using two tensors denoted $\boldsymbol{\mathcal{A}}$ and $\boldsymbol{\mathcal{B}}$. First the tensor, $\boldsymbol{\mathcal{A}} = U_0 U_{ij}$, can be expressed as,

$$\boldsymbol{\mathcal{A}} = \begin{bmatrix} U_0 U_{xx} & U_0 U_{xy} & U_0 U_{xz} \\ U_0 U_{yx} & U_0 U_{yy} & U_0 U_{yz} \\ U_0 U_{zx} & U_0 U_{zy} & U_0 U_{zz} \end{bmatrix}, \tag{5.15}$$

and the tensor, $\boldsymbol{\mathcal{B}} = U_i U_j$, as

$$\boldsymbol{\mathcal{B}} = \begin{bmatrix} U_x U_x & U_x U_y & U_x U_z \\ U_y U_x & U_y U_y & U_y U_z \\ U_y U_x & U_x U_y & U_Z U_z \end{bmatrix}. \tag{5.16}$$

The condition is such that the tensor formed by $\boldsymbol{\mathcal{A}} - \boldsymbol{\mathcal{B}}$,

$$\boldsymbol{\mathcal{A}} - \boldsymbol{\mathcal{B}} = \begin{bmatrix} U_0 U_{xx} - U_x U_x & U_0 U_{xy} - U_x U_y & U_0 U_{xz} - U_x U_z \\ U_0 U_{yx} - U_y U_x & U_0 U_{yy} - U_y U_y & U_0 U_{yz} - U_y U_z \\ U_0 U_{zx} - U_y U_x & U_0 U_{zy} - U_x U_y & U_0 U_{zz} - U_Z U_z \end{bmatrix}, \tag{5.17}$$

is symmetric positive definite. For simplicity and since all the studied problems are two-dimensional, the analysis is done in 2D for the rest of the chapter. Hence,

in order to study this realizable space, moments of odd order in v_z (that are U_z, U_{xz}, U_{yz}), are taken to be zero. This leads to,

$$\boldsymbol{\mathcal{A}} - \boldsymbol{\mathcal{B}} = \begin{bmatrix} U_0 U_{xx} - U_x U_x & U_0 U_{xy} - U_x U_y & 0 \\ U_0 U_{yx} - U_y U_x & U_0 U_{yy} - U_y U_y & 0 \\ 0 & 0 & U_0 - U_{xx} - U_{yy} \end{bmatrix}, \tag{5.18}$$

Using the leading principle minors, one can find the relations describing the limits of the two-dimensional realizable space as follows,

$$U_{xx} - U_x U_x \geq 0 \tag{5.19}$$

$$(U_{xx} - U_x U_x)(U_{yy} - U_y U_y) - (U_{xy} - U_x U_y)^2 \geq 0 \tag{5.20}$$

$$(1 - U_{xx} - U_{yy}) \left[(U_{xx} - U_x U_x)(U_{yy} - U_y U_y) - (U_{xy} - U_x U_y)^2 \right] \geq 0 \tag{5.21}$$

It is important to note that using this 2D simplification the realizability domain in moment space is now restricted to five dimensions. The first condition, forces the radiative pressure to be greater or equal to zero, while the second condition describes the realizability domain as a parabolic space in U_x, U_y, U_{xx}, U_{xy} and U_{yy} moment space. Finally the third condition restricts the value of U_{zz} to be non-negative.

5.3 The Moment Space Covered by the PAQ_2 Closure

The first-order model of the new hierarchy, the PAQ_1 closure, produces a convex realizable moment space. By rotating enough discrete-ordinates representations, the general first-order realizability domain can be almost entirely covered. This means that every state, $\boldsymbol{U}$, predicted by this first-order closure, lands within the reach of at least one discrete-ordinates representations. In order to study the moment space covered by the PAQ_2 closure, a single discrete-ordinates represen-

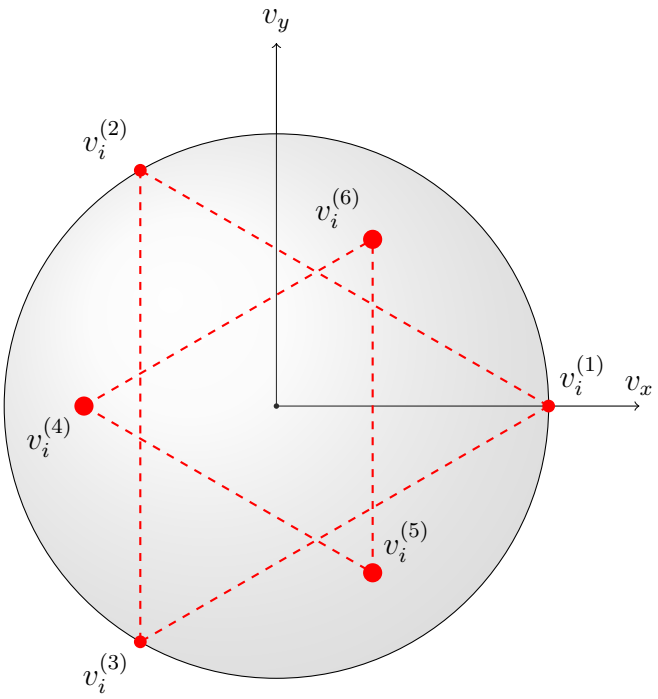

Figure 5.3: Projection of the "initial" discrete-ordinates representations, S_2, on a 2D velocity space

tation is first considered. Under the restriction that $U_0 = 1$, the moment space covered by this discrete-ordinates representation forms a simplex in moment space. Every possible state possible, $\boldsymbol{U}$, that can be represented by this quadrature rule is a convex combination of at least two nodes forming the simplex. Each of the node is found using the moment equation, Eq. (5.10), with the constraint that all particles are only moving along each corresponding specific direction. By using the 2D description presented in the previous section, one can redefine the matrix, $\boldsymbol{Q}$, to be based on the arrangement shown in Figure 5.3. In this figure, the original three-dimensional discrete-ordinates representation is projected on the 2D velocity space. Using this 2D discrete-ordinates representation, the matrix $\boldsymbol{Q}$ can be

written as,

$$\boldsymbol{Q} = \begin{bmatrix} 1 & 1 & 1 & 2 & 2 & 2 \\ v_x^{(1)} & v_x^{(2)} & v_x^{(3)} & 2v_x^{(4)} & 2v_x^{(5)} & 2v_x^{(6)} \\ v_y^{(1)} & v_y^{(2)} & v_y^{(3)} & 2v_y^{(4)} & 2v_y^{(5)} & 2v_y^{(6)} \\ v_x^{(1)}v_x^{(1)} & v_x^{(2)}v_x^{(2)} & v_x^{(3)}v_x^{(3)} & 2v_x^{(4)}v_x^{(4)} & 2v_x^{(5)}v_x^{(5)} & 2v_x^{(6)}v_x^{(6)} \\ v_x^{(1)}v_y^{(1)} & v_x^{(2)}v_y^{(2)} & v_x^{(3)}v_y^{(3)} & 2v_x^{(4)}v_y^{(4)} & 2v_x^{(5)}v_y^{(5)} & 2v_x^{(6)}v_y^{(6)} \\ v_y^{(1)}v_y^{(1)} & v_y^{(2)}v_y^{(2)} & v_y^{(3)}v_y^{(3)} & 2v_y^{(4)}v_y^{(4)} & 2v_y^{(5)}v_y^{(5)} & 2v_y^{(6)}v_y^{(6)} \end{bmatrix}.$$

One can see that the contribution of the forth, fifth and sixth discrete directions ($v_i^{(4)}$, $v_i^{(5)}$, $v_i^{(6)}$), have been multiplied by a factor of two. This is necessary since each of these directions now correspond to two superposed quadrature points. The limits of the moment space covered by one quadrature representation is described as a simplex in this five-dimensional moment space. Again, each of the six nodes forming this five-dimensional simplex is found by calculating the moments, $\boldsymbol{U}$, such that all the particles are moving along only one specific discrete direction at the time. Mathematically, the nodes of the simplex, $\boldsymbol{\mathcal{N}}^{(l)}$, are found by solving the following moment equation,

$$\boldsymbol{\mathcal{N}}^{(l)} = \boldsymbol{Q}\boldsymbol{W}^{(l)}, \tag{5.22}$$

where the weight vectors, $\boldsymbol{W}^{(l)}$, are defined as,

$$\boldsymbol{W}^{(1)} = \begin{bmatrix} 1 \\ 0 \\ 0 \\ 0 \\ 0 \\ 0 \end{bmatrix}, \boldsymbol{W}^{(2)} = \begin{bmatrix} 0 \\ 1 \\ 0 \\ 0 \\ 0 \\ 0 \end{bmatrix}, \boldsymbol{W}^{(3)} = \begin{bmatrix} 0 \\ 0 \\ 1 \\ 0 \\ 0 \\ 0 \end{bmatrix}, \boldsymbol{W}^{(4)} = \begin{bmatrix} 0 \\ 0 \\ 0 \\ 1 \\ 0 \\ 0 \end{bmatrix}, \boldsymbol{W}^{(5)} = \begin{bmatrix} 0 \\ 0 \\ 0 \\ 0 \\ 1 \\ 0 \end{bmatrix}, \boldsymbol{W}^{(6)} = \begin{bmatrix} 0 \\ 0 \\ 0 \\ 0 \\ 0 \\ 1 \end{bmatrix}.$$

Since the transformation between the space of positive weights and the moment space is linear, the edges of the simplex of realizable states are four-dimensional hyperplanes.

5.3.1 Visualization of the PAQ_2 Moment Space

In order to study the moment space covered by the PAQ_2 closure and compare it to the general realizable space described previously, a slice of this five-dimensional space is considered. Since it is impossible to visualize the total five-dimensional space, this three-dimensional plane is used in order to acquire a basic understanding of the behaviour of the closure. The plane of interest is chosen in U_x, U_{xx} and U_{yy} space. This choice is completely arbitrary and the technique illustrated bellow works for any plane in moment space. In order to find the area that the five dimensional simplex covers on the chosen plane, one must find the points given by the intersection of each edge of the simplex and the plane of interest. For the following investigation, the plane is chosen such that is satisfies the following condition,

$$U_{xx} + U_{yy} + U_{zz} = 1\,, \tag{5.23}$$

with the restriction that $U_{zz} = U_{yy}$. This leads to,

$$U_{xx} + 2\,U_{yy} = 1\,. \tag{5.24}$$

This equation can be used to describe a plane in U_x, U_{xx} and U_{yy} space. The plane is represented in Figure 5.4. It is useful to rewrite the plane equation in its so called parametric form using two noncollinear vectors $\vec{u}$ and $\vec{v}$ and an arbitrary point $\vec{P_0}$ defined on the plane,

$$\vec{r}(a,b) = a\ \vec{u} + b\ \vec{v} + \vec{P_0}\,. \tag{5.25}$$

As explained is the previous section, the nodes, $\boldsymbol{\mathcal{N}}^{(l)}$, forming the simplex are found using Eq. (5.22). Using this relation, it is possible to write a second parametric equation, $\vec{r}_s(\alpha)$, representing every possible state contained in the simplex

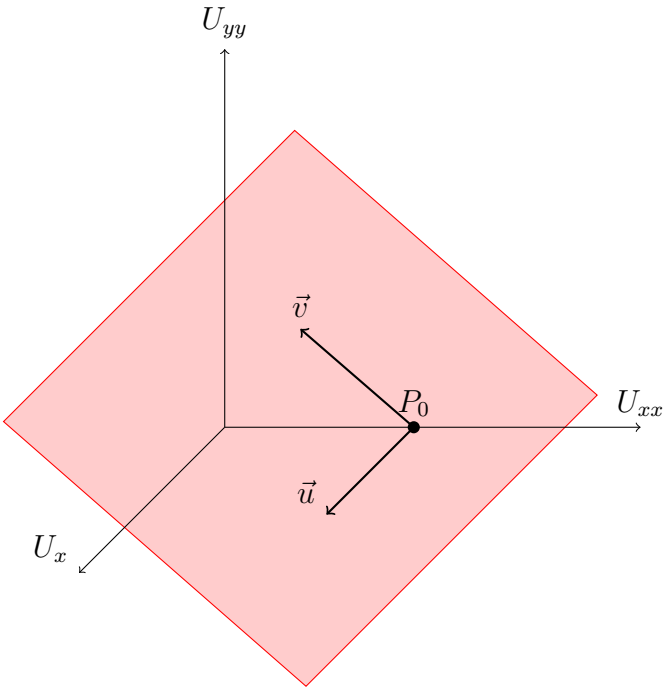

Figure 5.4: Representation of the plane of interest in U_x, U_{xx} and U_{yy} space.

as a linear-combination of the nodes. This parametric equation is written as,

$$\vec{r}_s(\alpha) = \alpha_1 \, \boldsymbol{\mathcal{N}}^1 + \alpha_2 \, \boldsymbol{\mathcal{N}}^2 + \alpha_3 \, \boldsymbol{\mathcal{N}}^3 + \alpha_4 \, \boldsymbol{\mathcal{N}}^4 + \alpha_5 \, \boldsymbol{\mathcal{N}}^5 + \alpha_6 \, \boldsymbol{\mathcal{N}}^6 \, . \tag{5.26}$$

Intersection between one edge of the five dimensional simplex and the plane of interest occurs when at least two of the parameters, α, are zero. Thus the intersection points forming the limits of moment space covered on the chosen plane are simply found by solving the following linear system for every possible combination of the four remaining nodes (α_i, α_j, α_k and α_l),

$$a \, \vec{u} + b \, \vec{v} + \vec{P_0} = \alpha_i \, \boldsymbol{\mathcal{N}}^i + \alpha_j \, \boldsymbol{\mathcal{N}}^j + \alpha_k \, \boldsymbol{\mathcal{N}}^k + \alpha_l \, \boldsymbol{\mathcal{N}}^l \, . \tag{5.27}$$

Finally, the point, $\vec{r}_s(\alpha_i, \alpha_j, \alpha_k, \alpha_l)$, is an intersection if and only if the parameters a and b exist and the sum of the α is one. Once all intersections are found, it is possible to plot the area that the simplex covers on the plane of interest and compare it with the global realizability limits of second-order moment space. Figure 5.5 shows the space covered by one discrete-ordinates representation on the

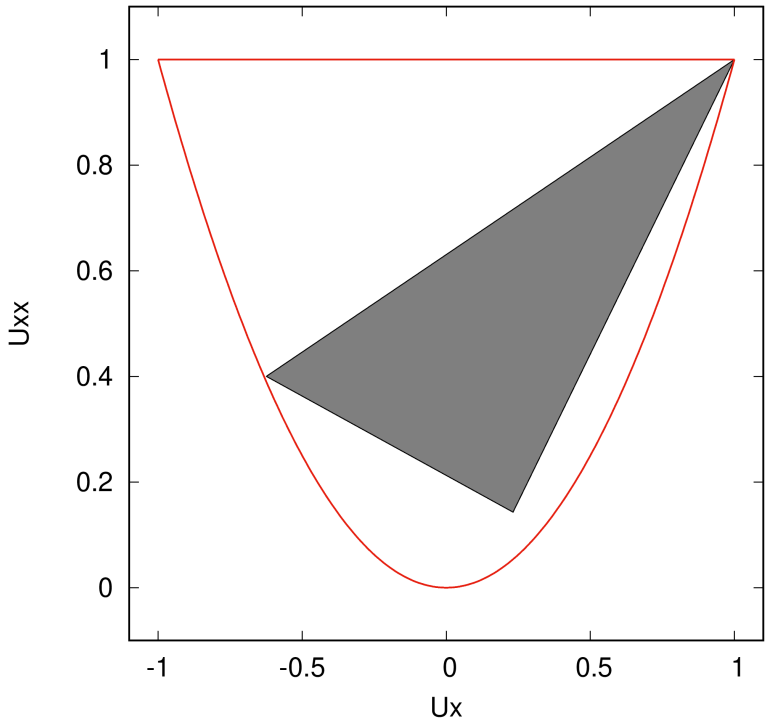

Figure 5.5: Moment space covered by one discrete-ordinates representation on the U_x and U_{xx} plane

chosen slice of moment space. The red lines correspond to the global realizability limits of second-order moment space on the U_x and U_{xx} plane. The limits are calculated using Eq. (5.19). One can see that the discrete-ordinates quadrature does not cover a big portion the realizability domain. It is hoped that by adding more quadrature representation, the moment space covered by the PAQ_2 closure will approach the global realizability limits, as was the case for the PAQ_1 closure.

The convexity of the moment space covered by each model is also important. If two radiating states $\boldsymbol{U_1}$ and $\boldsymbol{U_2}$ interacts, one can imagine that the two states move towards a weighted average state. As pictured in Figure 5.6, if the moment space covered by the model is convex, the average between any two realizable states, denoted $\boldsymbol{U_1}$ and $\boldsymbol{U_2}$, is also realizable. However, if the realizable space for a particular model is not convex, the weighted average between the two states can leave realizable space. Since the moment space covered by one discrete-ordinates representation is convex, all the initial states $\boldsymbol{U}$ that can be represented by this

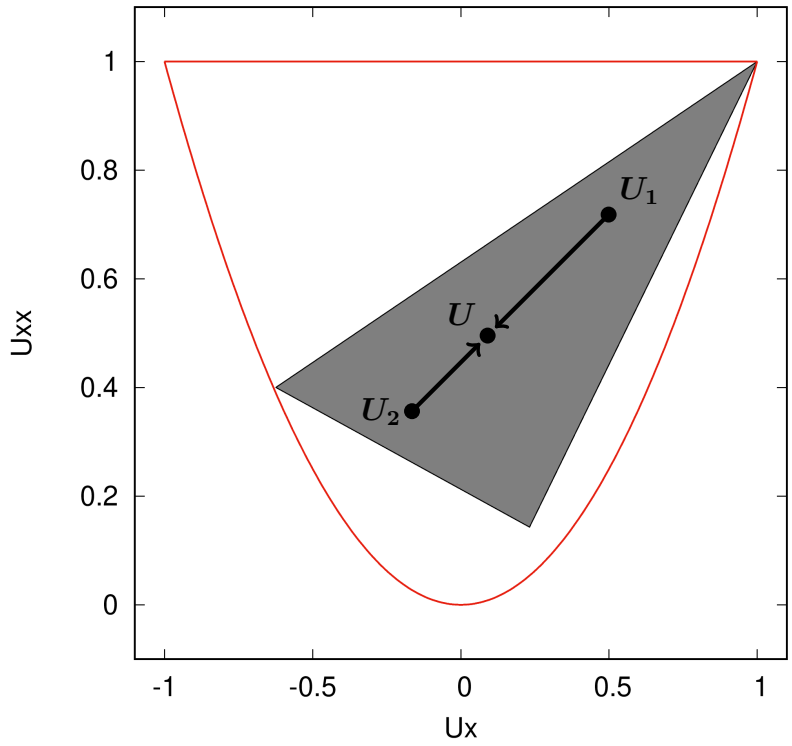

Figure 5.6: Average state $\boldsymbol{U}$, on the moment space covered by one discrete-ordinates representation on the U_x and U_{xx} plane

simple quadrature are guaranteed to stay within the realizability domain of the model.

By applying this technique to the collection of discrete-ordinates representations forming the PAQ_2 model, the moment space covered using this closure can be plotted. Figure 5.7, shows the moment space covered by the PAQ_2 closure on the same U_x and U_{xx} plane using increasing number of discrete-ordinates representations. First, one can see that increasing the number of discrete-ordinates barely covers more moment space. Furthermore, the moment space produced by the new closure is not convex. Often times during a calculations the model predicts an average state that is outside of the space that can be represented by the closure, therefore the solution becomes impossible to compute. This situation is pictured in Figure 5.8. The problem is mainly due to the fact that the rotations applied to the "initial quadrature" do not cover the space evenly in all directions. Even when using different rotation orientations, the moment space covered using

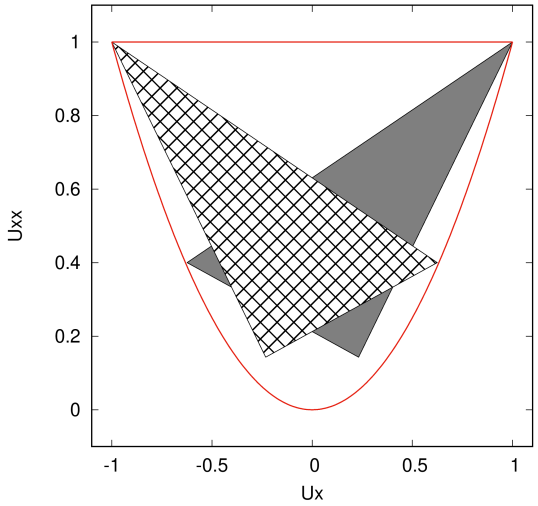

(a) 2 discrete-ordinates representations

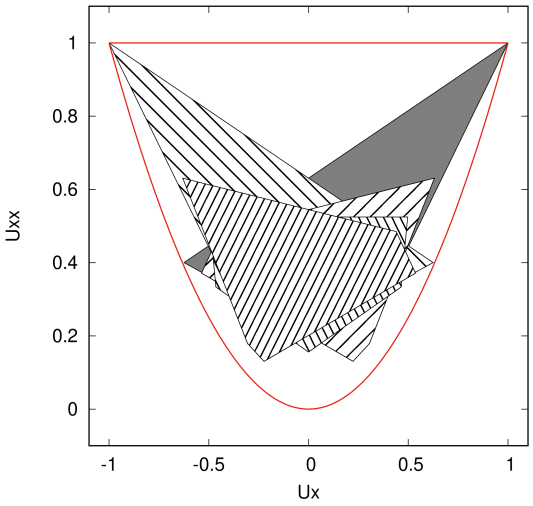

(b) 8 discrete-ordinates representations

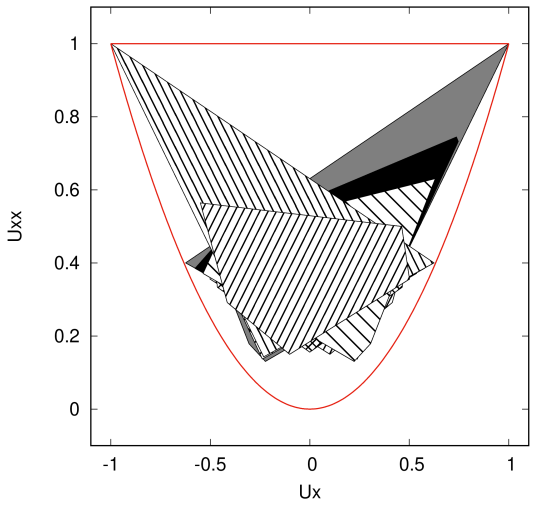

(c) 32 discrete-ordinates representations

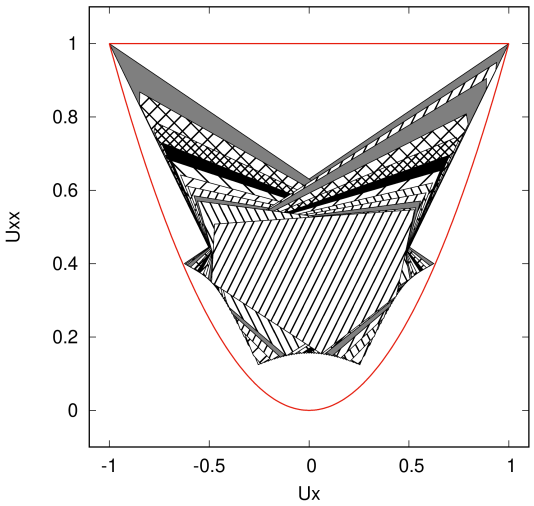

(d) 128 discrete-ordinates representations

Figure 5.7: Moment space covered by the PAQ_2 closure on the U_x and U_{xx} plane for increasing number of discrete-ordinates representations

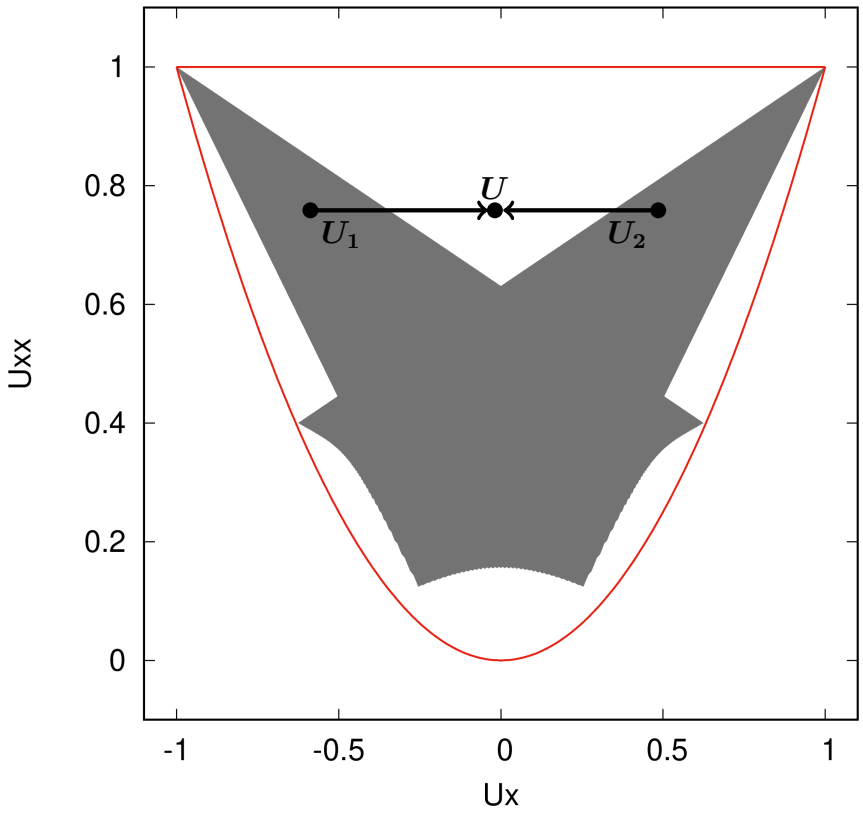

Figure 5.8: Average state $\boldsymbol{U}$, on the moment space covered by the PAQ_2 closure on the U_x and U_{xx} plane

this technique always seems to be non-convex. This difficulty greatly limits the construction of the PAQ hierarchy.

Chapter 6

Conclusion

Radiation plays an important role in many engineering systems. The traditional methods used for the numerical simulation of radiative transport suffer from serious modelling artifacts [14]. The spherical-harmonics models produce rotationally invariant solutions and are relatively inexpensive to compute, but often predict a negative particle density in some regions. The discrete-ordinates models, on the other hand, preserve positivity, but do not generate symmetric solutions. In order for the discrete-ordinates to be accurate, a huge number of prescribed directions must be chosen, thus making the model very computationally expensive. Finally maximum-entropy models produce positive and rotationally invariant solutions. However, all but the first-order closure cannot be written in closed form. In other words, for higher than the first-order closure, whenever a flux is needed, an expensive and ill-conditioned entropy-maximization problem must be solved numerically. This entropy-maximization requires many integrals that must be accurately evaluated using quadratures, leading to large computational expense.

The goal of this research project was to design a new hierarchy of radiative transport models that produces rotationally invariant solutions while preserving positivity of the particles's density field. It has been demonstrated that the first-order closure of the proposed model hierarchy, due to its special flux averaging

procedure, maintains positivity and produces a solution with almost perfect symmetry. However, the proposed method can be relatively expensive to compute compared to other first-order closures. When this first-order closure was combined with the binary-tree data structure, the computational cost decreased drastically. However, the model then no longer produces rotationally invariant solutions. By applying the first-order closure to the line-source problem, it was possible to show that the simulations maintain relatively good agreement with the exact solutions compared to the other studied first-order models. Again, when applied to both the hohlraum problem and the lattice problem, the new first-order model shows promising behaviours that lead to the investigation of the second-order closure of the new hierarchy. Unfortunately, it was found that, when the new technique was applied to the second-order closure, the model could not produce solutions to any of the benchmarks. The calculations was always terminated because the model predicts a state that cannot be represented by any of the quadrature rules forming the model. By studying the moment space covered by this second-order closure, it was shown that the proposed technique will always lead to space of realizable moments that is non-convex. It, unfortunately, seams unlikely that the technique in its current form cant easily be used to produce higher-order, more accurate closures.

Bibliography

[1] C. Berthon, P. Charrier, and B. Dubroca. An HLLC scheme to solve the M1 model of radiative transfer in two space dimensions. *SIAM, Journal on Scientific Computing*, 31:347–389, 2017.

[2] T. A. Brunner. Riemann solvers for time-dependent transport based on the maximum entropy and spherical harmonics closures. *Ph.D. Thesis, University of Michigan*, 2000.

[3] T. A. Brunner. Form of approximate radiation transport. Technicel Report 2002–1778, Sandia National Laboratories, July 2002.

[4] T. A. Brunner and J. P. Holloway. One-dimensional riemann solvers and the maximum entropy closure. *Journal of Quantitative Spectroscopy and Radiative Transfer*, 69:543–566, 2001.

[5] T. A. Brunner, J. P. Holloway, and K. G. Powell. Using an approximate riemann solver with the maximum entropy closure. *Transactions of the American Nuclear Society*, 79:128–129, 1998.

[6] T. Christen and F. Kassubek. Minimum entropy production closure of the photo hydrodynamic equations for radiative heat transfer. *Journal of Quantitative Spectroscopy and Radiative Transfer*, 110:452–463, 2009.

[7] D. Fan. *Evaluation of Maximum Entropy Moment Closure for Solution To Radiative Heat Transfer Equation.* Master's Thesis, University of Toronto, 2012.

[8] M. Frank, C. D. Hauck, and E. Olbrant. Perturbed, entropy-based closure for radiative transfer. *Kinetic and Related Models*, 6:557–587, 2013.

[9] C. D. Ganapol. Homogeneous infinite media time dependent analytic benchmarks for x-tm transport methods development. Technical report, Los Alamos National Laboratory, 1999.

[10] C. K. Garrett and C. D. Hauck. A comparison of moment closures for linear kinetic transport equations: The line source benchmark. *Transport Theory and Statistical Physics*, 42:203–235, 2013.

[11] J. Jung, H. Chijiwa, K. Kobayashi, and H. Nishihara. Discrete ordinate neutron transport equation equivalent to PL approximation. *Nuclear Science and Engineering*, 49:1–9, 1972.

[12] D. S. Kershaw. A new method for numerical solution of the transprot equation. Technicel Report 1976–94550, Lawrence Livermore Laboratory, July 1996.

[13] G. M. Kremer. *An Introduction to the Boltzmann Equation and Transport Processes in Gases*. Springer-Verlag Berlin Heidelberg, 2010.

[14] C. Kuehn. *Moment Closure - A Brief Review*. Springer, New York, 2015.

[15] C. D. Levemore. Moment closure hierarchies for kinetic theories. *Journal of Statistical Physics*, 83:1021–1065, 1996.

[16] E. E. Lewis and W. F. Miller. *Computational Methods of Neutron Transport*. American Nuclear Society, New York, 1993.

[17] T. Linde. A practical, general-purpose, two-state HLL Riemann solver for hyperbolic conservation laws. *Astronomy and Astrophysic, ASCI Flash Center, University of Chicago*, 2002.

[18] J. G. McDonald. *Extended Fluid-Dynamic Modelling for Numerical Solution of Macro-Scale Flows*. Ph.D. Thesis, Graduate Department of Aerospace Engineering, University of Toronto, 2011.

[19] J. G. Mcdonald and C. P. T. Groth. Numerical modeling of micron-scale flows using the gaussian moment closure. Paper 2005–5035, AIAA, June 2005.

[20] M. P. Menguc and R. Viskanta. Radiative transfer in three-dimensional rectangular enclosures containing inhomogeneous anisotropically scattering media. *Journal of Quantitative Spectroscopy and Radiative Transfer*, 33:533–549, 1985.

[21] W. F. Miller and W. H. Reed. Ray-effect mitigation methods for twodimensional neutron transport theory. *Nuclear Science and Engineering*, 62:391–411, 1997.

[22] I. Müller and T. Ruggeri. *Extended Thermodynamics*. Springer-Verlag, New York, 1993.

[23] G. C. Pomeraning. *The Equations of Radiation Hydrodynamics*. Dover books on physic, 1973.

[24] T. Prichard and G. W. Alldredge. An approximation of the M2 closure: application to radiotherapy dose simulation. *Journal of Computational and Theoretical Transport*, 45:174–183, 2017.

[25] W. H. Reed. Spherical harmonic solutions of the neutron transport equation from discrete ordinate codes. *Nuclear Science and Engineering*, 49:10–19, 1972.

[26] R. W. Schefer, D. M. Wicksall, and A. K. Agrawal. Combustion of hydrogen-enriched methane in a lean premixed swirl-stabilized burner. *Proceedings of the Combustion Institute*, 29:843–851, 2000.

[27] P. L. Tallec and J. P. Perlat. Numerical analysis of Levermore's moment system. Technicel Report 3124, INRIA Rocquencourt, 1997.

[28] R. Viskanta and M. P. Menguc. Radiation heat transfer in combustion systems. *Progress in Energy and Combustion Science*, 13:97–160, 1987.